Subhajit Konar

2K20PHDME508_Thesis_Subhajit Konar.pdf

Delhi Technological University

Document Details

Submission ID
trn:oid:::27535:125278334

Submission Date
Dec 28, 2025, 10:00 PM GMT+5:30

Download Date
Dec 29, 2025, 10:41 AM GMT+5:30

File Name
2K20PHDME508_Thesis_Subhajit Konar_2.pdf

File Size
5.6 MB

196 Pages

41,202 Words

227,076 Characters

10% Overall Similarity

The combined total of all matches, including overlapping sources, for each database.

Filtered from the Report

- Bibliography
- Quoted Text
- Cited Text
- Small Matches (less than 14 words)

Exclusions

- 9 Excluded Sources
- 2 Excluded Matches

Match Groups

123 Not Cited or Quoted 10%
Matches with neither in-text citation nor quotation marks

0 Missing Quotations 0%
Matches that are still very similar to source material

0 Missing Citation 0%
Matches that have quotation marks, but no in-text citation

0 Cited and Quoted 0%
Matches with in-text citation present, but no quotation marks

Top Sources

2% Internet sources
7% Publications
3% Submitted works (Student Papers)

Integrity Flags

1 Integrity Flag for Review

Replaced Characters
75 suspect characters on 18 pages
Letters are swapped with similar characters from another alphabet.

Our system's algorithms look deeply at a document for any inconsistencies that would set it apart from a normal submission. If we notice something strange, we flag it for you to review.

A Flag is not necessarily an indicator of a problem. However, we'd recommend you focus your attention there for further review.

Match Groups

- **123** Not Cited or Quoted 10%
  Matches with neither in-text citation nor quotation marks
- **0** Missing Quotations 0%
  Matches that are still very similar to source material
- **0** Missing Citation 0%
  Matches that have quotation marks, but no in-text citation
- **0** Cited and Quoted 0%
  Matches with in-text citation present, but no quotation marks

Top Sources

2% Internet sources
7% Publications
3% Submitted works (Student Papers)

Top Sources

The sources with the highest number of matches within the submission. Overlapping sources will not be displayed.

1	Submitted works	University of the Aegean on 2019-02-05 <1%
2	Internet	www.researchgate.net <1%
3	Internet	worldwidescience.org <1%
4	Publication	Atul S. Takalkar, Lenin Babu Mailan Chinnapandi. "Deep drawing process at the el... <1%
5	Publication	Rahul Datta, Marrapu Bhargava. "Investigation of microstructure and microtextu... <1%
6	Publication	A. Steuwer, M.J. Peel, P.J. Withers. "Dissimilar friction stir welds in AA5083–AA608... <1%
7	Publication	Mishra, R.S.. "Friction stir welding and processing", Materials Science & Engineeri... <1%
8	Publication	Subhajit Konar, Vijay Gautam. "Investigations on Formability Enhancement of Fri... <1%
9	Publication	Bijendra Prasad, Vijay Gautam. "Experimental and Numerical Investigations of Fo... <1%
10	Publication	Reddy, Randall Dwain. "Effect of Tool Geometries on Butt Dissimilar Friction Stir ... <1%

11 Publication
Rakesh Kumar, Vijay Gautam. "Influence of Magnesium Content on Tensile Prope... <1%

12 Publication
Kamble, Liladhar Vitthal. "Study of Effect of Design and Process Parameters on Al... <1%

13 Submitted works
IIT Delhi on 2024-07-15 <1%

14 Publication
Vijay Gautam, D Ravi Kumar. "Experimental and numerical investigations on spri... <1%

15 Submitted works
Pandit Deendayal Petroleum University on 2022-06-11 <1%

16 Publication
"Revolutionizing Aircraft Materials and Processes", Springer Science and Business... <1%

17 Publication
A. Maciolek, A. Jöckel, S. Völkers, M. Hatzky et al. "Influence of Short-Time Post-W... <1%

18 Publication
Praveen Kumar, Satpal Sharma. "Effect of high tool rotational speed and pin diam... <1%

19 Submitted works
North Eastern Regional Institute of Science and Technology on 2025-10-30 <1%

20 Publication
Bijendra Prasad, Vijay Gautam. "Investigations on Formability of a SS/AA Clad She... <1%

21 Publication
Adetunla, Adedotun Olanrewaju. "Friction Stir Processing: Simulation and Experi... <1%

22 Submitted works
Uttar Pradesh Technical University on 2022-01-01 <1%

23 Internet
idr.nitk.ac.in <1%

24 Submitted works
Anna University on 2025-07-16 <1%

25 Publication
Muhamad Zulkhairi Rizlan, Ahmad Baharuddin Abdullah, Zuhailawati Hussain. "T... <1%

26 Publication
Bijendra Prasad, Vijay Gautam. "Investigations on Formability of a SS/AA Clad She... <1%

27 Internet
gyan.iitg.ernet.in <1%

28 Publication
"Flexible Automation and Intelligent Manufacturing: The Human-Data-Technolog... <1%

29 Submitted works
National Institute of Technology, MIZORAM on 2022-09-01 <1%

30 Publication
Xiaolong Liu, Pu Xie, Robert Wimpory, Wenya Li, Ruilin Lai, Meijuan Li, Dongfeng ... <1%

31 Submitted works
NIT Imphal on 2019-01-29 <1%

32 Internet
theses.hal.science <1%

33 Publication
"Light Metals 2018", Springer Nature, 2018 <1%

34 Publication
Azeez, Sarafadeen Tunde. "Weld Reliability Characterisation of Dissimilar Friction ... <1%

35 Publication
Najm, Sherwan Mohammed. "Parametric Effects of Single Point Incremental Shee... <1%

36 Publication
Plessinger, Ryan. "Characterization of Galvanized/Galvannealed Sheet Steel Defec... <1%

37 Submitted works
Charotar University of Science And Technology on 2017-10-10 <1%

38 Publication
Sreevivasan, Narasimhan. "Effects of laser welding on formability aspects of adva... <1%

39 Publication

Yarrapareddy, Eswar. "Development of slurry erosion resistant materials by laser... <1%

40 Publication

"Recent Advances in Manufacturing Processes and Systems", Springer Science an... <1%

41 Publication

Aiman H. Al-Allaq, Manish Ojha, Yousuf S. Mohammed, Srinivasa N. Bhukya, Zhen... <1%

42 Submitted works

Anna University on 2025-01-28 <1%

43 Publication

Georgios Patsalias, Konstantinos Sofias, Achilles Vairis. "Solid-State Welding of Th... <1%

44 Submitted works

Universiti Sains Malaysia on 2022-09-29 <1%

45 Publication

Aldoğan, Enver Burak. "Grain Refinement of Al-Si-Mg Cast Alloys with Niobium – B... <1%

46 Submitted works

Anna University on 2025-09-09 <1%

47 Publication

Changshu He, Hanwen Zhou, Hao Zhang, Jingxun Wei, Xiaodan Li, Gaowu Qin. "Fo... <1%

48 Publication

Gang Song, Zejie Wang, Xiaoyu Fan, Liming Liu. "Research Progress of Aluminum ... <1%

49 Internet

www.preprints.org <1%

Experimental and Numerical Investigations on Formability of Tailor Welded Blanks Prepared by Friction Stir Welding Process

Thesis Submitted
in Partial Fulfillment of the
Requirements for the Degree of

DOCTOR OF PHILOSOPHY

by

Subhajit Konar

(Roll No.: 2K20/PHDME/508)

Under the supervision of

Prof. Vijay Gautam

Department of Mechanical Engineering

DELHI TECHNOLOGICAL UNIVERSITY

(Formerly Delhi College of Engineering)

Shahbad Daulatpur, Main Bawana Road, Delhi-110042, India

December, 2025

DELHI TECHNOLOGICAL UNIVERSITY

(Formerly Delhi College of Engineering)
Shahbad Daulatpur, Main Bawana Road, Delhi-42

CANDIDATE'S DECLARATION

I, **SUBHAJIT KONAR**, hereby certify that the work which is being presented in the thesis entitled "**Experimental and Numerical Investigations on Formability of Tailor Welded Blanks Prepared by Friction Stir Welding Process**" in partial fulfillment of the requirements for the award of the Degree of Doctor of Philosophy, submitted in the Department of Mechanical Engineering, Delhi Technological University is an authentic record of my own work carried out during the period from January, 2021 to August 2025 under the supervision of Prof Vijay Gautam, Department of Mechanical Engineering, DTU, Delhi. The matter presented in the thesis has not been submitted by me for the award of any other degree of this or any other Institute.

Subhajit Konar

(Roll No.- 2K17/PHDME/508)

DELHI TECHNOLOGICAL UNIVERSITY

(Formerly Delhi College of Engineering)
Shahbad Daulatpur, Main Bawana Road, Delhi-42

CERTIFICATE

Certified that SUBHAJIT KONAR (2K20/PHDME/508) has carried out their search work presented in this thesis entitled "**Experimental and Numerical Investigations on Formability of Tailor Welded Blanks Prepared by Friction Stir Welding Process**" for the award of **Doctor of Philosophy** from Department of Mechanical Engineering, Delhi Technological University, Delhi, under my supervision. The thesis embodies results of original work, and studies are carried out by the student himself and the contents of the thesis do not form the basis for the award of any other degree to the candidate or to anybody else from this or any other University/Institution.

Prof. VIJAY GAUTAM
Professor
Department of Mechanical Engineering
Delhi Technological University

Date:

ACKNOWLEDGEMENTS

42

I would like to convey my deep sense of gratitude and sincere thanks to my supervisor Professor Vijay Gautam, Department of Mechanical Engineering, Delhi Technological University, for giving me an opportunity to pursue this research work under his guidance. He has been a tremendous mentor for me. Perseverance, exuberance, positive approaches are just some of the traits they have imprinted on my personality.

He steered me through this journey with his invaluable advice, positive criticism, stimulating discussions and consistent encouragement. If I will stand proud of my achievements, then undeniably he is the main creditor. It is my privilege to be under his guidance. His advice on both research as well as on my career have been priceless. Words are short to suffice his favour and cooperation. I am grateful to him in all respects.

I would like to express my gratitude to Prof. Prateek Sharma, Vice chancellor, Delhi Technological University, Delhi for providing this opportunity to carry out this work in this prestigious institute.

I would like to thank Prof. B.B. Arora, Head of the Department of Mechanical Engineering, and Prof. Atul Kumar Agrawal, DRC Chairman, for their esteemed support in finishing this work.

I wish to record my thanks and gratitude to my Internal SRC expert, Prof. Atul Kumar Agrawal, Department of Mechanical Engineering (Delhi Technological University); and External SRC expert Prof. Anil Kumar, Department of Chemistry (Delhi Technological University), for their valuable guidance, critical and constructive discussion during this work.

I would like to thank my senior fellow research scholars Dr. Pankaj Kumar Sharma, Mr Rakesh Kumar, Dr. Bijendra Prasad and Dr. Ravi Datt Yadav, Mr Praveen Kumar Singh, Mr Gaurav Ranjan and, for steering me in my challenges during Ph.D. work. Their valuable experience was very needful in improving my quality of research work. Without their support and motivation, pursuit of this Ph.D. work would have never been possible.

I would like to thank lab assistant/ Senior Technician Mr. Ignatius Francis, Mr. Om Prakash and Mr. Tek Chand for their help and support during the experimental work in the Metal Forming Laboratory.

I sincerely thank the anonymous reviewers whose insightful and constructive comments and suggested revisions improved the organization and clarity of the research.

I am greatly indebted to my brothers Dhrubajeet and Sabyasachi for their continuous love throughout the journey. With immense pleasure and delight, I would like to thank my wife ***Mrs. Raima*** for giving me mental and moral support in my highs and lows of this Ph.D. journey. I am greatly indebted to my parents Mr. Jagannath Konar and Mrs. Sandhya Konar for their love and blessings to see me scaling greater heights of life. With immense pleasure and delight.

Finally, I would like to express my gratitude to the supreme personality, Radha Rani & Lord Krishna, for giving me the patience and strength to overcome all types of hindrances.

Subhajit Konar

(Roll No.- 2K17/PHDME/508)

ABSTRACT

With the advent in technology, the automotive parts makers are particularly interested in the utilization of new manufacturing concepts and modern materials. The phrase "tailor welded blank (TWB)" refers to a blank in which two or more sheets of material are welded together to form a single blank before the forming process. TWBs have considerable benefits in terms of lowering manufacturing costs, reducing vehicle weight, and enhancing part performance.

Experimental and numerical investigations on the formability of longitudinally butt-welded tailor welded blank of the same thickness prepared by friction stir welding is presented in the thesis. The friction stir welding technique involves a solid-state stirring mechanism to butt weld the two blanks of aluminium alloy AA5083 and AA6082 both in annealed state. This study employs a Taguchi approach to systematically explore and optimize critical FSW parameters such as tool rotational speed and traverse speed, while keeping axial force as constant. The influence of each parameter on weld quality metrics, such as tensile properties (strength and ductility), hardness distribution, and defect formation, is assessed using an appropriate orthogonal array (L9) and signal-to-noise (S/N) ratio analysis. The Taguchi approach identifies the most significant parameters and their optimal levels with fewer experimental trials, boosting joint efficiency, increasing material flow in the stir zone, and ensuring a defect-free weld. This optimization framework offers a reliable and cost-effective way for creating different FSW joints between AA5083 and AA6082 alloys. In order to study the effect of welded region on formability, experiments are performed on tailor welded blanks with and without the annealing operation. The tensile properties of the parent sheets, welded blanks and welded region are determined by performing standard uniaxial tension tests. The formability of tailor-welded blanks was investigated by performing limiting dome height (LDH) tests

and measuring major and minor strains along and across the weld line in deformed samples. The elastic properties, true stress-true strain and anisotropic data sets are used in the material model for the prediction of failure strains to develop forming limit plots. The predicted results from finite element analysis are validated with the experimental results obtained from limiting dome height test and are found to correlate well with experimental data. The annealing is observed to enhance the formability of the FSTWB by almost 13% in plane strain and equibiaxial stretch conditions.

Keywords: Friction Stir Welding, Tailor Welded Blank, Formability, Stretch Forming, Limiting Dome Height, Strain Distribution, Finite Element Analysis.

TABLE OF CONTENTS

LIST OF FIGURES

LIST OF TABLES

LIST OF ABBREVIATIONS

ASTM	American Society for Testing and Materials
AA	Aluminium alloy
BHF	Blank holding force
CAE	Computer Aided Engineering
FLD	Forming limit diagram
TRS	Tool Rotational Speed
TTS	Tool Travel Speed
FEA	Finite Element Analysis
HV	Hardness on Vickers scale
LDH	Limiting Dome height
UTS	Ultimate Tensile Strength
UTM	Universal testing machine
XRD	X-ray diffraction
YS	Yield strength
EDX	Energy-Dispersive X-ray
SS	Stainless Steel

NOMENCLATURE

R	Plastic strain ratio
$\bar{r}$	Normal anisotropy
Δr	Planar anisotropy
σ	True stress
ε	True strain
$\dot{\varepsilon}$	Strain rate
N	Strain hardening exponent
M	Strain rate sensitivity
K	Strength coefficient
μ	Friction coefficient

CHAPTER 1

INTRODUCTION

Automakers are continuously searching for new and innovative ways to reduce vehicle weight and manufacturing costs in order to meet increasingly stringent fuel economy criteria while remaining economically competitive. The usage of tailor welded blanks (TWBs) offers a potential option to address these seemingly contradicting needs. Tailor welded blanks are made by welding numerous sheets of material together before shaping. In a conventional sheet-metal forming techniques, the blank is normally constructed of a single piece with a constant thickness and is cut from a big sheet. However, the new trend of using TWBs involves the use of numerous pieces of sheet metal of varying forms and thicknesses or of different materials [1].

The joining of sheets in TWBs is a critical manufacturing step that enables the integration of sheets with different thicknesses, grades, or material properties into a single blank prior to forming. This method allows designers to accurately arrange material strength and thickness, which improves structural performance, reduces weight, and optimizes material utilization. Welding techniques such as friction stir welding, laser beam welding, and resistance welding are often used for TWB fabrication because they create small weld zones with little distortion and mechanical integrity [2]. The weld's quality defined by its strength, ductility, microstructural homogeneity, and defect-free nature has a major impact on the overall formability and performance of the custom welded blank during subsequent forming operations. A well-executed joint enables consistent strain distribution across the weld and base materials, whereas poor joining can cause strain localization and premature failure.

The weld region in a friction stir tailor welded blank (FSTWB) prepared by joining of two or more sheets with same or different thickness of same or different materials in a single plane prior to forming is the main reason for reduction in its formability. However, due to numerous benefits, it is important to enhance the formability of TWBs used in sheet metal components for automotive and aerospace industries. Also, It has become an essential mass production technology which reduces the weight of the finished products by eliminating number of reinforcements and stiffeners [1]. Mass optimization for lighter components is achieved by the use of a low density ultra-high strength aluminium alloy, which offers good formability and crashworthiness [2]. Based on classification, fusion welding and solid-state welding are the two techniques commonly employed to prepare a TWB. Although, the fusion welding technique is a high speed process providing good joint strength and efficiency in the steel components, it is not preferred in welding aluminium alloys due to the formation of an oxide layer and other solidification defects [3]. Friction stir welding (FSW) technique is a solid state welding process which is a good alternative to the fusion welding in addressing the problems encountered in welding aluminium alloys. It incorporates the use of friction heat caused due to severe plastic deformation using a non-consumable rotating tool moving along the weld line during joining of the two different sheets by a mechanical inter-locking mechanism [4]. Apart from low power consumption, FSW technique offers good weld strength and integrity with a negligible distortion [5]. In the last decades, owing to academic and industrial applications, many researchers have studied the deformation behaviour and formability of TWBs prepared by FSW technique [6-8]. Silva et al., 2009 [9] carried out experimental studies on the forming behaviour of a TWB of aluminium alloy using a single point incremental forming

technique and confirmed that FSW produced TWB can be successfully used in the manufacturing of components requiring deep depths. Experimental and numerical methods were used by Kim et al., 2010 [10] to study the formability of FSTWBs made of four different sheets with varying thicknesses, such as 6111-T4, 5083-H18, 5083-O, and DP590. Yld2000-2d, a non-quadratic orthogonal anisotropic yield function, was used without considering anisotropy. It was concluded that accurate numerical prediction of forming limit is dependent on the properties of the welded region. Nguyen et al., 2015 [11] studied the springback behavior of tailor welded blanks (TWBs) made from twinning-induced plasticity (TWIP) and mild steels, noting significant differences on either side due to the large disparity in material strength. To mitigate springback defects during the U-draw bending process of such TWBs, the researchers applied varying blank holding force (BHF) profiles on both sides of the blank. They proposed a systematic method to determine optimal BHF-stroke profiles that reduced the springback. Hariharan et al., 2014 [12] studied the formability of tailor welded blanks with a very high strength ratio, created by joining TWIP and low carbon steels, through numerical analysis using a limiting dome height test. They modified the drawbead geometry on the weaker side to enhance the dome height. The drawbead design was optimized by treating it as a multi-objective problem, with the goals of maximizing dome height and minimizing weld line movement. Hovanski et al., 2015 [13] carried out experimental and numerical characterization of aluminium alloy TWBs prepared by high speed FSW technique for mass production. Simulations were performed on TWBs and machined dissimilar blanks for different thickness ratios and it was concluded that predicted results are in good agreement with the experimental data. Kesharwani et al., 2015 [4] experimentally and numerically characterized the

formability of tailor friction stir welded blanks of AA5754-H22/AA5052-H32 on the basis of limiting draw ratio and also, optimized the welding parameters to achieve optimum weld strength and ductility using Taguchi Orthogonal array approach. Perente et al., 2016 [14] investigated the formability of TWB consisting of AA5182/AA6061 prepared by FSW and compared the results with the formability of parent sheets. Khan et al., 2017[15] studied the mechanical behaviour of a friction stir welded blanks and reported an acceptable joint efficiency although with a higher hardness due to grain refinement in the stirring zone. Bhukya et al., 2022 [16] experimentally investigated the effects of heat treatment on the microstructure and mechanical properties of a copper aided friction welding of AA6061 aluminium alloy. Copper assisted FSW of the alloy joint was prepared at a constant tool rotational speed of 1400 rpm and welding speed at 1 mm/s. FSW specimens were subjected to solid solution heat treatment at 540 °C for 1 hour followed by quenching in water at ambient temperature and then ageing artificially at 180 °C for 6 hours and 24 hours followed by air cooling. It was concluded that a softening effect brought on by the breakdown of hardening precipitates is indicated by Vickers micro hardness. The consistent distribution of fine hardening precipitates at all aging time levels is most likely responsible for hardness recovery. Feyissa et al., 2018 [17] conducted experimental studies on the characterization of microstructure, mechanical properties and formability of cryorolled and annealed AA5083 alloy sheets and compared the properties with cold rolled sheets. The influence of annealing time and temperature on hardness was studied, and it was observed that annealing at 275 °C for 15 min after cryorolling yielded a good combination of strength and ductility.

On the basis of the literatures, it is concluded that an excessive plastic deformation during FSW produces equiaxed recrystallized grains which are responsible for higher strength and lower ductility in the welded region resulting in reduced formability. Therefore, in order to enhance the formability of a TWB produced by FSW technique, it is imperative to improve the ductility of the welded region by reducing the dislocation density and resultant residual stresses through heat treatment route.

In the present study, experimental and numerical investigations are carried out to analyse the effect of annealing operation on formability of TWBs. To prepare a good butt weld, FSW parameters are optimised using design of experiments and analysis of variance (ANOVA). The tensile properties of the parent sheets, welded blanks and welded region are determined by standard uniaxial tension tests. In order to predict the failure strains, forming limit curves are drawn using limiting dome height tests and simulations. A series of experiments are conducted to decide an optimum annealing temperature for TWBs thereby reducing the strength, residual stress and hardness in strain free grains in the welded region. The forming limit curves obtained from experiments show that the formability of friction stir welded blank is significantly enhanced after the annealing process.

TWB enables design engineers to integrate and position the optimal qualities of materials within the component where they are required. This provides the ideal attributes by integrating the necessary features of the blanks, allowing for precise engineering of the design. It has evolved into a crucial mass manufacturing technology that diminishes the weight of completed items by reducing the quantity of reinforcements and stiffeners. The Corporate Average Fuel Economy 2025 (CAFE) regulations [18], established by the U.S. Congress in 1975 following the Arab Oil

Embargo, aim to enhance the average fuel efficiency of cars and light trucks sold in the United States. Mass optimization of components and subsystems can be accomplished through the utilization of low-density, ultra-high strength alloys, such as aluminum alloys, which offer excellent formability and crashworthiness. The most significant qualities are low density, high specific energy absorption performance, and outstanding specific strength. Aluminum exhibits corrosion resistance and may be recycled to its original purity. Welding aluminum blanks using traditional procedures to prepare a TWB [19] is rather difficult. Friction stir welding (FSW) emerged as a technique for combining aluminum alloys through a solid-state joining process [20]. Noor Zaman Khan et al. [21] (2017) examined the mechanical and microstructural properties of friction stir welded comparable and dissimilar aluminum alloy blanks, demonstrating increased hardness attributed to grain refinement in the stirring zone, along with a durable joint efficiency. The FSW process utilizes material locking [22] for joining, attributed to its stirring mechanism. FSW, as a solid-state joining technique, circumvents numerous flaws associated with porosity, blowholes, and inadequate solidification. The pronounced plastic deformation at extreme temperatures during Friction Stir Welding results in equiaxed recrystallized grains, which contribute to the increased strength and diminished formability of the weld zone [23]. Warm forming is a superior method to improve the formability of Tailor Welded Blanks.

1.1 Sheet metal forming

Sheet metal forming is crucial in the production of intricate components for the automobile industry, domestic appliances, and aircraft parts, as it minimizes material waste and energy consumption while allowing designers to leverage the material's

inherent qualities. The process entails transforming flat sheet metal blanks into components of specified forms, either in a single stage or via numerous stages, by applying external forces that induce significant plastic deformation in the material. Plastic deformation occurs due to the application of tensile or compressive loads, or a combination of both. Common sheet metal forming operations include stretch forming, deep drawing, and bending, as shown in Figure 1.1. During a stretch forming operation, the peripheries of a sheet metal blank are secured by exerting a substantial blank holding force, while a stiff tool or punch is employed to deform the material to get the intended shape. During the stretch forming process, the material experiences pure tensile pressures. This method offers superior form control and surface quality compared to rolled or drawn components [24]. This technology is mostly utilized in the aerospace sector for the fabrication of aircraft skin panels. Deep drawing is a significant sheet metal forming technique in which material is shaped into a die of appropriate geometry. In this procedure, as opposed to stretching, the material is extracted from the outer flange region into the die to achieve the intended form. This procedure is mostly employed to manufacture components of significant depth through single or several processes. The deep drawing technique entails a mix of tensile and compressive stresses. The flange region experiences compressive hoop stress and radial tensile stress; elevated compressive hoop stress can lead to wrinkling. This can be mitigated by exerting adequate blank holding force. In the cup wall region, the material experiences plane strain stretching, resulting in considerable thinning. The metal at the center of the blank experiences biaxial tensile stress as a result of contact with the bottom punch [25].

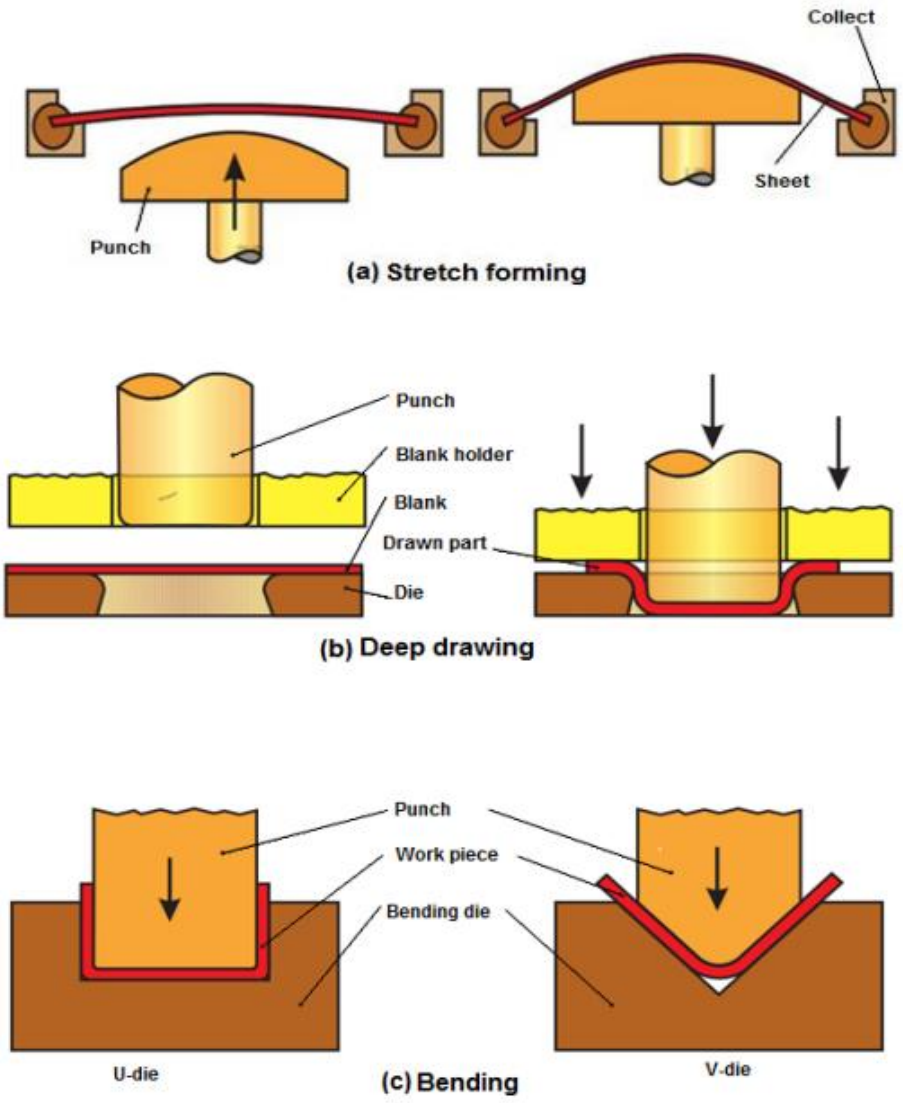

Figure 1.1 Sheet metal forming operation [26]

Bending is a fabrication process wherein sheet metal is exposed to bending force to create curved components or sections. Common bending operations include V-bending and U-bending, among others (Figure 1.1). During bending, the exterior of the sheet experiences tensile stress, while the interior undergoes compressive stress. The alteration in bend angle resulting from the material's elastic recovery post-bending is termed springback, which can be mitigated by incorporating appropriate allowances

in the tools. Complex sheet stampings entail a synthesis of the aforementioned procedures. The production of the majority of vehicle and aerospace components entails both stretching and drawing, along with accompanying processes such as bending, unbending, and flanging [27].

1.2 Formability

In sheet metal forming, formability refers to the capacity of a sheet metal to be shaped into a specific desired configuration without experiencing failure. The extent of deformation attainable in a single stage is constrained by the initiation of tensile instability (necking) and/or fracture resulting from excessive thinning of the blank. Necking and, at times, excessive thinning are the primary limiting factors in sheet metal operations. The formability of sheet metals is typically assessed by laboratory simulation experiments. In simulated tests, the material is distorted in a manner that closely mimics a certain forming process. This section provides a quick explanation of many regularly utilized simulated test methodologies.

1.2.1 Erichsen and Olsen tests

Figure 1.2 presents the schematic of the Erichsen and Olsen tests. The initial assessment for determining the formability of sheet metals was introduced by Erichsen [28]. A circular specimen with a diameter of 27mm is secured between two grips and deformed with a hemispherical punch of 20mm diameter until necking or failure occurs, at which point the cup height is measured. The greater the cup height, the superior the material's formability during stretching. Subsequently, Olsen [29] introduced a comparable test utilizing altered tool and blank dimensions. Inadequate repeatability and unpredictability in clamping (material draw-in) restrict the application of these tests.

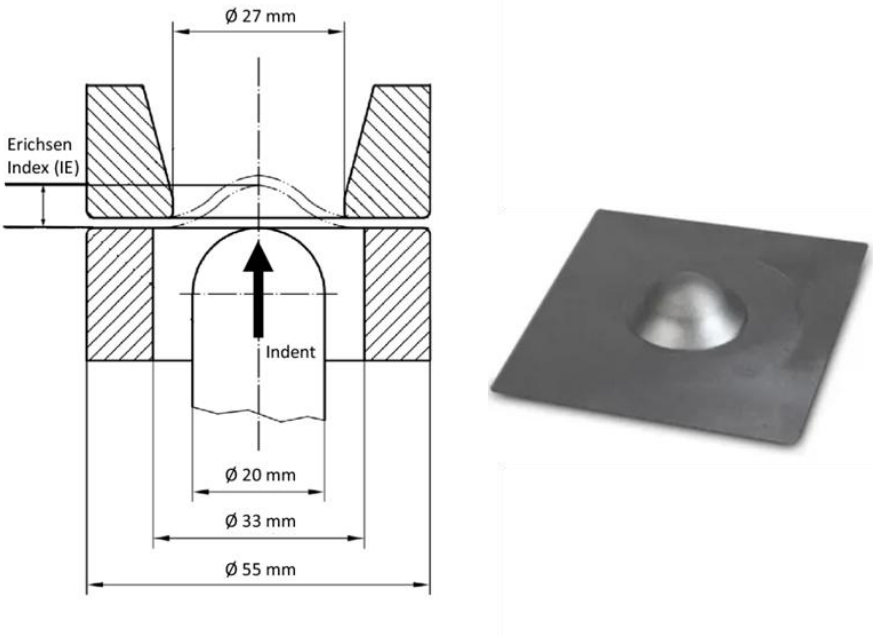

Figure 1.2 Tool for Erichsen and Olsen tests and a tested sample [30]

1.2.2 Limiting dome height test

Hecker [31] introduced a formability test wherein the blank is deformed over a hemispherical punch with a diameter of 101.6 mm, incorporating a drawbead within the die plates. In limit dome height test the material is entirely secured by employing a drawbead, which prevents the material from being drawn into the die, resulting in pure biaxial stretching during the test. Figure 1.3 displays the schematic of the tooling with a tested sample. The formability is assessed by measuring the dome height at the initiation of necking or failure. This assessment is usually referred to as the limiting dome height (LDH) test.

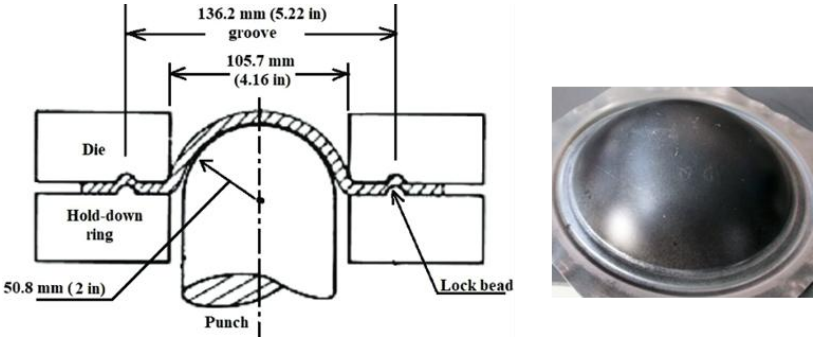

Figure 1.3 Limiting dome height test and a tested sample [31]

1.2.3 OSU test

A further test was introduced by Wagoner et al. [32], referred to as the Ohio State University (OSU) test, to ascertain the limiting dome height under plane strain conditions. The failure punch height serves as an indicator of formability. This test is expedient as it requires the evaluation of only one specimen width (124 mm) to achieve a plane-strain failure. The test configuration employs a flat elliptical punch rather than the hemispherical punch utilized in the LDH test as shown in Figure 1.4. Various coated and uncoated sheet materials were evaluated using both flat elliptical and hemispherical punches, and the results were compared. OSU testing demonstrated greater stability and repeatability in comparison to LDH tests.

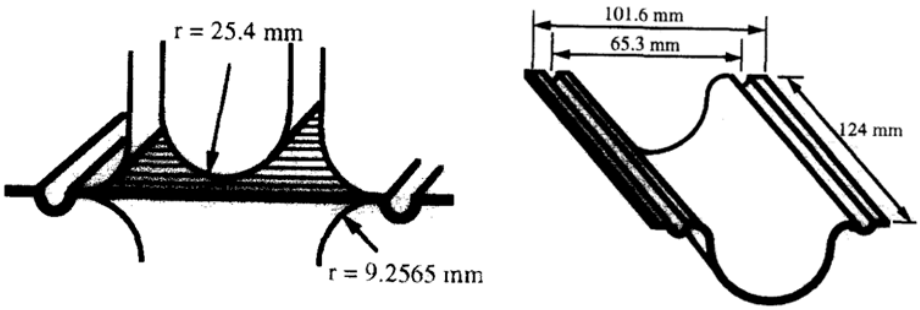

Figure 1.4 OSU test and a tested blank sample [33]

1.2.4 Hydraulic bulge test

A hydraulic bulging test [34] is another method for assessing the formability of a sheet under biaxial stretching. The configuration comprises a pressure chamber and a clamping apparatus. Pressure can be generated utilizing fluid or gas as shown in Figure 1.5. The bulge height at which material failure occurs is utilized to assess formability. This test's advantage lies in the absence of friction between the tool and the workpiece, facilitating equibiaxial stretching and resulting in increased total strain.

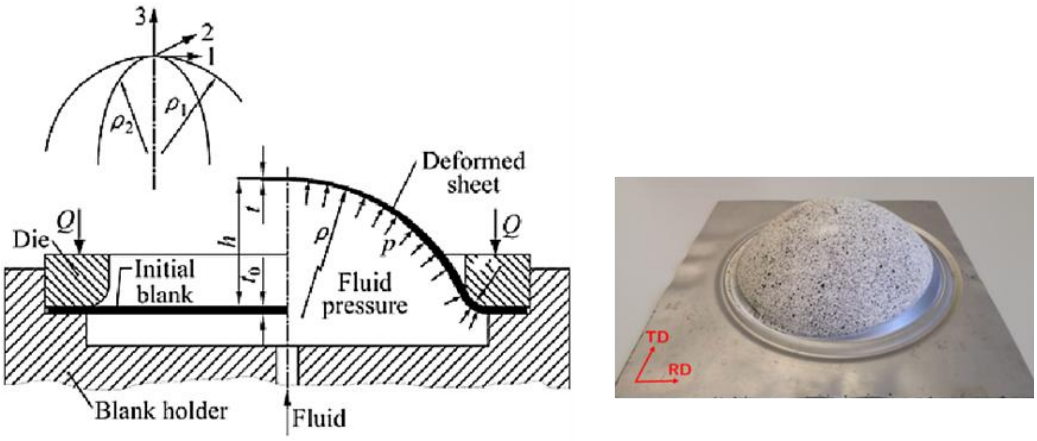

Figure 1.5 Hydraulic bulge test and a tested sample [35]

1.2.5 Swift cup drawing test

All the aforementioned tests are employed to assess the formability of a sheet under stretching conditions. The Swift flat bottom cup test [36] is a classic method for assessing the drawability of a sheet. This test employs a flat-bottom punch with a diameter of 50mm to draw circular blanks of varying diameters into the die as shown in Figure 1.6. The blank diameter is progressively enlarged to ascertain the limiting draw ratio (LDR), defined as the ratio of the largest blank diameter that may be pulled without failure to the diameter of the punch.

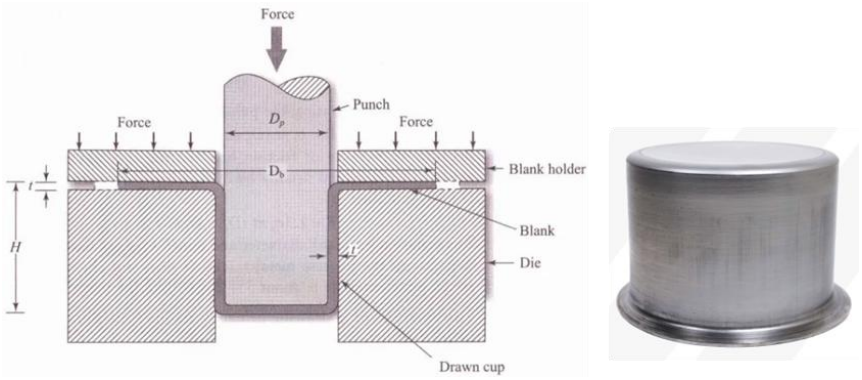

Figure 1.6 Swift cup test and a drawn cup [33]

1.2.6 Fukui conical cup test

Fukui [33] proposed an alternative testing method to assess formability in a combined mode of deformation (stretching and drawing). The test apparatus comprises a spherical ball with a diameter of 22 mm and a conical die featuring a 60° included angle as shown in Figure 1.7. The punch exerts stress on the ball, causing the unsupported circular blank to distort until a failure in the sheet is evident. During deformation, the material experiences elongation from the flange area. The hole is far larger than the ball, necessitating the development of a conical cup. The formability is assessed by the base diameter of the cup.

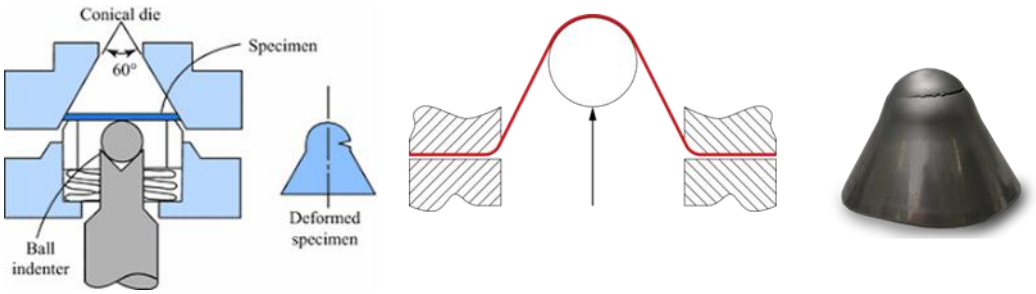

Figure 1.7 Fukui conical cup test and a tested sample [33]

1.3 Forming limit diagram

A forming limit diagram, commonly referred to as the Forming Limit Curve (FLC), is utilized to anticipate the forming behaviour of sheet metal. This graph forecasts the material's failure

zone. To conduct the Forming Limit Diagram experiment, circular markings are applied to the sheets. The sheet is subsequently distorted in a press. before establishing The blank holder secures the sheet and facilitates material locking to enable adequate deep drawing. When the blank is secured at a specified pressure, the punch advances toward the sheet and deforms it. When the sheet is stretched, circles become warped, resulting in an ellipse, as illustrated in Figure 1.8.

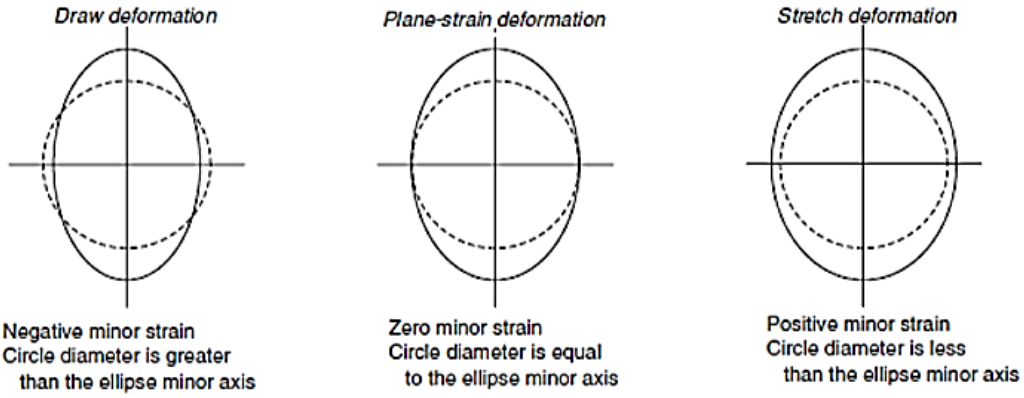

Figure 1.8 Circles deformed into ellipses in different modes of deformation

Let the initial diameter of the circle be d1, and the end diameters of the deformed circle, namely the ellipse, be d_2minor (minor diameter) and d_2major (major diameter).Principal strains can be determined as follows: the major strain, aligned with the major axis of the ellipse, is expressed as $\ln(d_{2major}/d_1)$, while the minor strain is represented as $\ln(d_{2minor}/d_1)$. The values at failure and necking indicate the failure and necking conditions, while strain levels distant from necking signify a safe situation. A graph depicting the amalgamation of major and minor strain associated with failure, necking, and the safe zone results in the developing limit diagram, commonly referred to as the Keeler-Goodwin diagram.

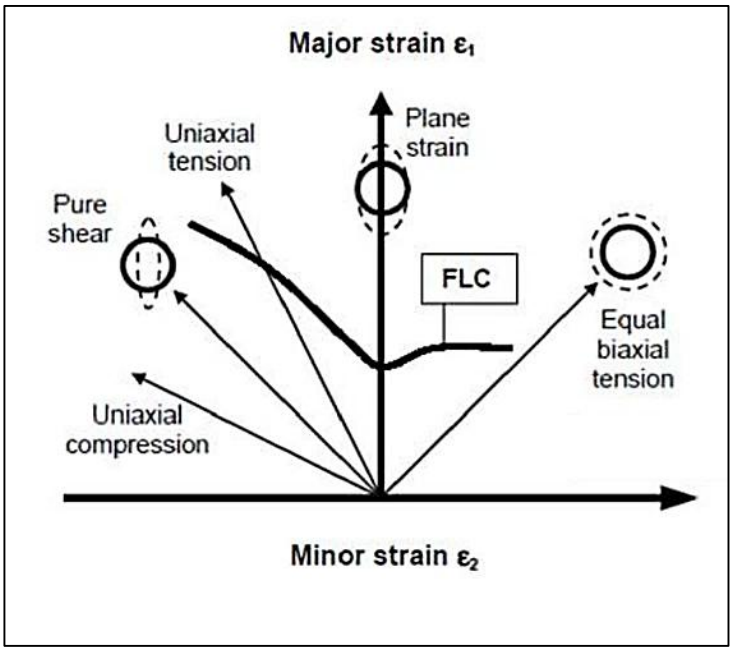

Figure 1.9 A typical forming limit diagram

Figure 1.9 illustrates the threshold beyond which the forming operation may result in necking or fracture. The strain data above the curve indicates the regions of failure. The curve on the left side represents limit strains recorded from samples subjected to combined tension and compression deformation. The curve on the right illustrates the limiting stresses recorded from samples deformed under biaxial tension. The principal strain value, when the secondary strain is zero, signifies a condition of plain strain.

1.3.1 Important material parameters which affect formability

The mechanical properties which affect the formability of sheet metals are strain hardening exponent, anisotropy and thickness of the material.

1.3.1.1 Strain Hardening exponent

The strain hardening exponent (n) signifies a material's capacity to uniformly distribute strain under tensile stress. It shows a material's ability to undergo work hardening, which occurs when the flow stress increases with increasing plastic strain. A larger n number suggests a stronger potential for uniform plastic deformation, since the material can transfer strain more

effectively and postpone the beginning of localized necking. This improves formability by allowing the sheet to withstand larger strains before failing, which is especially useful in forming processes like deep drawing and stretch forming. In contrast, materials having a low strain hardening exponent tend to localize deformation quickly, resulting in early necking and poor formability. As a result, a larger strain hardening exponent is typically related with improved resistance to instability, increased forming limits, and overall performance in sheet metal forming processes.

Anisotropy

The normal anisotropy ($\bar{R}$) and planar anisotropy (ΔR) influences drawability and earing of the sheets during deep drawing [37]. R value (plastic strain ratio) represents the ratio of true strain in width to true strain in thickness. The R value, defined as the ratio of true strain in the width direction to true strain in the thickness direction, provides a direct assessment of a material's resistance to thinning under tensile deformation. Higher average normal anisotropy ($\bar{R}$) suggests superior drawability, since the sheet may undergo greater plastic deformation with lower thickness reduction, minimizing the danger of tearing or fracture. Planar anisotropy (ΔR) is the fluctuation of R values with orientation relative to the rolling direction, causing non-uniform material flow while drawing. Higher ΔR values cause significant earing defects along the cup rim, resulting in increased material waste and post-processing requirements. Therefore, achieving a high $\bar{R}$ combined with a low ΔR is essential for enhancing deep drawability while suppressing earing tendencies in sheet metal forming operations.

Thickness

Increased sheet thickness enhances formability. It has a direct impact on stress distribution, strain accommodation, and failure resistance throughout the forming process. Thicker sheets have better formability because they can resist higher forming loads and accommodate larger plastic strains before experiencing localized necking or fracture. The higher thickness

increases resilience to thinning, improves through-thickness stress support, and decreases ripping during procedures like deep drawing and stretching. Thinner sheets, on the other hand, are more susceptible to rapid thickness decrease, strain localization, and early failure, especially in complicated stress conditions. Increased sheet thickness results in increased forming forces and material consumption, which must be balanced against design and production limits. As a result, an appropriate sheet thickness is required to enable increased formability while preserving efficiency and structural integrity in forming applications. In the necking zone, elevated limiting stresses arise due to the increased thickness of the sheet metal [38]. The configuration of the neck is contingent upon the strain rate sensitivity index (m) of the material. Necks exhibit a more gradual profile in materials with a greater modulus. Aluminium alloys with lower m exhibit significantly sharper necks. The presence of a sharper neck likely diminishes the significance of the thickness effect [39].

Ductility

Sheet ductility is a fundamental material attribute that substantially influences formability since it determines the amount of plastic deformation that a sheet can withstand before fracture. Materials with high ductility can withstand bigger strains through consistent plastic flow, allowing complicated shapes to be formed without breaking or tearing during forming processes such as deep drawing, bending, and stretching. Enhanced ductility improves strain redistribution under multiaxial stress states, slows the development of localized necking, and enhances the sheet's forming limit. Sheets with low ductility, on the other hand, have restricted plastic deformation capability, resulting in premature fracture and reduced formability, especially in places subjected to high tensile stresses. Higher sheet ductility is directly related to improved formability, forming reliability, and design flexibility.

.

1.4 Aluminium alloys

The unique combinations of properties provided by aluminium and its alloys make aluminium one of the most versatile, economical, and attractive metallic materials for a broad range of uses from soft, highly ductile wrapping foil to the most demanding engineering applications. Aluminium alloys are second only to steels in use as structural metals. Aluminium has a density of only 2.7 g/cm3, approximately one-third as much as steel (7.83 g/cm3). One cubic foot of steel weighs about 490 lb; a cubic foot of aluminium, only about 170 lb. Such light weight, coupled with the high strength of some aluminium alloys (exceeding that of structural steel), permits design and construction of strong, light weight structures that are particularly advantageous for anything that moves space vehicles and aircraft as well as all types of land- and water-borne vehicles. Aluminium resists the kind of progressive oxidization that causes steel to rust away. The exposed surface of aluminium combines with oxygen to form an inert aluminium oxide film only a few ten-millionths of an inch thick, which blocks further oxidation. And, unlike iron rust, the aluminium oxide film does not flake off to expose a fresh surface to further oxidation. If the protective layer of aluminium is scratched, it will instantly reseal itself. The thin oxide layer itself clings tightly to the metal and is colourless and transparent invisible to the naked eye. The discoloration and flaking of iron and steel rust do not occur on aluminium. Appropriately alloyed and treated, aluminium can resist corrosion by water, salt, and other environmental factors, and by a wide range of other chemical and physical agents. The corrosion characteristics of aluminium alloys are examined in the section “Effects of Alloying on Corrosion Behaviour” in this article.

Aluminium surfaces can be highly reflective. Radiant energy, visible light, radiant heat, and electromagnetic waves are efficiently reflected, while anodized and dark anodized surfaces can be reflective or absorbent. The reflectance of polished aluminium, over a broad range of wave lengths, leads to its selection for a variety of decorative and functional uses. Aluminium typically displays excellent electrical and thermal conductivity, but specific alloys have been

developed with high degrees of electrical resistivity. These alloys are useful, for example, in high-torque electric motors. Aluminium is often selected for its electrical conductivity, which is nearly twice that of copper on an equivalent weight basis. The requirements of high conductivity and mechanical strength can be met by use of long-line, high-voltage, aluminium steel-cored reinforced transmission cable. The thermal conductivity of aluminium alloys, about 50 to 60% that of copper, is advantageous in heat exchangers, evaporators, electrically heated appliances and utensils, and automotive cylinder heads and radiators. Aluminium is nonferromagnetic, a property of importance in the electrical and electronics industries. It is nonpyrophoric, which is important in applications involving inflammable or explosive-materials handling or exposure. Aluminium is also non-toxic and is routinely used in containers for food and beverages. It has an attractive appearance in its natural finish, which can be soft and lustrous or bright and shiny. It can be virtually any colour or texture. The ease with which aluminium may be fabricated into any form is one of its most important assets. Often it can compete successfully with cheaper materials having a lower degree of workability. The metal can be cast by any method known to foundrymen. It can be rolled to any desired thickness down to foil thinner than paper. Aluminium sheet can be stamped, drawn, spun, or roll formed. The metal also may be hammered or forged. Aluminium wire, drawn from rolled rod, may be stranded into cable of any desired size and type. There is almost no limit to the different profiles (shapes) in which the metal can be extruded. Different types of Aluminium alloys are described below:

1xxx Series. Aluminium of 99.00% or higher purity has many applications, especially in the electrical and chemical fields. These grades of aluminium are characterized by excellent corrosion resistance, high thermal and electrical conductivities, low mechanical properties, and excellent workability. Moderate increases in strength may be obtained by strain hardening. Iron and silicon are the major impurities.

2xxx Series. Copper is the principal alloying element in 2xxx series alloys, often with magnesium as a secondary addition. These alloys require solution heat treatment to obtain optimum properties; in the solution heat-treated condition, mechanical properties are similar to, and sometimes exceed, those of low-carbon steel. In some instances, precipitation heat treatment (aging) is employed to further increase mechanical properties. This treatment increases yield strength, with attendant loss in elongation; its effect on tensile strength is not as great. The alloys in the 2xxx series do not have as good corrosion resistance as most other aluminium alloys, and under certain conditions they may be subject to intergranular corrosion. Therefore, these alloys in the form of sheet usually are clad with a high-purity aluminium, a magnesium-silicon alloy of the 6xxx series, or an alloy containing 1% Zn. The coating, usually from 2 to 5% of the total thickness on each side, provides galvanic protection of the core material and thus greatly increases resistance to corrosion. Alloys in the 2xxxseries are particularly well suited for parts and structures requiring high strength-to-weight ratios and are commonly used to make truck and aircraft wheels, truck suspension parts, aircraft fuselage and wing skins, structural parts, and those parts requiring good strength at temperatures up to 150 °C (300 °F).

3xxx Series. Manganese is the major alloying element of 3xxx series alloys. These alloys generally are non-heat-treatable but have about 20% more strength than 1xxx series alloys. Because only a limited percentage of manganese (up to about 1.5%) can be effectively added to aluminium, manganese is used as a major element in only a few alloys. However, one of these, the popular 3003 alloy, is widely used as a general-purpose alloy for moderate-strength applications requiring good workability.

4xxx Series. The major alloying element in 4xxx series alloys is silicon, which can be added in sufficient quantities (up to 12%) to cause substantial lowering of the melting range without producing brittleness. For this reason, aluminium-silicon alloys are used in welding wire and

as brazing alloys for joining aluminium, where a lower melting range than that of the base metal is required. Most alloys in this series are non-heat treatable, but when used in welding heat-treatable alloys, they pick up some of the alloying constituents of the latter and so respond to heat treatment to a limited extent. The alloys containing appreciable amounts of silicon become dark grey to charcoal when anodic oxide finishes are applied and hence are in demand for architectural applications. Alloy 4032 has a low coefficient of thermal expansion and high wear resistance; thus, it is well suited to production of forged engine pistons.

5xxx Series. The major alloying element in 5xxx series alloys is magnesium. When it is used as a major alloying element or with manganese, the result is a moderate-to-high-strength work hardenable alloy. Magnesium is considerably more effective than manganese as a hardener, about 0.8% Mg being equal to 1.25% Mn, and it can be added in considerably higher quantities. Alloys in this series possess good welding characteristics and good resistance to corrosion in marine atmospheres. However, certain limitations should be placed on the amount of cold work and the safe operating temperatures permissible for the higher-magnesium alloys (over ~3.5% for operating temperatures above ~65 °C, or 150 °F) to avoid susceptibility to stress-corrosion cracking.

6xxx Series. Alloys in the 6xxx series contain silicon and magnesium approximately in the proportions required for formation of magnesium silicide (Mg2Si), thus making them heat treatable. Although not as strong as most 2xxx and 7xxx alloys, 6xxx series alloys have good formability, weldability, machinability, and corrosion resistance, with medium strength. Alloys in this heat-treatable group may be formed in the T4 temper (solution heat treated but not precipitation heat treated) and strengthened after forming to full T6 properties by precipitation heat treatment.

7xxx Series. Zinc, in amounts of 1 to 8%,is the major alloying element in 7xxxseries alloys, and when coupled with a smaller percentage of magnesium results in heat-treatable alloys of

moderate to very high strength. Usually other elements, such as copper and chromium, are added in small quantities. Dilute additions of scandium also improve properties. 7xxx series alloys are used in airframe structures, mobile equipment, and other highly stressed parts. Higher strength 7xxx alloys exhibit reduced resistance to stress corrosion cracking and are often utilized in a slightly overaged temper to provide better combinations of strength, corrosion resistance, and fracture toughness.

8xxx series alloys constitute a wide range of chemical compositions. For example, improved elevated-temperature performance is achieved through the use of dispersion-strengthened Al-Fe-Ce alloys (e.g.,8019) or Al-Fe-V-Si alloys (e.g., 8009) made by powder metallurgy processing. Lower density and higher stiffness can be achieved in lithium-containing alloys (e.g.,8090). The latter alloy, which is precipitation hardenable, has replaced medium-to-high strength 2xxx and 7xxx alloys in some aircraft/aerospace applications (e.g., helicopter components).

1.4.1 Importance of lightweight sheet materials

The reduction of automotive weight while preserving functional requirements is a primary objective of engineering design and manufacture, aimed at conserving materials, energy, and prices, as well as minimizing environmental impact. A reduction of only 10% in vehicle weight is projected to yield a 6 - 8% enhancement in fuel efficiency, accompanied by a corresponding decrease in exhaust emissions [39 - 40]. Aluminum (Al) alloys present significant opportunities for weight reduction in the automotive sector by substituting prevalent materials [41 – 42], such as various grades of steel, due to their superior strength-to-weight ratio, thermal characteristics, exceptional corrosion resistance, 90% recyclability, and ease of machinability. The utilization of aluminum alloys enhances both fuel efficiency and safety. Aluminum alloys of equivalent weight to steel absorb twice the energy after a collision, hence enhancing passenger safety. In 2015, the average aluminum content in vehicles was 350 lbs (160 kg) and

is projected to reach 547 lbs (250 kg) by 2025, representing a 37% increase (Figure 1.10). Significant growth is noted in automotive body and closures. The predominant shipments of aluminum goods consist of sheets and plates. The enhancement of mechanical characteristics in aluminum alloys through alloying and heat treatment has expanded their applications in the automotive and aerospace sectors [43]. Figure 1.11 illustrates many applications of aluminum alloys in the automotive industry. Despite the significant potential of aluminum alloys for automotive and other applications aimed at weight reduction and fuel efficiency, the substitution of steel with aluminum alloys in the production of complex sheet metal components remains challenging with current conventional manufacturing processes due to the inadequate formability of aluminum alloys at ambient temperature. Consequently, sophisticated forming techniques are required to enhance their formability. Improvements are anticipated with the application of specialized forming processes, such sheet hydroforming, superplastic forming, and high energy rate forming, which will be briefly described next.

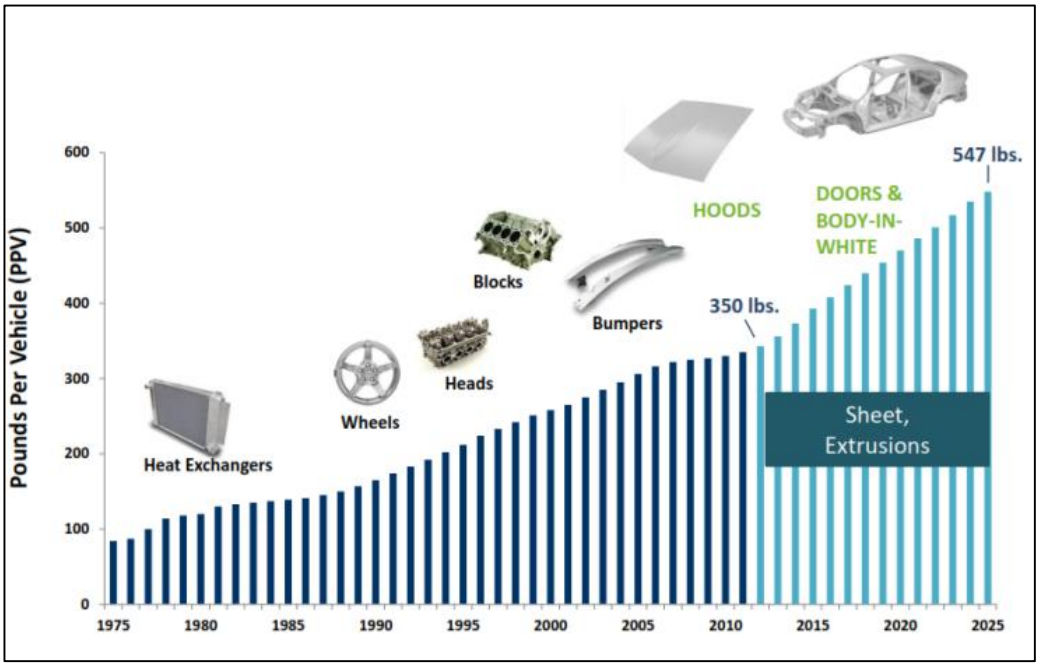

Figure 1.10 Aluminum growth in automotive industry [44]

Figure 1.11 Applications of aluminum alloys in automobiles [45]

1.4.2 Aluminium alloys application in automobile body parts

Global environmental requirements for autos have become rigorous and difficult to comply with. They save natural resources, diminish energy consumption, alleviate environmental pollution, improve vehicle safety, and ensure comfortable driving conditions. The pressing concern is the minimal energy consumption for conservation purposes and the reduction of CO2 emissions to address global warming. Improving engine and drivetrain efficiency, reducing running resistance, and decreasing vehicle weight are fundamental ways to lower fuel consumption. In terms of weight reduction, strategies encompass reducing the size of the autobody, modifying the structural design, and replacing traditional materials with lighter substitutes.

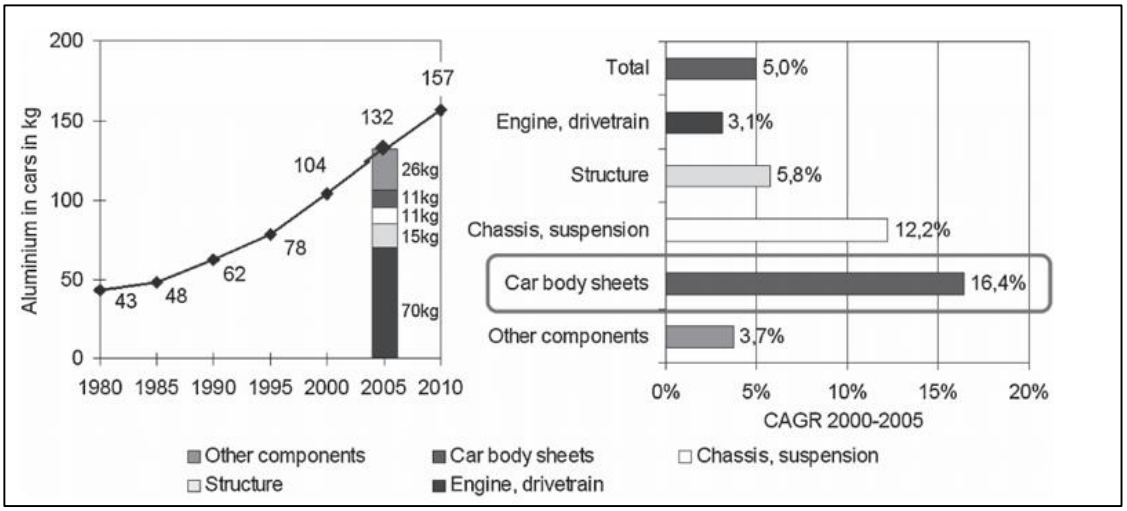

Figure 1.12 Growth of Aluminium in car body application

Reducing the size of automobiles is the most effective method for weight reduction; yet, dimensions tend to increase to accommodate safety requirements and consumer demand. Moreover, the installation of air-conditioning units and additional accessories increases the weight of a vehicle. The transition from a frame-type to a frameless monocoque body structure in passenger cars led to a reduction in weight. Japanese automotive manufacturers began to implement high-strength steel sheets (HS) in the exterior panels of vehicle bodies, marking a

pivotal shift during the two oil crises. Subsequently, several types of high-strength materials with excellent formability were created, resulting in a progressively increasing use rate of high-strength materials. To attain weight reduction in response to stringent fuel consumption regulations, it is essential to substitute conventional materials with advanced lightweight alternatives. This study presents the current status of the development and application of sheet materials for reducing autobody weight and discusses the challenges associated with these materials in sheet formation. Enhancing engine and drivetrain efficiency, minimizing running resistance, and reducing autobody weight are primary strategies to decrease fuel consumption.

1.4.3 Sheet materials for weight reduction of autobody

The practical employment of aluminum alloys in automobiles is anticipated due to their lightweight properties. The utilization of aluminum alloys in engine cylinders and wheels is sophisticated, with the typical weight proportion of aluminum components being 5 to 7% of the total weight of mass-produced passenger vehicles in Japan. The utilization of aluminum alloy sheets for autobody components has risen since the initial implementation of A1-Mg-Zn alloy in 1985. Certain separable components, including the hood (both outer and inner), front fender, and sunroof panels of many passenger vehicles, are constructed from aluminum alloy sheets. Due to the higher cost of aluminium alloy sheets compared to steel sheets, aluminium alloys are utilized exclusively in specific types of passenger vehicles. A automobile with a white exterior entirely constructed from aluminum alloys has been available on the market. The development of extruded aluminium alloy forms for structural components is ongoing. Each of these materials possesses distinct advantages and downsides. 1) Material and processing costs, 2) quality and stability, 3) reliable supply, 4) functional attributes such as luminosity and strength, 5) productivity in operations such as forming and welding, and 6) disposal and recycling post-use. From the perspective of sheet material formability, numerous indices of material attributes exist for selection. In the press forming of big, complex components like automotive skin panels, it is essential to investigate numerous adverse events

throughout the forming process and to assess the overall impact of material attributes and forming processes on performance. Yoshida proposed distinguishing fitting behavior, shape fixing, and fracture behavior to enhance the knowledge of the deformation behavior of metal sheets, based on an analysis of forming flaws and their countermeasures in the press shop [46]. The formability of sheet metal should be assessed based on three properties: fitability, shape fixability, and fracture resistance, which collectively define total formability.

Fracture resistance refers specifically to formability. Formability, as determined by fracture resistance, is categorized as deep drawability, stretchability, stretch flangeability, and bendability [46]. Flttability refers to the extent of deviation of a manufactured component from its intended shape, specifically the degree of geometric imperfections such as wrinkles and surface deflections. Fixability refers to the degree of retention of shape and dimension of a produced part post-stamping. During stamping, springback and minor surface deflection occur due to elastic recovery from the release of residual stresses, with material parameters significantly impacting the primary adverse events observed in the forming process [47]. The sheet metals must be chosen based on their overall formability.

1.4.4 Aluminium alloys application in TWBs

Aluminium has long been entrenched in the automotive sector. The prevailing trend in the automotive and aerospace industries is to create designs that minimize vehicle weight, hence reducing energy consumption and environmental impact in future vehicles. It is utilized for structural components, closures, and external attachments, including cross beams, doors, and hoods. Pure aluminum structures have been created and utilized. They are mostly utilized in premium automobiles like the Audi A8 and certain niche vehicles, such as the BMW Z8, due to their relatively elevated material and production expenses. Nonetheless, aluminium presents numerous advantages and novel opportunities, and will assume a more significant position in the automotive sector in the future. The utilization of TWBs for automotive components is

influenced by a broad spectrum of demands, contingent upon particular specifications. This encompasses economic efficiency, safety, recyclability, and lightweight performance. Figure 1.13 illustrates the application of a TWB constructed from aluminium alloys with two distinct thicknesses.

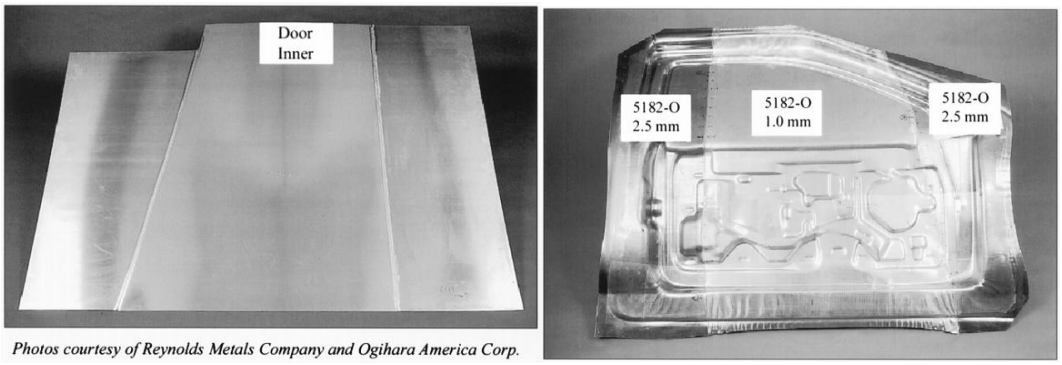

Figure 1.13 Application of a TWB in inner door panel for an automobile [47]

1.4.5 Characteristics of aluminium alloy sheets

Aluminium alloys utilized in autobody applications primarily consist of three types of alloying element compositions. Heat-treatable 2000 series A1-Cu alloys, 6000 series AI-Mg-Si alloys, and non-heat-treatable 5000 series A1-Mg alloys have been utilized in automotive body construction. In the USA, 2000 series AI-Cu alloys are utilized alongside 5000 series Al-Mg alloys; however, in Japan, 2000 series alloys have not been employed due to inadequate anti-corrosion resistance. The mechanical qualities of aluminium alloys utilized for stamping are often characterized as follows: The strength level (YP, TS) is inferior to that of steels. The elastic constant (Young's modulus), E, is approximately one-third that of steel. The elongation, especially local elongation, is minimal. Discontinuous deformation phenomena, including yield-point elongation and jerky flow resulting from the P-L effect, are present. The plastic anisotropy, denoted as the r value, is low, measuring (below 1.0) 6) Comparatively pliable and susceptible to surface damage Consequently, it may be concluded that aluminium alloy sheets are more challenging to form in press operations compared to steel sheets. Aluminium firms

are developing new alloy sheets with high strength and high elongation for autobody applications, particularly A1-Mg 5000 series alloys. The overall elongation for 5000 series AI-Mg alloys reaches up to 36%, while the tensile strength attains up to 300 MPa. The overall elongation for the 6000 series A1-Mg-Si reaches up to 32%, and the tensile strength (TS) can attain up of 290 MPa.

1.5 Fundamental principles of friction stir welding

The two phenomena involved in the Friction Stir Welding (FSW) process are the thermal generation from tool friction on the material and the material flow resulting from the tool's stirring action. Experiments and numerical models are extensively employed to enhance the comprehension of these phenomena. Nevertheless, the numerical technique provides insight into processes that are challenging to quantify through experimentation. Predictive simulations must consider the following aspects: linked friction and heat generation, plastic flow and slip surface formation, and, ultimately, heat and material flow. [48].

1.5.1 Heat generation

Despite the fact that the energy input of FSW is comparable to or less than that of arc welding [49], the heat is disseminated over a broader area by the shoulder, in contrast to a concentrated arc. Furthermore, the close contact between the sample and the backing plate functions as a heat sink, effectively dissipating heat. Consequently, FSW is regarded as a cold-welding method, resulting in minimal residual stress and distortion. Heat is primarily produced by the friction between the tool shoulder and the workpiece surface, then augmented by the extensive plastic deformation and pin friction. In literature, the pin contribution to the heating process is reported to range from 2% to 51% [50]. Nonetheless, a prevailing tendency indicates a contribution of less than 5%. Dong et al. explicitly delineate the impact of each process component (shoulder friction, pin friction, and plastic work) on heating during AA6061 T6 welding [51]. In the scenario of friction exclusively, the temperature beneath the shoulder

(about 350°C) is comparable to that beneath the pin (300°C). Nevertheless, this warmth is disseminated over a broader surface area, resulting in an increased energy intake. Furthermore, the heat produced by the pin is in proximity to the surface backing, where heat extraction is optimal. These two facts validate the predominant role of shoulder friction in heat generation during the FSW process. In the context of plastic deformation alone, the global temperature remains comparatively low (about 100°C beneath the tool) in contrast to frictional heating (250°C), except beneath the pin where the strain is elevated. This simulation validates the primary influence of friction on heating. Ultimately, when the two phenomena are integrated The global temperature beneath the tool is around 250°C, with localized hotter regions beneath the shoulder and the pin exceeding 350°C.

The thermal energy generated by shoulder friction can be quantified [52]. This equation demonstrates that power input escalates with an increase in the friction coefficient, forging force (i.e., the normal load exerted by the tool), rotating speed, and shoulder diameter.

$$q_0 = \frac{4}{3}\pi^2 \mu P N R^3$$

37 Where, q_0: net power (W), μ: friction coefficient between the piece and the tool, P: pressure distribution (MPa), N: rotational speed (rpm), R: surface radius (mm).

10 The friction at the tool's forefront creates a plasticized zone, which is then displaced around the tool and deposited on the receding side. This procedure is seen as continuous throughout the workpiece. However, if melting transpires in front of the tool due to excessive heating,

10 reduced friction is produced due to the slippage between the tool and the molten metal. As the temperature diminishes, the material reverts to a solid form and vice versa. This phenomenon may restrict the utilization of elevated tool revolutions and consequently the application of high welding speeds.

1.5.2 Material flow

The intricate flow surrounding the FSW tool can be divided into three more straightforward flow components. (i) The initial component can be regarded as a cylinder of the welded material undergoing rigid body rotation, delineated from the remainder of the weld by a cylindrical shearing surface, which represents a velocity discontinuity (refer to Figure 1.14 (a)). The revolving cylinder is designed to be affixed to the FSW tool, with its rotational speed matching that of the tool spindle. The borders extend toward the tool shoulder to accommodate the shoulder's contour. Furthermore, its thickness marginally rises on the retreating side to facilitate the metal transfer to the back of the pin as the pin advances. For thinner materials, this cylinder may be characterized as a conical region to accommodate the reduced pin length. The shearing surface is consequently situated between the shoulder corner and the pin base. (ii) The second flow component is a homogenous and isotropic flow field that is identical in magnitude and opposite in direction to the welding speed (refer to Figure 1.14 (b)). This uniform translation is commonly referred to as "extrusion movement," drawing an analogy to the corresponding manufacturing process. (iii) The third component is a ring vortex flow that encircles the tool, transporting metal outside, inward at the shoulder, downward internally, and outward in the lower regions of the pin (see to Figure 1.14 (c)). The flow is governed by the threads and/or flutes on the pin and can be inverted if the orientation of the threads or the tool rotation is altered. The vertical motion is vividly highlighted by tracer tests [53], where four threads are positioned along the pin length, allowing a marker to undergo approximately 18 cycles around the pin. This typically results in the disruption and dispersion of the marking. Figure 1.14 (d) illustrates that the amalgamation of these three flows produces straight-through and vortex currents contingent upon the location. The material near the advancing side traverses a longer arc within the spinning cylinder and is subjected to the axial flow of the ring vortex for an extended duration. Thus, the vortex current transports the metal to the base of the weld. Consequently, vortex current residues are emitted to the advancing side to preserve

the substance. Conversely, the direct current occupies the receding side, as the metal in this area is briefly subjected to the ring vortex. The proportion of straight-through and vortex currents appears to vary, possibly due to a change in shear versus friction slip on the shoulder surface [39 - 40].

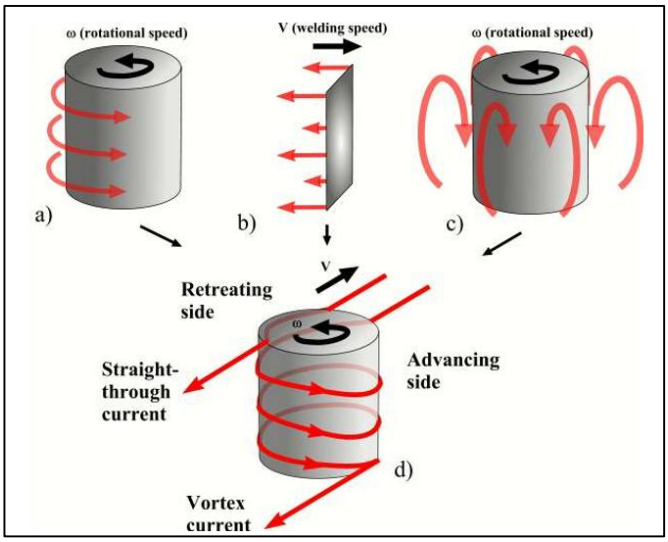

Figure 1.14 Three incompressible flow fields: a) rigid body rotation, b) uniform translation, c) ring vortex, d) combination of the three flow fields.

1.5.3 Tool parameters

As seen in the last chapter, the welding settings have a major impact on the quality of FSW joints. To achieve a solid and consistent weld, the shoulder-pin assembly's rotational speed, the welding speed, the downward forging force, and lastly the tool design must all be optimized [60]. This chapter aims to provide an overview of the many designs and tool factors, such as shoulder diameter, pin size, and shape, that might change the properties of an FSW joint (see Figure 1.15).

Shoulder diameter and shape

The main source of energy input is shoulder size. The achievement of a sound weld is highly dependent on the tool size since the heat input is a function of the shoulder radius to the third power and only relies linearly on the applied forge force and the rotational speed [61 - 62]. Furthermore, shoulder radius also affects Z-axis forge force [63].

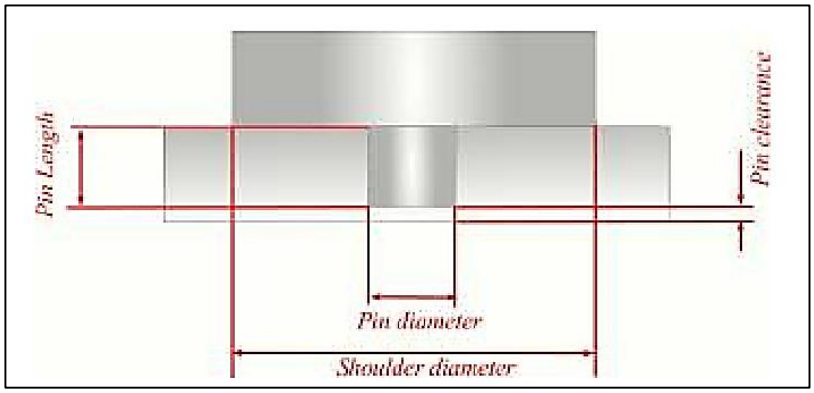

Figure 1.15 Scheme of tool parameters

Pin size and shape

The pin diameter is equal to the sheet thickness for thicknesses ranging from 1 to 8.3 mm. Furthermore, the minimum pin diameter is approximately 3 mm. Once again, the spectrum of the pin diameters may be extensive. For instance, in the welding of 8-mm thick plates, pin diameters ranging from 8 to 13 mm result in defect-free welds. Reynolds et al. investigated the effect of pin diameters ranging from 8 to 12 mm on the X-axis force (i.e., along the welding direction) and the specific weld energy. For this spectrum of tool geometries, the pin diameter did not seem to affect the necessary x-axis force or the specific weld energy.

The clearance is essential to ensure sufficient plastic deformation at the root of the weld. A pin clearance ranging from 0 to 0.5 mm for thicknesses between 1 and 8.3 mm has been documented in the literature, with all these values resulting in fully penetrated welding. If the clearance is insufficiently small, it results in an unbonded region at the root, which may lead

to premature fracture during tensile or bending deformation [64]. It should be noted that a null value for pin clearance is typically avoided, as it may lead to pin damage resulting from the tool penetration during welding. An essential parameter in the design of FSW tools is the ratio of dynamic volume (the volume covered by the pin during rotation) to static volume (the volume of the pin itself). Enhancing this ratio leads to a decrease in void formation within the welds and facilitates more efficient disruption and dispersion of surface oxide within the microstructure [65]. In traditional FSW, the dynamic to static ratio can be enhanced through the incorporation of re-entrant features, flutes, threads, and/or flats machined into the pin [66]. The facets on the pin function as the cutting edge of a cutter. Subsequently, the material becomes confined within the flats and is discharged behind the tool, facilitating comprehensive blending. The most advanced application of this principle is the friction skew swirl method. The footprint technique may be employed to emphasize the exploitation of the dynamic/static ratio. The polar plot of the force footprint illustrates the force vector encountered by the instrument during each rotation.

Optimum tool rotational speed

Rotational speed influences optimal heat input, leading to the formation of finer granules with enhanced plastic flow and sufficient bonding. A higher tool rotational speed results in an increased heat input and a slower cooling rate. It induces metallurgical transformations such as solubilization, reprecipitation, and coarsening of the precipitates. Reduced tool rotational speed leads to decreased frictional heat generation, an increased cooling rate, diminished plastic flow, and insufficient bonding, which ultimately results in coarser particle formation.

Low welding speed

results in high power density responsible for developing coarse grain in stirring zone. Increased welding speed ensures perfect tool work interaction, sufficient plastic flow and formation of fine grains. Lack of bonding takes place if welding speed exceeds the optimum

value. Optimum axial load results in confinement of material within the cavity offers least heat dissipation rate.

Optimum direct axial load

Plasticized material extending from the leading edge to the trailing edge and remaining contained within the weld cavity. Heat loss occurs within the cavity. An increase in axial load leads to greater frictional heat generation, causing material loss due to excessive contact between the tool shoulder and the base plate, which results in a reduction of the cross-sectional area. Increased heat loss occurs as a result of material removal from the base plate, which reduces the available heat for weld formation.

1.6 Work hardening of aluminium alloys

Work hardening, also referred to as strain hardening or deformation hardening, is a phenomenon in which a material's strength enhances during plastic deformation. This section begins with an overview of the effects of work hardening on the material's response. Work hardening is closely associated with the interactions among individual dislocations as well as between dislocations and barriers within the material.

1.6.1 Work hardening

The work hardening behavior of a material is most commonly illustrated by its stress-strain curve, from which the different phases of work hardening can be discerned. Let us initially examine a single crystal subjected to a strain in a direction that activates only one slip system, crystal D in Figure 1.16. Initially, deformation takes place through the phenomenon known as effortless glide, which is depicted as stage I in the stress-strain curve. Since dislocations glide exclusively along a single slip system, the only impediments to their movement are the internal friction between atomic planes and any existing obstacles. Following initial deformation, slip will initiate on additional slip systems (multi-slip), and as dislocations on intersecting slip planes begin to interact, their mobility will be restricted, resulting in an increase in the

material's strength. This second stage of work hardening we are now entering is linear and is characterized by a rapid rate of approximately G/200. The progression from stage I to stage II, as well as the gradient of stage II, is highly influenced by the crystal orientation. If the crystal is oriented such that multiple slip systems are active from the outset, stage I may not manifest at all, as exemplified by crystals A, B, and C in Figure 1.16. During stage II of deformation, the dislocation density will escalate swiftly. However, as the separation between the dislocations diminishes to a sufficiently small distance, they will commence to annihilate each other or recover. The dynamic recovery phenomenon will diminish the dislocation storage rate, resulting in a decrease in the hardening rate.

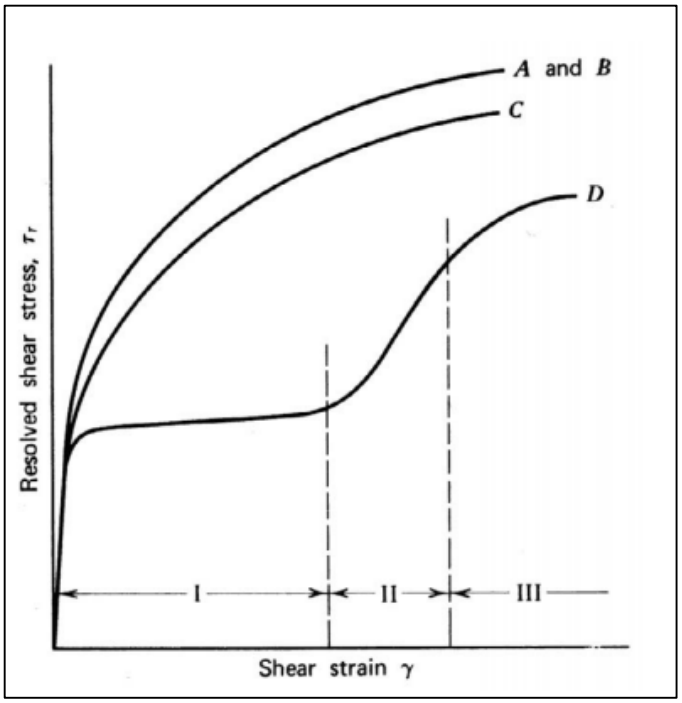

Figure 1.16 Stress-strain curves for single crystals of various orientations. Crystal D, having one active slip system, shows work hardening stages I, II and III. In the multi slip orientations A-C, the material goes directly into stage II. [66]

This is illustrated by the nonlinear region of the stress-strain curve, Stage III, in Figure 1.16. Beyond stage III, there is a progression to a linear stage IV characterized by a low hardening rate. In certain instances, such as ultra-pure aluminium at room temperature and commercially

pure aluminium above approximately 100°C, a stress saturation point (hardening rate = 0) is attained. The work hardening behavior is occasionally represented by the work hardening rate (θ) as a function of stress. Figure 1.16 presents a diagram for copper polycrystals subjected to torsion testing across different temperatures. It is well established that the hardening rate of FCC metals and alloys increases as the temperature decreases, and it scales with the transition stress between stages III and IV, where the scaling parameter an is typically approximately 0.1 for FCC metals.

1.6.2 Precipitation strengthening

Precipitation hardening is the primary mechanism responsible for the fortification of AlMgSi alloys. The fine particulates are dispersed within the comparatively ductile matrix, thereby enhancing the overall mechanical properties. Precipitation hardening, also known as age hardening, is achieved through solution treatment and quenching, during which the second phase remains in solid solution at elevated temperatures. The secondary phase particles precipitate during quenching and aging at a reduced temperature. This phase must be soluble at elevated temperatures and demonstrate decreasing solubility with decreasing temperature to facilitate precipitation hardening. In the case of AlMgSi alloys, the secondary phases are composed of the primary alloying elements magnesium and silicon. A phase diagram illustrating the solubility of Mg and Si as a function of temperature, represented by the Mg2Si phase, is depicted in Figure 1.17.

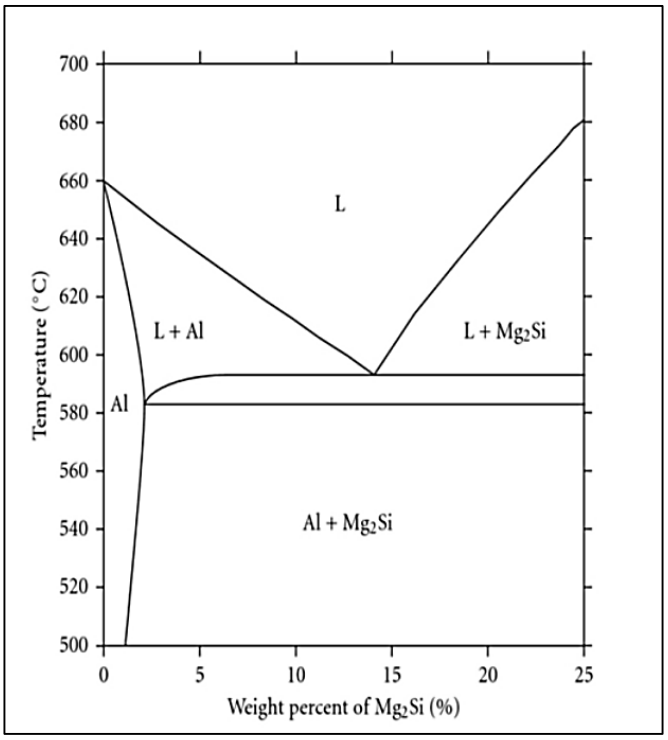

Figure 1.17 Phase diagram showing the solubility of Mg and Si as a function of temperature represented by the phase Mg2Si. [66]

1

The precipitation hardening procedure is conducted through multiple stages. Initially, the alloy is heated to a temperature exceeding the solvus temperature. This is intended to generate a homogeneous solid solution α. The dissolution of alloying elements facilitates the elimination of the second phase and removes segregations such as dislocations and granules within the alloy. After the alloy is cooled from the solubilization temperature, quenching by air or water restricts atomic diffusion toward potential nucleation sites, resulting in the formation of an unstable supersaturated solid solution αss due to reduced solubility at lower temperatures. The supersaturated alloy may then undergo artificial aging. During this phase, the alloy is subjected to heating below the solvus line, typically within the temperature range of 160 to 200°C.

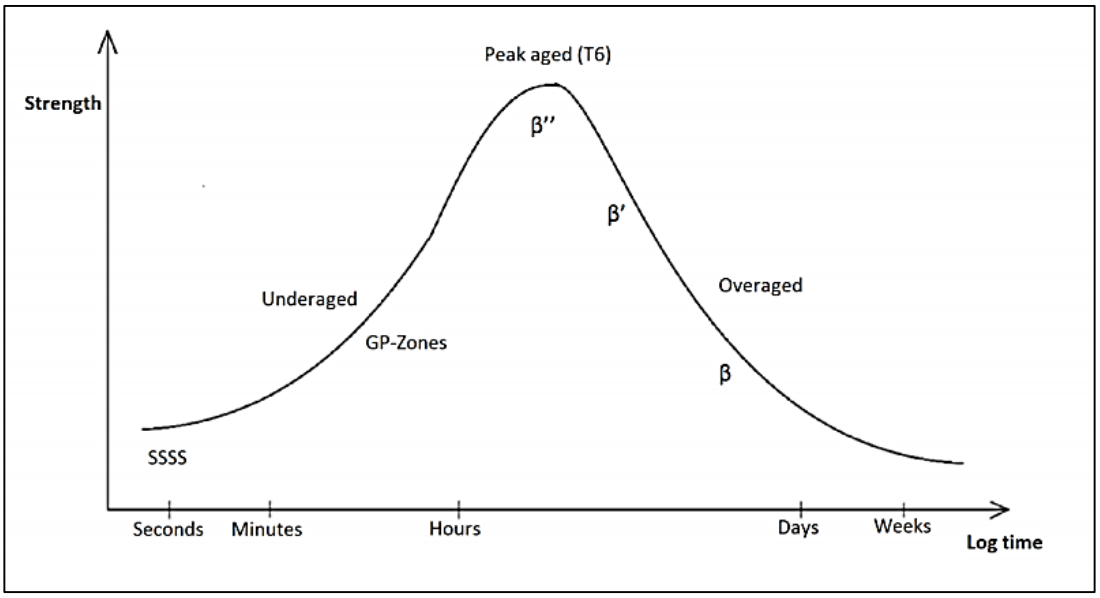

Figure 1.18 Modified sketch of strength evolution during artificial ageing of an AlMgSi-alloy

This allows atoms to diffuse at short distances. Due to the unstable αss phase, the second phase atoms diffuse at several nucleation sites that lead to controlled dispersion of particles. Typical precipitation sequence for AlMgSi-alloys is given in Equation 4 while the composition and the shape of the precipitates. The strengthening effect of the precipitates depends on the particles resistant to dislocation movement. The hardest phase for the aluminium 6xxx series is the β'' and Figure 1.18 shows the strength evolution with ageing time of 6xxx-alloys [68].

1.6.3 Annealing

When any metal undergoes cold working, its crystals are elongated and deformed, resulting in an increased dislocation density and the introduction of imperfections, which enhance the material's strength but reduce its ductility. A decrease in ductility is unfavorable in metal forming processes. To attain a more malleable material, cold-worked metal is subjected to heating within a furnace. If the material is subjected to prolonged heating, the cold-worked metal undergoes several transformations, including (1) recovery, (2) recrystallization, and (3) grain growth.

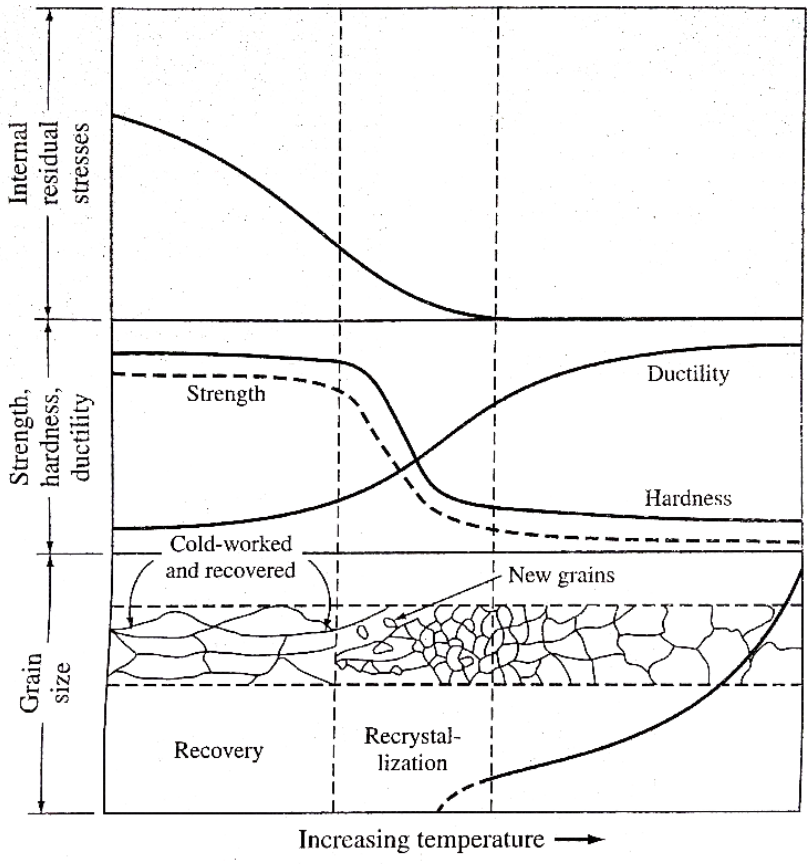

Figure 1.19 Effect of annealing on the structure and mechanical property changes of a cold-worked metal

Figure 1.19 illustrates the influence of temperature on the mechanical properties of the materials. This reheating process, known as annealing, is employed to relax the material. When a material undergoes cold working, strain energy is dissipated within the material as a result of plastic deformation, resulting in an increase in the internal energy of the material. For this reason, the intrinsic energy of a strain-hardened material is always greater than that of an unstrained one.

When a cold-worked material is reheated below its recrystallization temperature, specifically within the recovery temperature range, internal stresses and residual stresses are alleviated. During the recovery process, dislocations reconfigure into a lower energy state facilitated by the provided thermal energy. Due to material recovery, sub-grain boundaries are formed,

characterized as low-angle grain boundaries known as polygonization, which occurs prior to recrystallization. Internal energy decreases as dislocations are annihilated and reorganize into a lower energy state, leading to a minor reduction in strength but a substantial increase in ductility.

During recrystallization, the deformed structure resulting from cold working is entirely substituted by new, recrystallized granules. Primary recrystallization transpires through two principal mechanisms (1) An isolated nucleus may grow in conjunction with a deformed grain. (2) An initial high-angle grain boundary can migrate into a more heavily deformed region of the metal. The annealing procedure comprises three stages: (1) heating to specified temperatures, (2) maintaining the temperature during soaking, and (3) cooling to ambient room temperature. Time is a critical parameter in this process. During the heating and chilling processes, a temperature gradient exists between the interior and exterior of the furnace, which is influenced by the size and geometry of the workpiece.

CHAPTER 2

LITERATURE REVIEW

He et al. [67] examined that friction stir welding (FSW) is an energy-efficient and eco-friendly solid-state joining technique, wherein materials are united through severe plastic deformation instead of melting, thus obviating the necessity for shielding gases and reducing harmful emissions. Due to these benefits, FSW has achieved extensive industry adoption in industries including aerospace, shipbuilding, trains, and electronics. The authors highlighted that Friction Stir Welding (FSW) is essential for combining traditionally un-weldable aluminum alloys, specifically the 2xxx (Al - Cu) and 7xxx (Al - Zn) series, where conventional fusion welding frequently results in significant softening and deterioration of mechanical properties. They emphasized that the integration of disparate materials continues to pose difficulties owing to variations in physical, thermal, and metallurgical characteristics. The integration of interlayers, including zinc, copper, brass, nickel, and tin, proved beneficial in addressing these difficulties. An interlayer improves tensile strength and joint efficiency while mitigating the excessive production of hard and brittle intermetallic compounds by facilitating their fine and uniform distribution. Furthermore, interlayers contribute to the mitigation of residual stresses and enhance metallurgical adhesion at the contact. He also examined the substantial impact of FSW process factors, such as tool rotational speed, traverse speed, and tool material, on material flow, thermal generation, and microstructural development. Their conclusion emphasized that meticulous adjustment of these parameters, together with suitable interlayer selection, is crucial

for attaining defect-free joints with enhanced mechanical performance in both analogous and heterogeneous material combinations.

Maciolek et al. [68] demonstrated that zinc-containing 7xxx series aluminum alloys exhibit remarkable potential for lightweight structural applications due to their high strength and low density; however, their use is constrained by inadequate weldability with conventional fusion welding methods, primarily because of hot cracking. The authors illustrated that friction stir welding (FSW) addresses these restrictions and facilitates the creation of robust connections with enhanced mechanical characteristics. To improve joint performance, they examined the impact of post-weld heat treatment (PWHT) intended to reinstate precipitation hardening following welding. Two post-weld heat treatment (PWHT) methods were utilized, comprising solution treatment at 480 °C with soaking durations of 10 seconds and 300 seconds, succeeded by water quenching and artificial aging at 120 °C for 24 hours. The findings indicated that reduced soaking duration resulted in superior quasi-static strength relative to both extended soaking time and the as-welded FSW condition, suggesting enhanced precipitation kinetics. The fatigue behaviour was analysed under low-cycle and high-cycle situations, demonstrating a decrease in fatigue strength for both post-weld heat treatment scenarios. The deterioration was ascribed to grain growth at the surface caused by the heat treatment. The study demonstrated that the elimination of the compromised surface layer markedly enhanced fatigue performance, underscoring the pivotal influence of surface microstructure on the fatigue behavior of PWHT-FSW joints in 7xxx series aluminum alloys.

Gemme et al. [69] investigated the impact of the welding pitch, defined as the ratio of the tool's advancing to rotational speed, and the heat input during friction stir welding (FSW) of 2.3 mm thick AA7075 T6 sheets on high cycle fatigue (HCF) parameters. Two principal failure modes were identified. Initially, fatigue cracks originated at the base of circular grooves situated in the contact area between the sheets and the tool shoulder. As the welding pitch increased, the adverse effect intensified. Secondly, material softening in the heat-affected zone and sub-surface flaws caused by excessive material agitation were key to failure in instances with low welding pitches. The minimal fatigue strengths were observed in the initial case. At an intermediate welding pitch, the emergence of lateral lips at the peripheries of the weld surface was documented, which considerably diminished the fatigue strength.

Sajadifar et al. [70] investigated the quenching medium employed for post-weld heat treatment following friction stir welding. In the FSW process, the solution heat treated (SHT) AA7075 alloy, subjected to a temperature of 480 °C for 30 minutes, followed by water quenching and artificial aging for 20 hours at 120 °C, exhibited abnormal grain growth (AGG) in the thermo-mechanically affected zone (TMAZ). Air chilling, as opposed to water quenching following solution heat treatment (SHT), effectively lowers grain growth; yet, it concurrently facilitates the formation of precipitate-free zones (PFZ) along grain boundaries, ultimately leading to a substantial reduction in tensile strength and ductility.

Datta et al. [71] examined the formability characteristics of tailor-welded blanks (TWB) fabricated using friction stir welding (FSW) of dissimilar materials, namely with the advancing side being AA6061 and the retreating side AA5754, both of

uniform thickness of 1.5 mm, to assess their formability behavior. The influence of various FSW process parameters, including rotational speeds (950 rpm, 1100 rpm, 1250 rpm, and 1400 rpm) and traverse speeds (50 mm/min, 75 mm/min, and 100 mm/min), determined through visual inspection and macrostructural analysis of the welds, was examined concerning the formability and mechanical properties of welded AA6061 and AA5754 sheets. Tensile tests were conducted on base materials and specimens welded under varying process conditions in accordance with ASTM E8 standard to assess the mechanical qualities. Micro-hardness assessments were conducted at multiple sites over the cross-section in the transverse direction relative to the weld on both sides. The evaluation of formability was conducted by deforming the as-received and welded specimens along uniaxial, plane, and biaxial strain directions utilizing Limit Dome Height (LDH) tests. The tensile test assessment of parameter combinations 1250 rpm–50 mm/min, 1250 rpm–75 mm/min, 1400 rpm–50 mm/min, and 1400 rpm–75 mm/min revealed cracks located away from the weld center towards the advancing side (AA6061 side) of the specimens, signifying high weld quality, consistent with the macrostructures of the stir zone. The micro-hardness distribution graphs indicated a reduction in hardness within the TMAZ of the advancing side, designating it as the most vulnerable area of the weld. The LDH test indicates that the formability of all FSWed specimens is midway between that of AA5754 (better formability) and AA6061 (poor formability), regardless of the strain routes associated with their respective strain hardening exponents. In uniaxial and plane strain conditions of the welded specimens, failure occurred on the advancing side, consistent with the tensile qualities; however, in biaxial stretching, failure transpired in the weld center due to the associated microstructural characteristics. An anomalous behavior

was seen in the equibiaxial stretching; specifically, the minor strain achieved for all welded specimens was markedly lower. Extensive analyses of microstructure and microtexture were conducted on both un-deformed and deformed specimens to examine their distinctive behavior, revealing that initial local misorientations significantly influence the grain orientation spread (GOS) after deformation. The average GOS values were found to be similar across all deformed welded samples within their respective strain trajectories. The inclusion of the Cube texture component in the biaxial strain path substantially reduced the influence of the Goss texture, leading to a distinctive phenomenon: a large reduction in the minor strain observed in the deformed welded materials under the biaxial strain path.

Sen et al. [72] investigated the influence of several process factors, specifically three distinct levels of tool rotating speed, traverse speeds, and tool pin offset distances, on the dissimilar friction stir welding of AA5086 and AA6061 with a thickness of 6 mm. The ANNOVA analysis of the L9 Taguchi orthogonal array indicated that a combination of 1000 rpm rotational speed, 160 mm/min traverse speed, and 0.4 mm tool pin offset resulted in maximum tensile strength.

Schmidt et al. [73] and Singh et al. [74] demonstrated that friction stir welding (FSW) may produce high-quality welds without melting the base materials, thereby circumventing prevalent issues associated with fusion welding, including porosity, cracking, and distortion. Zhang et al. [75] demonstrated that the joints exhibit anisotropic mechanical behavior attributable to the resultant microstructure; however, these distinct local deformation properties can be modified through the meticulous selection of process parameters investigated by Su et al. [76] and Patel et al. [77]

Moreover, Gibson et al. [78] and Patel et al. [77] examined that Friction Stir Welding (FSW) is intrinsically linked to sustainable practices due to its energy efficiency, minimal environmental impact with reduced emissions, material efficiency, and cost-effectiveness, as it eliminates the need for filler materials or shielding gas.

Patsalias et al. [79] investigated the friction stir welding of thin aluminum sheets made from alloys AA1050 and AA5754, aiming to determine ideal process parameters for producing robust junctions with superior mechanical strength. The Taguchi optimization method was utilized to systematically assess the impact of critical FSW parameters, specifically tool rotating speed and welding (traverse) speed, on tensile strength and weld quality. The tensile test findings indicated that a rotational speed of 1000 rpm paired with a welding speed of 250 mm/min produced the maximum joint strength and optimal weld integrity. The study demonstrated that rotating speed significantly influenced weld performance, with excessive speeds resulting in weld degradation due to excessive thermal input. In contrast, reduced welding speeds enhanced weld stability, highlighting the essential need of parameter optimization in achieving defect-free, high-strength FSW joints.

Li et al. [80] examined the mechanical characteristics and degree of softening of friction stir welded (FSW) 6061-T6 aluminum alloy butt joints by experimental investigations and theoretical calculations. A total of 138 monotonic tensile coupon tests and 46 Vickers hardness tests were systematically conducted on welded plates of thicknesses 5, 8, 12, and 16 mm, utilizing varied welding speeds, tool rotation speeds, and tool combinations. The surface morphology post-welding, failure mechanisms, stress-strain curves, and hardness distribution patterns were assessed. An evaluation

of the relevance of current constitutive models and the suggested model for friction stir welded aluminium alloys was conducted, with predictive equations for the essential input parameters being generated. The findings indicate that the reduction in strength and degree of softening caused by Friction Stir Welding (FSW) under optimal parameters surpassed those of 6061-T6 aluminium alloy plates joined via fusion welding, as per Chinese and European standards, demonstrating the efficacy and suitability of FSW technology in aluminium alloy component fabrication and structural connections. The stress-strain curves of FSW butt joints demonstrated an enhanced strain hardening effect coupled with reduced ductility. The advanced three-stage Ramberg-Osgood model, utilizing seven established critical input parameters, demonstrated exceptional accuracy and consistency in predicting full-range stress-strain curves compared to previous constitutive models. Furthermore, the proposed constitutive model, utilizing merely three commonly accessible parameters, can yet attain an excellent equilibrium between precision and practicality.

Li et al. [81] demonstrated that friction stir welding (FSW) can effectively be utilized to fabricate super-large H-shaped aluminum alloy structural members by longitudinally welding pairs of T-shaped sections, thus surmounting the challenges related to the complex extrusion of large cross-section aluminum components. This process markedly contrasts with traditional fabrication techniques, wherein distinct web and flange plates are soldered at their intersections. The authors examined H-shaped sections constructed from 6061-T6 and 6013-T6 aluminum alloys. Six specimens with differing width-to-thickness ratios and plate thicknesses were examined using the sectioning method, yielding almost 4000 residual stress readings. The findings indicated that elevated tensile residual stresses were predominantly

localized in the web weld region, transitioning sharply to compressive stresses adjacent to the weld zone, with a slow, nearly linear decline toward zero at the flange–web junction. Conversely, the distributions of residual stress within the flanges exhibited greater variability and reduced uniformity. The intensity of both tensile and compressive residual stresses demonstrated a minor dependency on geometric parameters, including the width-to-thickness ratio and plate thickness. A simpler multi-linear residual stress distribution model, capable of representing both constant and linearly variable stress regions, is created based on experimental observations. The anticipated outcomes exhibited strong concordance with experimental data, validating the model's trustworthiness for evaluating residual stresses in FSW aluminum alloy H-shaped structural sections.

Salloomi et al. [82] conducted experimental and numerical investigations on the residual stresses of dissimilar friction stir welded 6061-T6 and 2024-T3 aluminum alloy joints. The study revealed that longitudinal residual stress was predominant, exhibiting greater values in 6061-T6 compared to 2024-T3. In summary, existing research on residual stress in FSW aluminum alloys primarily focuses on welded plates, while the longitudinal residual stress and distribution model of FSW H-shaped sections has been inadequately documented.

Guo et al. [83] investigated the stability of the dissimilar welded structure and its residual stress distribution. This work presents the welding of dissimilar aluminum plates, Al 2024 and Al 7075, using Friction Stir Welding (FSW), with the residual stress profiles of the welded specimens evaluated via neutron diffraction. A three-dimensional finite element model was employed to compute and compare the residual

stress distributions resulting from various welding conditions. The microstructural features in various friction stir welded zones were analyzed using the electron backscattered diffraction (EBSD) technique. The longitudinal residual stress on the 7075 side exceeds that on the 2024 side, and the maximum residual stress diminishes from the top scan line to the bottom scan line. The transverse and normal residual stresses are tensile on the 7075 side, whereas those on the 2024 side are compressive. The results of the numerical simulation are consistent with the neutron diffraction data. The KAM map of the thermo-mechanically affected zone indicates greater local plastic deformation compared to the stirred zone, resulting in a longitudinal residual stress with a "double peak" configuration.

Zapata et al. [84] investigated the residual stress in a dissimilar welded structure of 2024 and 6061 alloys, discovering that the maximum residual stress on the advancing side (2024) was less than that on the retreating side (6061). Aval et al. discovered that the peak tensile residual stress of the 6061/7075 friction stir welded joints is situated on the retreating side (7075).

Lombard et al. [86] examine the influence of different welding parameters on the residual stress profiles in friction stir welds of aluminium alloy AA5083-H321, produced on a fully equipped friction welding equipment. Residual stresses were assessed non-destructively by synchrotron X-ray diffraction. The width and maximum of the residual stress profile exhibit a distinct association with heat input, particularly the feed rate, identified as the predominant parameter.

Abdulstaar et al. [87] investigated the influence of microstructural variation on the mechanical properties of friction stir welded joints of 6061-T6 aluminum alloy, which

were later subjected to shot peening (SP). Subsequent to FSW, fatigue specimens were extracted orthogonally to the welding direction. Surface skimming to 0.5 mm from the crown and root sides of the joint was performed, followed by the application of shot peening on both sides utilizing ceramic shots with two distinct Almen intensities of 0.18 mmA and 0.24 mmA. Microstructural analysis via electron backscattered diffraction (EBSD) revealed a disparity in grain refinement inside the weld zone, with the largest grains (5 μm) at the crown side and the smallest grains (2 μm) at the root side. The weld zone exhibited a microhardness reduction of 60 HV in samples subjected to FSW conditions. The use of shot peening resulted in considerable strain hardening on the crown side, with Almen intensities of 0.24 mmA yielding the highest microhardness increase to 120 HV. Conversely, a maximum microhardness of just 75 HV was achieved at the root side. The disparity in strain hardening capacity between the two surfaces was significantly influenced by grain size. The two Almen intensities generated comparable distributions of compressive residual stresses in the subsurface regions, which improved the fatigue strength to that of the base metal for N ≥ 10^5 cycles. The augmentation of fatigue strength became more evident with the escalation of Almen intensity to 0.24 mmA, indicating more improvement through strain hardening.

Mishra et al. [88] examined the development of Friction Stir Welding (FSW) and Friction Stir Processing (FSP). Significant attention has been directed towards: (a) the mechanisms behind weld production and microstructural refinement, and (b) the influence of FSW/FSP parameters on the resulting microstructure and ultimate mechanical characteristics. Although the majority of the information pertains to aluminum alloys, significant findings are now accessible for other metals and alloys.

Currently, the proliferation of technology has markedly surpassed the fundamental comprehension of microstructural evolution and the links between microstructure and properties.

Stewart et al. [89] introduced two models for the Friction Stir Welding (FSW) process: the mixed zone model and the single slip surface model. The mixed zone concept posits that the metal within the plastic zone circulates in a vortex system at the angular velocity of the tool at the tool-metal contact, with the angular velocity diminishing to zero near the periphery of the plastic zone. In the single slip surface concept, the primary rotational slip occurs at a contracted slip surface external to the tool–workpiece interface. The use of a restricted slip region yielded predictions of the thermal field, force, and weld region morphology that aligned with experimental measurements.

Arbegast et al. [90] posited that the microstructure and material flow in friction stir welding closely parallel those found in traditional hot-working methods, including extrusion and forging. The FSW process was characterized as a metalworking operation comprising five separate zones: preheating, initial deformation, extrusion, forging, and post-heating/cooling. In the preheat zone, temperature increases owing to frictional and adiabatic heating, influenced by material characteristics and tool traverse velocity. Upon reaching a crucial temperature and flow stress, the material enters the initial deformation zone, initiating plastic flow and directing the material into the shoulder and extrusion zones. In the extrusion zone, material circulates around the pin from the advancing front to the rear within a thermally and mechanically delineated width. Subsequently, the forging zone is where the material is solidified under

hydrostatic pressure, aided by the tool shoulder. The material subsequently cools in the post-weld region. Arbegast also formulated a mass-balance-based model for the extrusion zone, showing strong concordance between anticipated temperature, strain rate, extrusion pressure, and experimental data.

Sato et al. [91] examined the transverse tensile characteristics of the friction stir weld of 6063-T5 aluminum. To elucidate the impact of postweld treatment on weld characteristics, postweld aging (175 °C for 12 hours) and postweld solution heat treatment and aging (SHTA, 530 °C for 1 hour followed by 175 °C for 12 hours) were performed on the welds.The experiment demonstrates that the tensile strength and elongation are minimal in the as-welded joint. The aged weld exhibits somewhat superior strength compared to the base material, along with enhanced ductility. The SHTA enhances the weld's strength above that of the base material while nearly fully restoring ductility.

Rhodes et al. [92] conducted an experiment on the microstructural evolution of 7075Al-T651 during friction stir welding, revealing the dissolution of larger precipitates and subsequent reprecipitation at the weld center. Consequently, they determined that the maximum processing temperatures range from approximately 400 to 480 °C in FSW 7075Al-T651. Murr et al. noted that certain precipitates remained undissolved during welding and proposed that the temperature increases to around 400 °C in friction stir welding of 6061 aluminum.

Xu et al. [93] created two finite element models, the sliding interface model and the frictional contact model, to simulate the friction stir welding process. The simulation predictions of the material flow pattern derived from these finite element models

qualitatively align with the empirically measured pattern obtained through the marker insert approach.

Mishra et al. [94] simulated the metal flow surrounding profiled Friction Stir Welding (FSW) tools with a two-dimensional Computational Fluid Dynamics (CFD) software, Fluent. A 'slip' model was created, in which the interface conditions were determined by the local shear stresses. The two-dimensional modeling yielded the following significant discoveries. The flow behavior derived from the slip model markedly differs from that predicted by the conventional assumption of material adhesion. The slip model demonstrated notable variations in flow with diverse tool geometries, which are not apparent with the traditional stick model. The deformation region for the slip model is significantly smaller on the advancing side compared to the retreating side. The material in the pin's trajectory is displaced around the receding side of the tool.

Kumar and Sharma [95] studied the influence of FSW process parameters on the Friction stir welded (FSW) regions such as weld nugget zone (WNZ), thermomechanical affected zone (TMAZ), and heat-affected zone (HAZ). They found that R of 1600 rpm, T of 30 mm /min, S of 14 mm, and P of 4 mm exhibits maximum tensile strength, yield strength, microhardness as compared to other samples due to plastic flow and generation of optimal frictional heat of material at stir zone. At R of 2240 rpm, T of 20 mm/min, S of 16 mm, and P of 5 mm exhibit a maximum elongation and dome height FSW blank.

Praneetha et al. [96] studied mechanical properties of the welded joint made by FSW of AA6082 and AA 2014. To get a good weld it is found that softer alloy AA2014 should be placed on the advancing side. The advancing side is the direction in which

the tool rotates and material goes into the plastic state at this region first and then it will be settled on the retreating side. Researchers found that the weld joint formed using the 900 r.p.m. 40 feed rate, 10 angles of the tool have a good surface finish compared with the other welded joint operating parameters.

Kamalvand et al. [97] studied the effect of friction stir welding parameters on the deep drawing of tailor-welded blanks (TWBs). The results revealed that the joint made with circular pin obtain gives the best results in deep drawing in terms of thickness distribution and weld line movement.

Parente et al. [98] carried out a series of experiments to investigate the formability performance of TWBs produced by FSW with dissimilar aluminum alloy thin sheets, and the results showed that TWB formability depended on weld line orientation.

Steuwer et al. [99] studied the residual stress distribution in dissimilar friction stir welds using neutron and synchrotron X-ray diffraction as a function of tool rotation and traverse speed. In all of the welds measured the region around the weld line was characterized by significant tensile residual stress fields which were balanced by compressive stresses in the parent material. The largest stresses occurred in the longitudinal direction being typically two to three times the stresses in the transverse direction. In most cases, the peak tensile residual stresses were found at the edge of the tool shoulder approaching the local room temperature yield stress.

Yoshida et al. [100] demonstrated that for a given aluminium alloy, high strength friction stir welds are obtained when the welding speed falls within a processing window. When the welding speed is too high, surface and sub-surface defects form,

lowering the notch tensile strength in the weld zone. At low welding speed, the notch tensile strength is negatively affected by the formation of a softened zone.

Mahoney et al. [101] studied the mechanical properties of FSW aluminium alloys and compared with the mechanical properties of the parent material, which helps in finding the way of changing the behaviour of the parent material after friction stir welding.

Vilaca and Thomas [102] studied the application of FSW technologies for ship building, design and construction and indicated that it is capable of reducing construction costs and welding distortion and improving durability in comparison with fusion welding.

Peel et al. [103] investigated the mechanical properties and residual stresses of a FSW aluminium 5083 test specimen, and concluded that these properties are governed by the thermal input rather than by the mechanical deformation caused by the FSW tool.

Steuwer et al. [104] studied the effect of tool traverse and rotation speeds on the residual stresses are quantified for welds between non-age-hardening AA5083 and age- hardening AA6082 and compared to single alloy joints made from each of the two constituents. The residual stresses have been characterized non-destructively by neutron diffraction and synchrotron X-ray diffraction. The region around the weld line was characterized by significant tensile residual stress fields which are balanced by compressive stresses in the parent material. The rotation speed of the tool has been found to have a substantially greater influence than the transverse speed on the properties and residual stresses in the welds, particularly on the AA5083 side where the location of the peak stress moves from the stir zone to beyond the edge of the tool shoulder.

Cavaliere et al. [105] studied the effect of processing parameters on mechanical and microstructural properties of AA6082 joints produced by friction stir welding. Different welded specimens were produced by employing a fixed rotating speed of 1600rpm and by varying welding speeds from 40 to 460mm/min. The joints mechanical properties were evaluated by means of tensile tests at room temperature. In addition, fatigue tests were performed by using a resonant electro-mechanical testing machine under constant amplitude control up to 250Hz sinusoidal loading.

Miles et al. [106] investigated Friction stir welding (FSW) as a method for joining dissimilar-aluminium alloys 5182-O, 5754-O, and 6022-T4. These alloys are used in automotive applications in which parts consisting of dissimilar welded combinations of these alloys may be of interest. This study focuses on the formability of friction-stir-welded, dissimilar-alloy pairs of essentially the same gage, in order to investigate the mechanical properties that can be obtained using this approach.

Feng et al. [107] studied neutron diffraction study of residual stresses in 6061-T6 aluminium friction stir welds. The specimens were 6 mm thick plates friction stir welded in the butt joint configuration at two welding speeds, 279 and 787 mm/min, respectively. The experimentally determined residual stresses show a symmetric double-peak profile across the weld center line, with the peaks located in the middle of the heat-affected zone. The maximum tensile stress, which is in the longitudinal direction, is 130 and 200 MPa, respectively. It is shown that the difference in the residual stress is due to a change in the microstructure and stress relaxation that occurred as a result of the longer heating time associated with the low welding speed.

Han et al. [108] studied the mechanical characteristics for friction stir welding (FSW) of 5083-O Al alloy were evaluated. The results show that in FSW at 800 r/min and 124 mm/min, a weld defect is observed at the start point. However, the button shape at the end point is good and the stir zone has a soft appearance. At 267 mm/min, a void occurs at the button. A slight weld defect and rough stir zone are seen both at the start and end points at 342 mm/min. Moreover, at the bottom, a tunnel-type void is observed from an early stage to the end point, and at 1 800 r/min, a weld defect can be found from an early stage to the end point.

Simoncini et al. [109] studied the effect of FSW parameters, tool configuration and sheet positioning on the mechanical properties, microstructure and post-welding formability to evaluate the advantages offered by the new welding methodology, the experimental results obtained using the double-side friction stir welding were compared with those given by the conventional process. The conventional FSW joints show ultimate tensile strength and elongation higher than those exhibited by the DS-FSW joints.

Kumar and Reddy [110] studied the formability of AA6082 alloy to manufacture parabola cups using single point incremental forming (SPIF) process. The finite element analysis has been carried out to model the single point incremental forming process using ABAQUS software code.

Liu et al. [111] studied an advanced forming technology, solution Heat treatment, Forming and in-die Quenching (HFQ), has been employed to form AA6082 tailor welded blanks (TWBs). In comparison with conventional stamping of TWBs, the mechanical properties and formability of AA6082 laser TWBs could be improved

under the HFQ forming condition. The TWB was divided into three physical zones, i.e. base metal, heat affected zone (HAZ) and weld zone, based on the hardness distribution. It was found that the degraded hardness of the weldment can be restored after HFQ forming. TWBs of AA6082 with different thickness ratios of 2 (2–1 mm), 1.3 (2–1.5 mm) and 1 (1.5–1.5 mm) were used to study the TWB thickness ratio effects on the forming behaviour. Hemispherical punch dome tests on the TWBs with varying thickness ratios demonstrated different foamabilities, and indicated increased displacement of the weld line with increasing thickness ratio. Finite element (FE) modelling was adopted to analyze the weld line movement and strain distributions during HFQ.

Dwivedi [112] studied A356/C355Aluminum Alloy found that the parameters which affect the tensile strength in descending order are as follows: tool rotational speed, axial force and welding speed. Shaikh et al. [113] studied the effect of Rotational speed and welding speed on weld quality and found that the tensile strength of the welded specimens was about 45MPa which is almost 80 % that of the base plate, the FSW process can be employed to weld HDPE plates with 4% filler minerals. Increasing the work linear speed from 14 to 56 mm/min had a decreasing effect on tensile strength.

Raju et al. [114] concluded that weldment made by FSW at the tool rotation speed of 900rpm and weld speed 40mm/min exhibited better mech properties. This is due to sufficient heat generation and proper mixing of material in the weld zone.

Prasad et al. [115] studied effect of Axial force, tool speed, Welding speed and found that As the Tool Rotational Speed increases, effectively Hardness also increases, and

in the same manner Axial Force also effects, if Welding Speed increases, effectively Hardness will be increases up to 60mm/min and slightly decreases at 72 mm/min.

Meshram et al. [116] found that A defect free weld with parameters of 1100rpm and traverse speed 8mm/min showed tensile strength of base material with 37% elongation by taking Welding speed, Rotational speed and Tilt angle as the variables. Ahmadi et al. [117] concluded that the welding speed was the most significant welding process parameter whereas the tilt angle was the least significant one affecting the tensile-shear strength.

Elatharasan and Kumar [118] found that Ultimate tensile strength of FSW joints increases with increase in tool rotational speed and welding speed up to a max value and then decreases. The materials used by the authors are AA6061-T6 and AA7056-T6 and the variables are Welding speed, Rotational speed, and Axial force.

Ko et. al. [119] found the new forming method is hot forming quenching (HFQ) for improved the aluminium alloys formability of friction stir welded tailor welded blank (TWBs). In this process at elevated temperature solid solution heat treated aluminium sheets formed. Joining of two different sheets thickness as TWBs by FSW tool shape and plate inclined angle is 3.44 degree. For the solid solution heat treatment conditions, the TWBs specimens was heated up to 950°C for 2 hours and transfer for rapidly quenched at 100°C and 200°C respectively.

Hui et al. [120] studied the formability of aluminium alloy AA7075 was investigated at elevated temperature through limiting drawing ratio (LDR), tensile test and limiting dome height (LDH) test. In uniaxial tensile test the properties of AA7075 does not get effected at the temperature of 140 ℃ and above this temperature ultimate and yield

tensile strength decrease and elongation not always up to 260 ℃, it begins to decrease after that temperature. The strain rate sensitivity index factor increased above the 140 ℃. At 140 ℃ deep drawing and stretch formability are poor. The best deep drawing formability at 180 ℃ and stretch formability at 220 ℃.

Steuwer et al. (2006) [121] investigated the residual stress distribution in dissimilar friction stir welds employing neutron and synchrotron X-ray diffraction techniques, examining the effects of tool rotation and transverse speed. In all measured welds, the area surrounding the weld line was characterized by substantial tensile residual stress fields, which were counterbalanced by compressive stresses within the source material. The maximum stresses were observed in the longitudinal direction, generally two to three times greater than those in the transverse plane. In the majority of instances, the maximum tensile residual stresses were observed at the margin of the tool shoulder, nearing the local room temperature yield stress. The exception occurs at a modest rotation speed (280 rpm) on the AA5083 side of the weld, where the stress reaches its maximum at the weld line. For the age-hardenable alloy AA6082, a direct correlation was observed between the position and magnitude of the maximal tensile stress and the welding parameters. It should be noted that the comparatively small dimensions of the welded plates allowed for an analysis of the residual stress state without the need to dissect the welds. Consequently, tension alleviation will not have been achieved. This may partly account for the comparatively high stresses measured in the present case compared to studies on sectioned samples [8], and aligns more closely with data obtained from larger weld sections [32].

Z. Feng et al. (2000) [33] investigated residual stresses in aluminum friction stir welds. The specimens consisted of 6 mm thick plates joined by friction stir welding in a butt joint configuration at two welding velocities, 279 and 787 mm/min, respectively. The residual stresses determined through experimental methods exhibit a symmetric double-peak distribution across the weld centerline, with the peaks situated within the central region of the heat-affected zone. The maximal tensile stresses in the longitudinal direction are 130 MPa and 200 MPa, respectively. It is demonstrated that the variation in residual stress results from alterations in the microstructure and stress relaxation, which occur due to the extended heating duration associated with lower welding speeds.

Hashimoto et al. [124] established that, for a specific aluminum alloy, high-strength friction stir welds are achieved when the welding speed is maintained within an optimal processing window. Excessively high welding speeds induce surface and subsurface defects, thereby reducing the notch tensile strength within the weld zone. At reduced welding speeds, the notch tensile strength is adversely impacted by the development of a softened zone.

Svensson et al. (1999) [125] investigated that for Al-6082 friction stir welds, which exhibit a hardness profile similar to that of Al-6061-T6, fracture takes place in the weakest region outside the weld zone. Conversely, for 5083 aluminium alloys, whose hardness shows minimal variation throughout the weld, fractures were predominantly observed within the weld zone.

North et al. (1999) [126] determined that the notch tensile strength indeed correlates with the width of the softened zone, and when a minimal softened zone is created, the notch tensile strength of the joint approaches that of the base metal.

Fatigue experiments conducted by Bussu and Irving [126] demonstrated that the area of lowest hardness corresponds to the region where the majority of fatigue cracks originated. Therefore, from a microstructural perspective, increased welding speed yields friction stir welds with enhanced mechanical properties, provided that no defects are introduced.

Paik et al. (2008) [127] investigated the application of high-strength aluminium alloys within the shipbuilding industry. They discovered that the advantages of utilizing aluminum instead of steel include its reduced weight, which enhances cargo capacity and decreases energy consumption, as well as its excellent corrosion resistance and low maintenance requirements.

Mahoney et al. (1998) [128] investigated the mechanical properties of FSW aluminium alloys and contrasted them with those of the parent material, thereby aiding in understanding how the behavior of the parent material is altered following friction stir welding.

Peel et al. (2003) [129] examined the mechanical properties and residual stresses of an FSW aluminium 5083 test specimen, concluding that these properties are primarily influenced by the thermal input rather than the mechanical deformation induced by the FSW tool.

This study by P. Cavaliere et al. (2007) analyzed the influence of processing parameters on the mechanical and microstructural properties of AA6082 joints fabricated through friction stir welding. [130] Different welded specimens were fabricated by maintaining a constant rotational speed of 1600 rpm while varying the welding velocities from 40 to 460 mm/min. The mechanical properties of the joints were assessed through tensile experiments conducted at ambient temperature. Furthermore, fatigue tests were conducted utilizing a resonant electro-mechanical testing apparatus under constant amplitude control, with sinusoidal loading up to 250Hz. The fatigue experiments were performed in axial control mode across all welding and rotation speeds employed in the current study. The microstructural evolution of the material was examined in relation to the welding parameters through optical analysis of the joint cross-sections. Additionally, SEM observations of the fractured surfaces were conducted to characterize the weld performance.

M.P. Miles et al. (2005) [131] examined Friction Stir Welding (FSW) as a technique for joining dissimilar aluminum alloys 5182-O, 5754-O, and 6022-T4. These alloys are employed in automotive applications where components composed of dissimilar welded combinations of these alloys may be of relevance. This research examines the formability of friction-stir-welded, dissimilar alloy pairings of approximately equal thickness to evaluate the mechanical properties achievable through this method. Testing demonstrated that the properties of welded 5182/5754 alloy pairs maintained relatively excellent formability in comparison to the performance of the base material. However, the alloy pairs 5182/6022 and 5754/6022 exhibited markedly diminished

49 formability relative to the properties of the base material, with defects observed in the heat-affected zone (HAZ) of the 6022 or within the weld nugget itself. However, this degree of formability was comparable to that of monolithic 6022 welded by friction stir welding.

X.L. Wang et al. (2000) [132] conducted a neutron diffraction analysis of residual stresses in 6061-T6 aluminum friction stir welds. The specimens consisted of 6 mm thick plates joined by friction stir welding in a butt joint configuration at two welding velocities, 279 and 787 mm/min, respectively. The residual stresses determined through experimental methods exhibit a symmetric double-peak profile across the weld center line, with the peaks positioned within the middle of the heat-affected zone. The maximal tensile stresses in the longitudinal direction are 130 MPa and 200 MPa, respectively. It is demonstrated that the variation in residual stress results from alterations in the microstructure and stress relaxation, which occur due to the extended heating duration associated with lower welding speeds.

Min-Su Han et al. (2009) [133] investigated the mechanical properties of friction stir welding (FSW) applied to 5083-O aluminum alloy. The results indicate that, in FSW conducted at 800 r/min and 124 mm/min, a weld defect is identified at the initiation site. However, the contour of the button at the endpoint is appropriate, and the stir zone exhibits a smooth appearance. At a rate of 267 mm/min, a void forms at the button. A minor weld defect and an uneven stir zone are observed at both the initial and terminal locations at a speed of 342 mm/min. Furthermore, a tunnel-like void is observed from an early stage to the endpoint at the bottom, and at 1,800 r/min, a weld defect can be detected throughout the entire length from the initial to the final stage. These defects

are characterized by uneven surfaces and imperfect joints resulting from excessive rotational speed and high applied force. Weld fractures in relation to rotational and travel velocities are observed within the stir zone. The optimal FSW parameters are a welding speed of 124 mm/min and a rotational speed of 800 rpm.

Jun Liu et al. (2009) [136] conducted investigations and comparisons during high-temperature tensile experiments to examine their formability. The outcomes of tensile tests and microstructural analyses were presented, demonstrating the deformation characteristics under various conditions. Both alloys demonstrated comparatively limited strain hardening effects, particularly at reduced strain rates. Furthermore, the maximum strain rate sensitivity index (m value) was identified, and the peak percent elongation-to-failure also aligned with the ranges of highest m value. The flow stress, in conjunction with dynamic particle growth, was correlated with temperature and strain rate. The granules appeared to be coarser in the deformed specimens.

P.F. Bariani et al. (2013) [135] examine the viability of manufacturing sheet components through stamping AA5083 sheets at elevated temperature and strain rate. Laboratory tensile and Nakajima-type tests were conducted to assess the material's flow stress, ductility, and fracture limits, as well as their sensitivity to temperature and strain rate. This was aimed at identifying the optimal combination of process parameters to ensure both maximum formability and effective post-deformation mechanical properties. Industrial testing was carried out on an automotive component to verify the laboratory findings.

J. Liu et al. (2010) [136] investigated the non-superplastic grade of 5083 aluminum alloy (AA5083) sheets with a thickness of 3 mm, which were utilized in a superplastic-

like forming process that integrates drawing (mechanical pre-forming) and superplastic forming (blast forming). Experimental trials were carried out to assess the potential for enhancing the forming rate and reducing the process temperature. The void was initially pre-formed during the mechanical pre-forming stage. Consequently, a portion of the material near the flange region was pre-emptively introduced into the deformation cavity prior to the blast forming process. Secondly, argon gas was introduced to the sheet, causing it to deform and contact the interior die surface at the conclusion of the pressure cycle. The blow forming phase lasted merely 8 minutes, and the procedure resulted in an almost fully formed component at 400°C. The minimal thickness was observed at the inward corners, while the maximum reduction in thickness of the formed component was 54%. Microstructural observations revealed the occurrence of grain growth and cavitation.

D.E. Cipoletti et al. (2008) [137] examined the effect of heterogeneity in grain boundary sliding resistance on the constitutive behavior of AA5083 during high-temperature deformation, employing simulations that assumed a uniform resistance to sliding across all grain boundaries. Molecular dynamics simulations demonstrate that sliding resistance is highly dependent on the nature of the boundary: high-angle boundaries exhibit resistance levels up to an order of magnitude lower than those of low-angle boundaries. To examine the impact of this heterogeneity, finite element simulations are employed to assess how the proportion of freely sliding boundaries within a polycrystal affects its creep behavior and the underlying deformation mechanisms. Our calculations indicate that (i) the critical strain rate at which the

deformation mechanism shifts from GBS to DC ranges from 2×10^{-5} s^{-1} to 10^{-3} s^{-1} as the volume fraction f increases from 20% to 100%. (ii) The stress exponent in the GBS regime diminishes from approximately 3.25 to 1.5 as the parameter f increases from 0% to 100%. The stress exponent within the DC regime exhibits reduced sensitivity. (iii) The flow stress at a strain rate of 10^{-4} s^{-1} (GBS regime) rises from 6 MPa to 14 MPa as f decreases from 100% to 0%; conversely, the flow stress at a strain rate of 0.01 s^{-1} increases from 33 MPa to 42 MPa (DC regime). (iv) A rapid escalation in GBS and an associated decline in flow stress are observed as f increases from 67% to 77%, indicating the existence of a percolation threshold. (v) A secondary (albeit lesser) increase in grain boundary sliding takes place when f is elevated from 39% to 46%. Microstructures with f=39% seem to include at least one particle entirely enclosed by sliding-resistant boundaries; in contrast, microstructures with f=46% do not exhibit this feature. We hypothesize that the obstructed granules could function as reinforcing agents. (vi) The flow stress and deformation mechanism are governed by the proportion of freely sliding grains and are not influenced by the specific spatial distribution of sliding resistance within the polycrystal.

L. Leotoing et al. (2008) [138] investigated the effect of strain rate on the formability of AA5083 by characterizing the material behavior of aluminum alloy 5083 at elevated temperatures. To characterize its visco-plastic behavior, Swift's hardening law is employed, and the corresponding parameter values are determined. Subsequently, two distinct methodologies are presented for constructing the forming limit diagrams (FLDs) of this alloy sheet and for assessing the influence of the rate sensitivity index

on its formability. The initial approach is theoretical (the M-K model), and an algorithm has been devised to determine the limiting strains according to this model. In the second approach, the Marciniak test is modeled using the commercially available finite-element software ABAQUS. Based on FEM results, various failure criteria are examined, and a suitable one is selected to identify the initiation of localized necking. With the material behavior data for AA5083 at 150 °C, parametric analyses are conducted to assess the influence of the strain rate sensitivity index. The comparison of results from these two approaches reveals a consistent trend: an enhancement of formability correlating with increased strain rate sensitivity. Finally, by examining the compensating effects of the strain hardening and rate sensitivity indices, the forming limit diagrams of this sheet at 150, 240, and 300 °C are established and compared. Results indicate that the formability of AA5083 does not appear to progress beyond a certain temperature (between 240 and 300 °C); however, above this temperature, the formability is significantly enhanced.

.M. Simoncini et al. (2014) [139] investigated the influence of FSW parameters, tool configuration, and sheet positioning on the mechanical properties, microstructure, and post-weld formability to assess the benefits provided by the new welding technique. The experimental results obtained through double-sided friction stir welding were compared with those from the conventional process. The conventional FSW joints demonstrate ultimate tensile strength and elongation superior to those observed in the DS-FSW joints.

K. S. S. Kumar et al. (2016) [140] investigated the formability of AA6082 alloy for the fabrication of parabola cups through the single point incremental forming (SPIF) procedure. The finite element analysis has been conducted to model the single-point incremental forming process utilizing ABAQUS software.

Xi Luan et al. (2016) [142] Formulation of forming limit diagrams (FLDs) for AA6082 under warm and heated stamping conditions. The experiments were conducted across a range of temperatures from 300°C to 450°C and forming speeds varying from 75 mm/s to 400 mm/s. The strain was analyzed and quantified utilizing ARGUS software supplied by GOM. The results clearly indicate that the formability of AA6082-T6 sheet metal, as measured by the limit major strain, increased by 38.9% when the forming temperature was raised from 300°C to 450°C at a speed of 250 mm/s. Additionally, the formability improved by 42.4% when the forming speed was reduced from 400 mm/s to 75 mm/s at a temperature of 400°C. It has been confirmed that heat stamping is a promising technology for the production of complex-shaped components. In this study, a novel test apparatus was designed and fabricated, and the formability limits of the high-strength aluminum alloy AA6082 in the T6 condition were experimentally established through formability testing. The influence of forming temperature and forming speed on formability was comprehensively examined, representing warm/hot stamping operations. The FLDs were acquired under various conditions.

J. Liu et al. (2015) [143] investigated an advanced forming technique, Solution Heat Treatment, Forming, and In-die Quenching (HFQ®), which has been utilized to shape

AA6082 tailor-welded blanks (TWBs). Compared to traditional stamping of TWBs, the mechanical properties and formability of AA6082 laser TWBs can be enhanced under HFQ forming conditions. The TWB was segmented into three distinct physical regions—namely, the base metal, the heat-affected zone (HAZ), and the weld zone—based on the distribution of hardness. It has been determined that the reduced hardness of the weldment can be reestablished following HFQ forming. TWBs of AA6082 with varying thickness ratios of 2 (2–1 mm), 1.3 (2–1.5 mm), and 1 (1.5–1.5 mm) were employed to investigate the influence of TWB thickness ratios on forming behavior. Hemispherical punch dome experiments on the TWBs with varying thickness ratios revealed differing formabilities and showed increased displacement of the weld line as the thickness ratio increased. Finite element (FE) modeling was utilized to examine the displacement of the weld line and the distribution of strains during HFQ.

S. Mohamed et al. (2012) [144] investigated a series of coupled viscoplastic constitutive equations pertaining to deformation and damage during hot stamping and cold die quenching of AA6082 panel components. The set of equations can be employed to forecast viscoplastic flow and damage caused by plastic deformation of AA6082 during heated forming processes. Deformation and damage are governed by a coupled set of evolving internal state variables, such as dislocation density, which are influenced by thermally activated and deformation-dependent processes including recrystallization and recovery. A phenomenological characterization of damage is formulated based on the anticipated physical scaling with respect to temperature, strain, and strain rate. The resulting equations were incorporated into the commercial software ABAQUS. A strong correlation has been established between the process simulation and the experimental results. This verifies that the physical dependencies

within the constitutive equations are accurately formulated, and that the equations and finite element model are suitable for calibration and application in the hot stamping of AA6082 panel components. Furthermore, process optimization was conducted utilizing the model to determine the optimal forming parameters for a basic panel component featuring a central circular opening. The study concludes with an analysis of the potential influence of the constitutive model, experimental characterization, and modeling outcomes on the manufacturing of AA6082 panel components.

Akramifard et al. examined the mechanical characteristics of cold roll bonded AA1050/AISI304 clad sheet. To assess the mechanical properties of the Al/ stainless steel clad sheet, tension experiments were conducted at room temperature. The results indicated a considerable decrease in flow stress following the peak point of the stress–strain curves (UTS), which corresponds to the debonding of the interface. The UTS values were considerably lower than the tensile strength of the base material, 304L stainless steel (722 MPa), but were found to be substantially higher than those of the annealed aluminum (72 MPa). The decline following the peak of the stress–strain curves indicated the influence of bond strength on tensile behavior and suggested the failure of localized bonds [50]. The tensile properties can also be ascertained through the application of the rule of mixtures. The flow stress of the (SS304/Al/SS304) sandwich sheet is observed to be intermediate between the stress values of the individual layers, consistent with the rule of mixtures [147].

Masoumi and Emadoddin conducted research on the formability and bond strength of two- and three-layer Al/SiCP sheets produced via the roll bonding process, examining various thickness reductions and layer configurations through Erichsen cupping tests and lap-shear tests [147].

Yoshida and Hino et al. [148] examined the formability of two- and three-ply steel-aluminium clad sheets. It was noted that, in both the analytical predictions and the experimental observations, the FLDs of the laminates fall within the range defined by their constituent sheet metals. The influence of pre-strain induced during the roll-bonding process on formability was also examined [54].

Lee and Kim examined the utilization of the rule of mixtures to forecast the flow stress in stainless steel-aluminium-stainless steel sandwich sheets. The rule of mixtures, which averages component qualities according to volume fractions, may be applied to the tensile strengths and strength coefficients of the sandwich specimens. The yield strengths of the sandwich sheets exhibited a positive divergence from the rule of mixtures owing to significant disparities in the elastic moduli of the components. The rule was determined to be applicable to uniform elongations, strain hardening exponents, and strain rate sensitivities of the sandwich sheets [52].

Basril et al. [149] examined the influence of heating temperature on the formability of various metal sheets, including mild steel, stainless steel, and aluminum, during the deep drawing process of a square cup. The thickness distribution in the deep-drawn square cup was analyzed at three distinct temperatures and various tooling positions through both numerical and experimental methodologies. It was observed that the uniform thickness distribution in the square cup was attained through the application of die heating, which maintained a temperature of 150°C.

Additionally, the impact of heating temperature on the drawability of Aluminum and Mild Steel round cups was examined through both numerical and experimental methods. The most notable elongation of 11.64 mm was observed for the aluminum round cup at a limiting drawing ratio (LDR) of 1.69 and a temperature of 100°C, while

a substantial elongation of 12.44 mm was recorded for mild steel at an LDR of 1.56 and the same temperature. The improved formability, achieved through the elimination of defects such as wrinkling and fracture, was attainable at an elevated temperature for both types of metal sheets.

Jayahari et al. [150] examined the formability of Austenitic stainless steel and assessed the friction behavior during tepid deep drawing of aluminum alloy through numerical and experimental methods. The elevated LDR of 2.5 was observed at a temperature of 150°C and persisted up to a temperature of 300°C. In the case of IS 737 grade aluminum alloy, the formability was observed to improve at a temperature of 350°C. Elevated friction levels were observed at higher temperatures for Aluminum, which were mitigated through the application of high-temperature lubricant Molycote [59].

.

Ghosh et al. [151] conducted tepid deep drawing experiments to examine the forming behavior of two Al-Mg-Si alloys. Among the chosen parameters, temperature was identified as having a considerable impact on the force-displacement curve, while anisotropy was found to substantially influence the earing profile. The count of ears observed remains unchanged, although the amplitude diminished with an increase in temperature. The anisotropy was found to remain constant despite variations in temperature. The thickness was observed to increase from the bottom towards the flange region and was found to be lower at the mid-height of the wall [60].

Alinia et al. [152] examined the optimization of process parameters for the tepid deep drawing of ASS304 steel, utilizing a temperature gradient. The influence of process parameters on the LDR, forming force, and thickness was examined at a temperature of 300°C. The optimal punch corner radius, matrix cavity corner radius, Blank Holder

Force (BHF), and temperature were determined to be 7.5 mm, 5 mm, 2200 N, and 160°C, respectively. The temperature and matrix cavity radius were identified as having the most substantial influence on LDR.

Goud et al. [153] examined the formability of EDD Steel under elevated temperature conditions. The stretch forming process was performed utilizing heated forming tooling equipped with Ni-based superalloy dies to generate the Forming Limit Diagram (FLD) at both room temperature and elevated temperature. It was observed that the formability improved with rising temperature owing to the reduction in mean flow stresses, except at a temperature of 450°C. The limited formability was observed at a temperature of 450°C, attributable to the dynamic strain regime [62].

Basak et al. [154] performed experimental and numerical studies to forecast the formability and fracture behavior of as-received and pre-strained sheet materials during the deep drawing process. Various types and magnitudes of pre-strain, including 5% and 10% equi-biaxial pre-strains (5% EBP and 10% EBP), 10% plane strain pre-strain (10% PSP), and 10% uniaxial pre-strain (10% UP), were applied to the 1.2 mm thick sheets of extra deep drawing (EDD) steel and aluminum alloy (AA5052). Additionally, all pre-strained sheet samples were subjected to deformation utilizing a cylindrical deep drawing apparatus. The forming limit diagrams (FLDs) of the as-received sheets were predicted using the Marciniak–Kuczynski (MK) model, which incorporated various anisotropic yield functions, including the Hill48 model [63].

Singh et al. [155] examined the formability of 1.0 mm thick commercially pure titanium (CPTi) sheet metal employing a laboratory-scale deep drawing test setup, and determined the limiting drawing ratio (LDR) to be 2.143. Four ears were observed in

the LDR cup with the maximal cup height along the diagonal direction (DD) and troughs along both the rolling direction (RD) and transverse direction (TD), and the earing height was approximately 13.7% of the total cup height. Tensile and stacking compression tests were conducted along various orientations to assess the anisotropic properties and the tension-compression strength differential, and these data were utilized to construct the CPB06 constitutive yield model.

Lin et al. [156] examined the influence of plastic anisotropy in ZK60 magnesium alloy sheets on their formation behavior during the deep drawing process. The deformation behavior of the sheet during deep drawing was investigated through both experimental methods and finite element analysis. The ZK60 alloy sheet demonstrates a higher plastic strain ratio (r) at 45° compared to 0° and 90° to the rolling direction, and the r value diminishes as the temperature increases across various loading orientations. A negative planar anisotropy (Δr) value leads to earing at a 45° angle relative to the rolling direction. As the drawing ratio (DR) increases, the average earing ratio initially rises to a zenith before subsequently decreasing, forming a bell-shaped curve. The average earning ratio of the cylindrical drawn cup increases as the deep drawing process advances. At the shoulder region of the drawn cups, the greatest reduction in thickness strain occurs at 45° to the rolling direction of the sheet. In the necking region, the minimal thickness strain at 0° is lower than that observed at 45° and 90° orientations.

Atrian et al. [157] examined the effects of various factors, including the layering sequence of the layers, lubrication, blank-holder force, and the diameter of the composite blank, on the load–displacement curve and the ultimate shape of the manufactured components. This study focuses on the experimental and finite element

analysis of the deep drawing process involving steel and brass laminated sheets. The reasonable accord between the experimental and finite element results demonstrated that FEM can be effectively employed in parameter studies of various industrial processes. In the aforementioned study, the drawing force necessary was overstated by approximately 10% in the finite element simulations.

Aghchai et al. examined the formability of a two-layer laminated sheet composed of Al1100 and St12. Theoretical and experimental methods have been employed to determine the forming limit diagram of the two-layer Al1100-St12 sheet, and the results obtained are subsequently compared. Additionally, the forming limit diagram of the two-layer sheet is contrasted with the formability of its metallic constituents. Results demonstrated a strong concordance between theoretical and experimental findings. It is also demonstrated that the formability of the two-layer metallic sheet exceeds that of its individual, lower-formability component [81].

Bagherzadeh et al. formulated an analytical model to examine the stress distribution and instability conditions in hydro-mechanical deep drawing (HMDD) of cylindrical aluminum and carbon steel containers. Based on these models, several parametric studies were conducted to investigate the effects of layer thickness, layer configuration, drawing ratio, and frictional conditions on the main parameter of critical fluid pressure in the process. The experimental procedures were conducted on two-layer sheets composed of Aluminum (1050-H0) and Carbon Steel (St13) to validate the analytical outcomes and to forecast the actual operational pressure range. It was demonstrated that the fluid pressure window for successful part forming could be efficiently predicted with reasonable accuracy using the analytical model, in comparison to extensive and costly FEA or experimental methods. [82].

Atrain et al. [158] examined the wrinkling behavior during the deep drawing process of Al3105/polypropylene/SS304. The components composed of three layers: aluminum 3105, polypropylene, and 304 steel, are manufactured by the deep drawing method. A finite element (FE) simulation of this process was conducted using ABAQUS software, and the findings of numerical and experimental investigations into the influence of blank holder force on flange wrinkling and punch force were compared. The findings demonstrate a decrease in wrinkling of the deep drawn cups with an increase in BHF [67].

Pazand et al. [159] investigated the alloy of AA3004/SUS304/Cu1011. The analysis revealed a significant influence of layer configuration in relation to the punch on the Forming Limit Diagram (FLD). Significantly, when the innermost layer of AA3105 contacted the punch during the forming operation, with the Cu1011 sandwich layer in the middle and SUS304 as the outside layer, a substantial enhancement in the formability of the clad sheet was noted. The conclusion was that the highest FLD was attained when the layer in contact with the punch was composed of the material with the lowest strength.

Karajibani et al. [160] conducted a numerical and experimental analysis of the deep drawability of a two-layered (AA/Steel) clad sheet to assess the impact of parameters including individual layer thickness, die and punch corner radius, friction coefficients at the punch-blank and die-blank interfaces, and material lay-up on the limiting draw ratio (LDR) [31]. Leu created an analytical model to forecast the punch force during the deep drawing of monolithic sheets, adding normal anisotropy based on Hill's yield criterion. This analytical model forecasted the outcomes of drawing loads for ferrous alloy sheets with an approximate inaccuracy of 5% compared to the experimental

results. The predicted punch force for copper and aluminum alloys ranged from 15% to 28% of the experimental results [69].

Azodi et al. [160] established an analytical model that predicted the punch force for monolithic sheets with the Barlat-89 anisotropic yield criterion, employing a constant material parameter value of a = 2 across all materials. The forecasts derived by Barlat-89 and Hill's anisotropic yield criterion were observed to be analogous, owing to the identical value of the material parameter utilized in both models [33]. The material parameter values of 6 and 8 were proposed for BCC and FCC metals, respectively, in the Barlat-89 yield criterion [79].

Afshin et al. [161] performed a comprehensive experimental investigation on the deep-drawing process at elevated temperatures of a two-ply AA1050/SS304 laminated sheet at three distinct temperatures. To obtain varied grain sizes, the aluminium sheet was subjected to annealing at three distinct temperatures for one hour. A larger grain size correlated with an increased coefficient of friction, which negatively affected the material's formability. The formability was notably affected by the increase in blank holder force; however, heated deep-drawing could be performed at higher temperatures with reduced load requirements.

Research gaps and Research Objectives

2.1 Research gaps

After an extensive literature survey, the following issues needs to be addressed:

1. Limited comparative analysis of anisotropy in welded and parent sheets: Although tensile properties of parent aluminium sheets are widely reported, there are few systematic investigations comparing the evolution of tensile behavior and anisotropy parameters ($\bar{R}$ and ΔR) between parent and friction stir welded (FSW)

sheets. The weld zone and thermomechanical impacted zone, in particular, have not been adequately defined in terms of directional characteristics.

2. Inadequate optimization of FSW parameters related to weld zone strength: Several researches have examined the effects of various FSW parameters on joint quality; nevertheless, extensive optimization utilizing statistical techniques that directly connect process factors with weld bead strength is lacking. The interactions between rotational speed, traverse speed, and axial force on mechanical performance have not been adequately investigated, particularly for dissimilar or custom welded setups. The effect of external energy supply on the weld strength, weld integrity and formability of the Friction Stir welded blank is needed to be studied. A few literatures are available on optimization of reduction of tool shoulder diameter to achieve a fine & sound weld joint but effect of reduction of the weld width on formability has not been studied.

3. There is a scarcity of tensile property data for FSW-based custom welded blanks: Although TWBs are extensively examined, most research focuses on laser-welded blanks. Detailed tensile characterisation of TWBs made specifically using friction stir welding, including strength mismatch and strain localization across the weld, is virtually unknown. The formability of Friction Stir welded blanks is still to be addressed due to reduced workability at room temperature due to the presence of a weld zone of significant width.

4. Limited integration of experimental data and FE-based formability prediction: Finite element analysis (FEA) has been used to predict formability; nevertheless, models frequently rely on assumed or uniform material qualities. There is a significant gap in combining empirically acquired, location-specific tensile and anisotropy

properties of FSW joints into FE simulations to improve formability prediction of welded sheets.

5. Limited experimental confirmation of FLD predictions for FSW blanks: The forming limit diagrams (FLDs) are frequently anticipated analytically, experimental confirmation via stretch forming tests on friction stir welded blanks is limited. The impact of weld line orientation, material mismatch, and weld zone heterogeneity on FLD evolution is not properly addressed in recent research.

In summary, the existing literature reveals several critical gaps in the comprehensive understanding of friction stir welded tailor welded blanks. Tensile characteristics and anisotropy in parent and welded sheets are not systematically characterized, especially when it comes to how different weld zones affect directional mechanical behavior. Robust statistical methods that directly link input parameters to weld bead strength are rarely used while optimizing friction stir welding parameters. Furthermore, as the majority of previous research has been on alternative welding methods, comprehensive tensile and formability tests on tailor welded blanks made especially using friction stir welding are still rare. Additionally, there is little incorporation of location-specific, empirically observed material properties into finite element models for formability prediction, which could result in errors. Lastly, stretch forming experiments on friction stir welded blanks are insufficient for experimental validation of anticipated forming limit diagrams.

2.2 Research objectives

1. To characterize tensile properties and anisotropy of the parent sheets and welded sheets
2. To optimize the friction stir input parameters based on the strength of weld bead
3. To characterize the tensile properties of TWBs prepared by friction stir welding process
4. To predict the formability of the welded sheet by Finite Element Analysis
5. To investigate the forming limit diagram (FLD) of the friction stir welded blanks by stretch forming experiments to validate the predicted results

CHAPTER 3

METHODOLOGY

Various experimental techniques and methods employed in the present work are described in detail in this chapter. Selection of the materials and experimental determination of tensile properties in the ambient working temperature range is presented in this chapter.

Design and development of experimental setup and control systems for conducting formability tests at ambient temperatures is presented detail followed by the actual experimental procedure. Numerical simulation procedure of stretch forming and experimental validation are also explained in this chapter.

3.1 Material selection

Two aluminium alloy sheets AA5083 and AA6082, each of 2 mm thickness are selected in an annealed condition for the study. AA5083 is a non-hardening alloy, extensively used in the sheet metal forming operations [162] in shipbuilding, rail-cars, vehicle bodies etc. due to its good formability. Whereas, AA6082 is an age hardening alloy containing nearly 1% of Si, Mg and Mn and finds its applications in structures, trusses, bridges, cranes, transport etc [163].

The combination of these alloys can be beneficial in construction application, marine, aerospace and automotive industries where high strength and corrosion resistance are required. The chemical composition of both the materials obtained by spark test is shown in Table 3.1.

Table 3.1 Chemical composition of aluminium alloys (in wt.%)

Alloy	Mg	Si	Mn	Sn	Cr	Ni	Fe	Al
AA5083	4.17	0.17	0.52	0.01	0.09	0.06	0.30	Rest
AA6082	0.99	1.11	0.59	0.07	0.25	0.07	0.23	Rest

3.2 Tensile Properties

The tensile specimens of AA5083 and AA6082 were prepared through laser cutting in accordance with the ASTM E8M sub sized standard and subjected to tensile testing to determine their mechanical properties. The tests were conducted using the H50KS Bench-top Uniaxial Testing Machine, which has a maximum load capacity of 50 kN and operates with a crosshead speed of 2.5 mm/min, as shown in Figure 3.1.

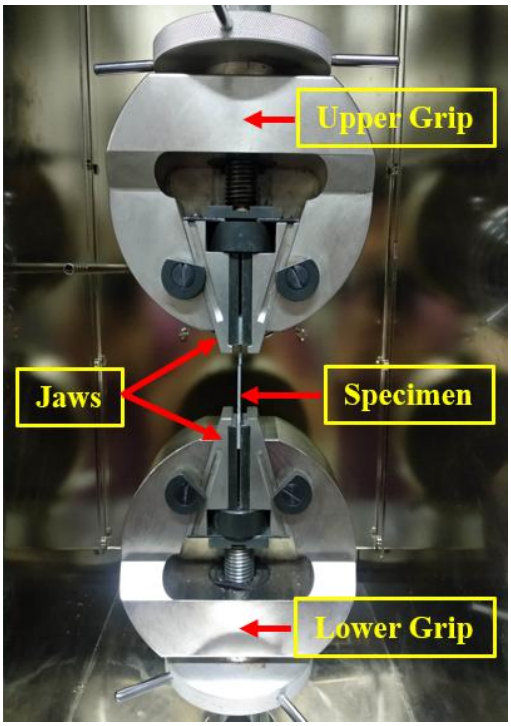

Figure 3.1 Tensile testing in progress

The universal testing machine (UTM) provides a precise force measurement within ±0.5% of the indicated load across the entire range, from 2% to 100% of the load cell's capacity.

The anisotropy of the parent sheets was determined by performing additional tensile testing as per ASTM E517-06 standard. According to this standard, the uniaxial tension tests of specimens oriented at 0°, 45°, and 90° with respect to the rolling direction were conducted by deforming the specimens to 10% elongation (below the strain at which necking occurs) and stopping the cross head in an automatic mode using the settings in the UTM. The true longitudinal and true width strains were measured in the deformed specimens followed by calculation of plastic strain ratio i.e. R_0, R_{45}, and R_{90}. In the case of FSTWBs, the anisotropy was estimated based on the weighted average method of the contribution of anisotropy of both of parent regions i.e. AA5083 and AA6082.

3.3 Determination of annealing temperature of TWBs

Pilot experiments were conducted in a muffle furnace at four distinct temperatures, namely 150˚C, 300˚C, 350˚C, and 400˚C, in order to determine the annealing temperature of the weld zone in the blanks. The aforementioned temperature range for annealing FSTWBs was selected based on research conducted by Lee et al. [164], wherein the mechanical and microstructural behaviour of cryorolled AA 5083 were experimentally studied, and the annealing temperature was systematically studied in the range of 150°C to 300°C. Similarly, the influence of annealing temperatures between 200°C and 325°C on the mechanical characteristics of cryorolled 5083 and 200°C and 350°C on cryorolled 6061 was investigated by Changela et al. [165].

During annealing, dehydrated sand was used cover the samples in order to prevent the oxidation. FSTWB samples were placed inside the chamber and heated continuously until the furnace reaches the desired temperature. The chamber was then allowed to cool and soak the samples for two hours. After annealing, the samples were tested to determine the mechanical properties.

3.4 Design of experiment

The longitudinal butt joining of AA6082 and AA5083 sheets was accomplished by friction stir welding. To determine the necessary input welding parameters for the intended mechanical properties of the welded joint, pilot experiments were conducted. Tool rotational speed (700, 800 and 900 rpm), tool travel speed (20, 25, and 30 mm/min), and tool pin to shoulder diameter ratio (5.0) were the input parameters for the welding.

3.5 Analysis of the input data for FSW and tensile properties of welded region

In friction stir welding with a good weld quality, input parameters are crucial. For the FSTWBs to have the appropriate strength and formability, a sound weld is required. Nine combinations of tool rotational and travel speeds make up the pilot experiment, and each combination has its own set of welded sheets. The tensile specimens taken from the TWBs were prepared by wire-cut electric discharge machining keeping the welded region longitudinal and transverse to the loading direction in order to determine the weld properties and integrity, respectively as shown in Figure 3.2. The true stress-true strain data obtained for the welded region was further used to model the weld zone property for the simulations.

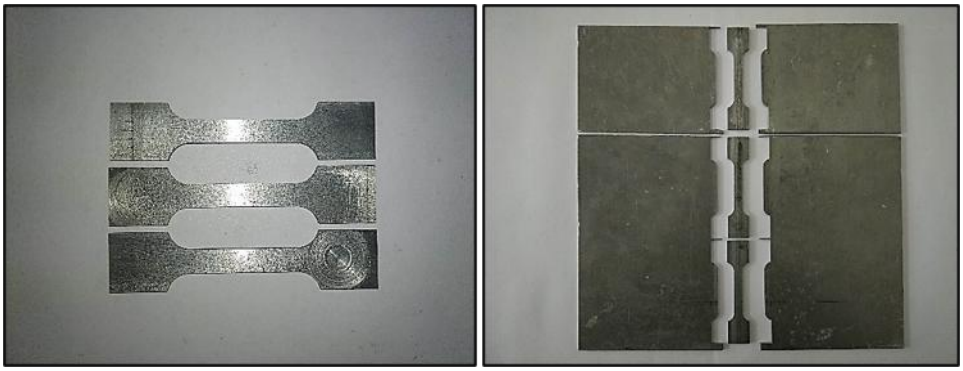

Figure 3.2 Tensile test specimen of weld zone prepared from FSTWB

With the aid of and one-way ANOVA techniques, the optimal weld was selected based on the required strength and percentage elongation. The implementation of an orthogonal array of L9 yielded the optimal process parameters for the intended response [166].

3.6 Taguchi method

Two distinct sets of independent variables, each with three levels, were utilized in pilot experiments to ensure the friction stir welding process is executed correctly. The independent variables chosen for the welding were tool rotational speed (TRS) and tool travel speed (TTS). The dependent parameters include final tensile strength, percentage elongation (for specimens with weld along the longitudinal direction, measuring weld strength), and percentage elongation (for specimens with weld along the transverse direction, measuring weld integrity). An orthogonal array (L9) was employed, and the signal-to-noise ratio was calculated using the "larger is better" criterion to identify the optimal process parameters.

Singh et al., 2022 [167] studied the fabrication of AA7075-T6-based hybrid metal matrix composites reinforced with silicon carbide (1.5–3.5 wt.%), graphite (2–4 wt.%), and S-glass fiber (3–5 wt.%) using a vacuum-sealed stir casting technique.

Employing the Taguchi L9 orthogonal array and ANOVA, they analyzed the effects of these reinforcements on micro-hardness and impact strength. The results showed an enhancement of 31.40% in micro-hardness and 33.33% in impact strength compared to the base alloy.

3.6.1 Design of Experiments

A series of tensile experiments were carried out to predict the optimum result in the terms of UTS, % elongation for determination of weld strength (ES) and % elongation for determination of weld integrity (EI). In order to determine the weld strength the tensile specimens were taken along the weld direction i.e. the longitudinal direction containing the weld region only. In order to determine the weld integrity, the tensile specimens were taken from the FSTWBs so that the weld region was transverse to the length of the specimen.

Output Parameters: UTS, % elongation for weld strength (ES), % elongation for weld integrity (EI)

Input Parameters: Tool travel speed, tool rotational speed

Objective Function: Larger is better

S/N Ratio for the function: $\{-10\mathrm{Log}_{10}\left(\frac{\mathrm{sum}(\mathrm{Y}^2)}{\mathrm{n}}\right)\}$, where, “n” is the “Sample Size” and “Y” is the “output parameters in that run”.

The process parameters and their levels are shown in Table 3.2, and the experimental matrix was created using the most likely combination of the input parameters shown in Table 3.3. The signal-to-noise ratio was determined through a total of nine experiments.

Table 3.2 Process parameters and corresponding levels

Parameters	Notation	Levels of factors		
Tool rotational speed (rpm)	TRS	700	800	900
Tool traverse speed (m/s)	TTS	20	25	30

Table 3.3 Experimentation control log using orthogonal array L_9

Experimental run	Tool traverse speed (m/s)	Tool rotational speed (rpm)
1	20	700
2	20	800
3	20	900
4	25	700
5	25	800
6	25	900
7	30	700
8	30	800
9	30	900

Experimentally measured values of UTS, ES, and EI were used as responses, and the signal-to-noise ratio was calculated using the larger is better control function. The average signal-to-noise ratio for UTS, ES, and EI was also computed. The orthogonal

array experimental data employs ANOVA to compute the response data for each parameter.

3.7 Friction Stir Welding

3.7.1 Experimental setup and process parameters

The friction stir welding by using a special machine tool (Model No. FSW 4T-HYD) was used to fabricate the TWBs as shown in Figure 3.3. The rated power of the machine is 11kW at 3000 rpm and can apply a forging load of 25kN. This machine carries a hydraulically actuated bed movement in the "X" and "Z" directions, as well as a manual movement in "Y" direction.

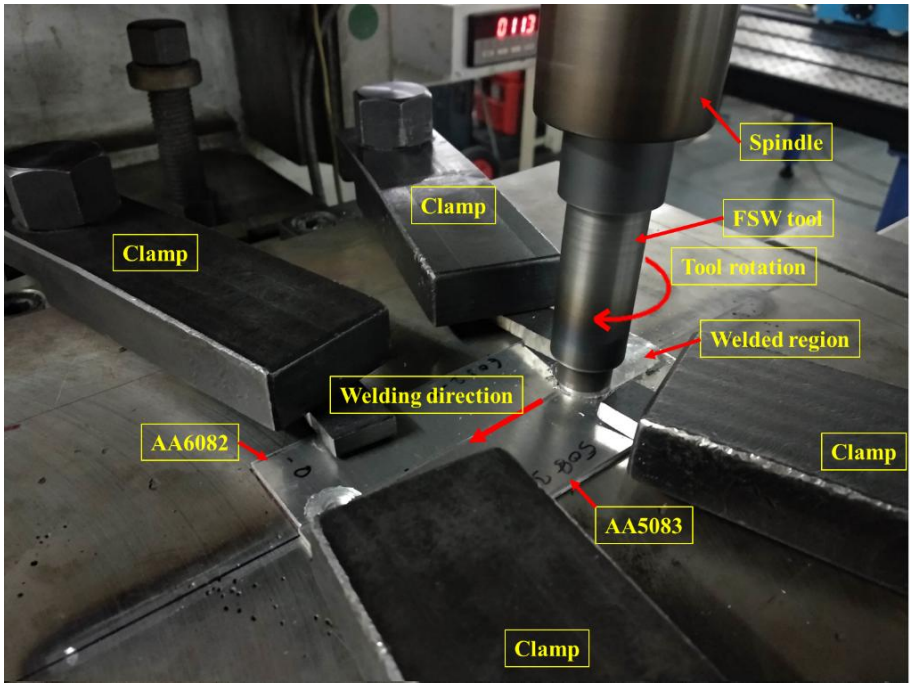

Figure 3.3 Friction stir welding experimental set up

A control panel directs the movement of the machine bed and head (mounted with a tool). A valve regulator controls the feed of the table as well as the vertical movement

of the spindle head. After the pilot experiments, the process parameters for friction stir welding were determined while keeping the tool geometry as constant. The process parameters such as the tool rotational speed and the tool travel speed were varied and the tool penetration was kept constant throughout the experiments.

Since, FSW deforms the sheets plastically and stirs to mix-up the materials from the parent sheets while translating and rotating through the sheets placed side by side in close contact to prepare a butt joint. A cylindrical tool made of H13 steel was selected possessing a hardness value of 59HRC. The specification of the FSW tool is shown in Figure 3.4.

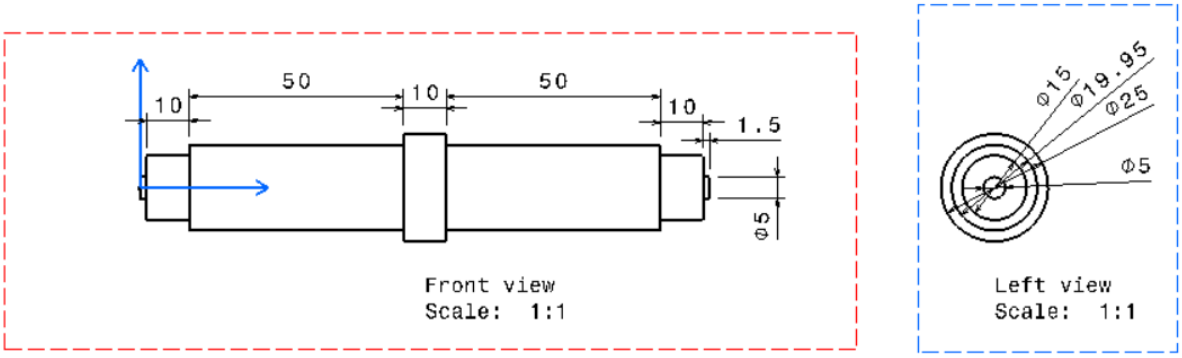

Figure 3.4 Two projection views of the FSW tool (all dimensions are in mm)

3.7.2 Residual stress measurements

As with any X-ray diffraction-based technique, it is essential to interpret the results by considering the factors such as grain size, preferred orientations, diffracting volume, and geometric alignment. The Debye ring mapping, as illustrated in Figure 3.5 -3.7, is a non-destructive method employed to evaluate residual stresses in a crystalline material via X-ray diffraction [168]. When an X-ray interacts with the crystal lattice, it produces constructive and destructive interference patterns, resulting in diffraction

rings visible on a detector screen. By rotating the sample while exposing it to X-rays, a diffraction data is collected at various angles, enabling a comprehensive mapping of the Debye ring, which captures the material's diffraction pattern.

To assess the residual stresses, the Cosα technique was utilized. This approach involves measuring the angular positions (2θ angles) of the diffraction lines relative to a reference direction, typically aligned with the material's loading axis or a designated orientation. By correlating the stress-induced strain with the angular displacement of the diffraction lines, the Cosα technique allows for the determination of the residual stresses. The magnitude of the residual stress in a specific direction is directly proportional to the cosine (Cos) of the angle (α) between the diffraction line and the reference direction [169].

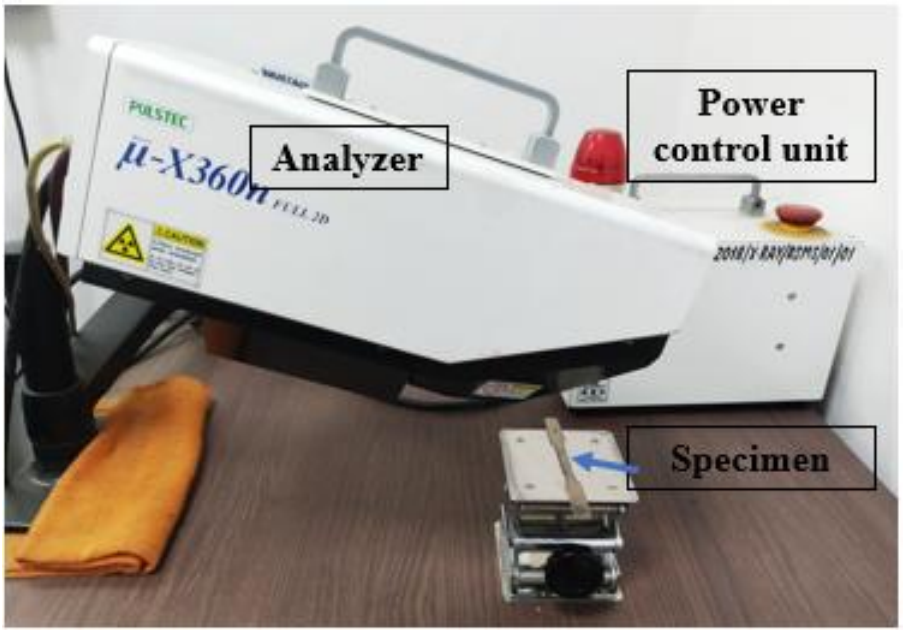

Figure 3.5 Portable X-ray residual stress measurement setup

The residual stresses are the internal, self-equilibrating stresses retained within a material after external forces are removed, which can result in uneven material

deformation. The residual stress measurement setup (PULSTEC μ-X360n) is based on the cos α method of the X-ray diffraction technique to study the influence on the residual stresses in the sheets after welding, as shown in Figure 3.5. A Debye ring mapping to evaluate residual stresses in FSTWBs is shown in Figure 3.6

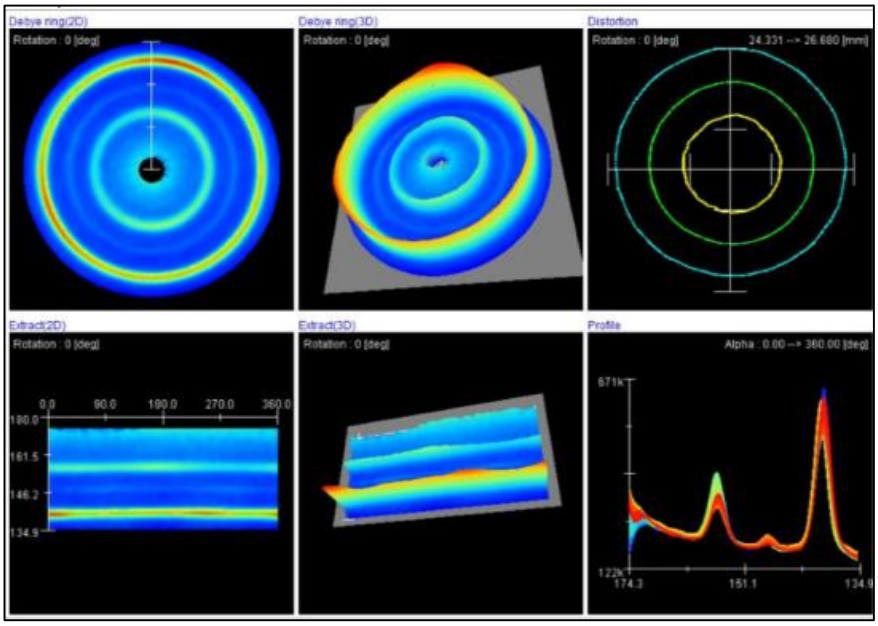

Figure 3.6 Debye ring mapping to evaluate residual stresses in FSTWBs

X-ray diffraction techniques are used for non-destructive testing of the residual stresses in the material. Taira et al. introduced the cosα method through X-ray diffraction, which could measure all plane stress components from one diffraction ring obtained by a single incident X-ray beam [168-169]. The cosα methodology leverages two-dimensional detectors to capture an entire Debye ring in one measurement, accelerating the assessment of residual stresses. Unlike traditional methods that require multiple sample tilts to gather similar data, cosα measurements are expedited and simplify the overall process. In the cosα technique utilizes the Debye-Scherrer (D-S) ring collected with a single measurement using a 2D detector. This method

incorporates Bragg's law to measure the variation in interplanar distance $(d_{\psi\varphi})$ caused by the residual stress. The strain measurement uses the D-S ring, detected on the 2D detector with a tilt angle ψ_0 from the Z axis, and rotation angle φ_0 from the X axis as shown in Figure 3.7.

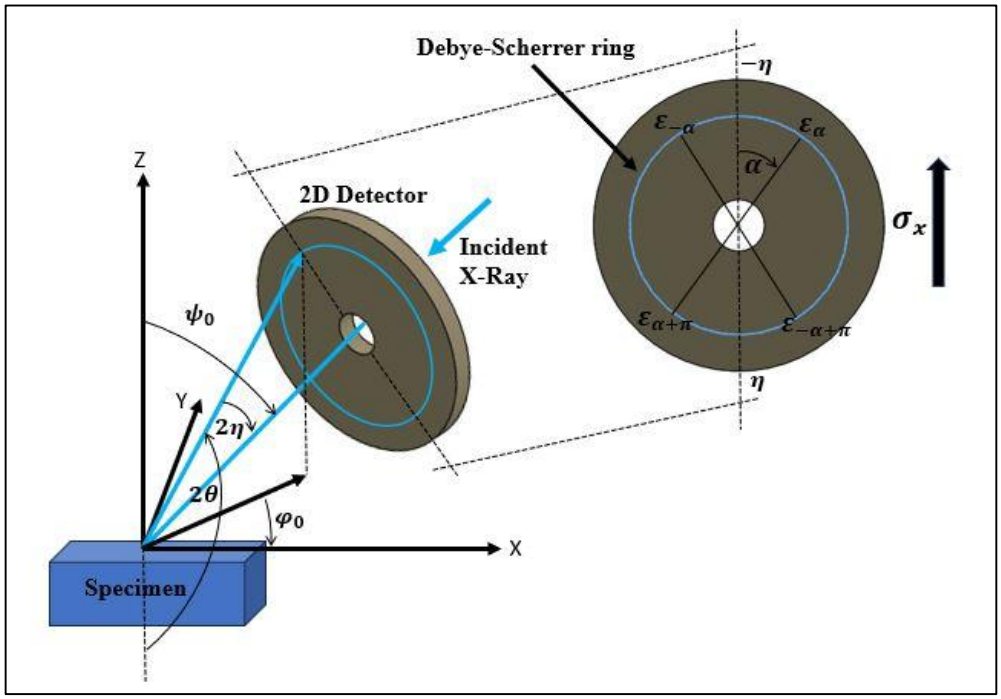

Fig. 3.7 Coordinate system of Cosα technique using a 2D detector

The strain $\varepsilon_{\psi\varphi}$, at azimuthal angle α from $-\eta$ as illustrated in Figure 3.6, is expressed as follows:

$$\varepsilon_{\psi\varphi} = \varepsilon_{\alpha} = \frac{d_{\psi\varphi} - d_0}{d_0} = n_1^2\varepsilon_x + n_2^2\varepsilon_y + n_3^2\varepsilon_z + n_1n_2\gamma_{xy} + n_2n_3\gamma_{yz} + n_1n_3\gamma_{xz} \quad (3.1)$$

where $n_i(i = 1,2,3)$ is the direction component of the diffraction vector n with respect to the sample coordinate system. The diffraction vector n is expressed as [169]:

$$n = \begin{pmatrix} n_1 \\ n_2 \\ n_3 \end{pmatrix} == \begin{pmatrix} \cos\eta\ \sin\varphi_0\cos\psi_0 - \sin\eta\ \cos\varphi_0\cos\psi_0\cos\alpha - \sin\eta\sin\varphi_0\sin\alpha \\ \cos\eta\ \sin\varphi_0\sin\psi_0 - \sin\eta\ \cos\varphi_0\sin\psi_0\cos\alpha + \sin\eta\cos\varphi_0\sin\alpha \\ \cos\eta\ \cos\varphi_0 + \sin\eta\sin\varphi_0\cos\alpha \end{pmatrix}$$

(3.2)

Now, the strain translation matrix represented by the equation, $\varepsilon_\alpha = n_i n_j \varepsilon_{ij}$ $(i, j = 1$ to 3). When combined with Hooke's law, the resulting expression is as follows:

$$\varepsilon_\alpha = \frac{1+\nu}{E} n_i n_j \varepsilon_{ij} - \frac{\nu}{E}\sigma_{kk} \tag{3.3}$$

9 where, ν is poisson's ratio, E is Young's modulus, σ_{kk} (k =1-3) is a stress component.

The mean value of the difference of strains at each azimuthal angle ($\boldsymbol{\alpha}$, $-\boldsymbol{\alpha}$, $-\boldsymbol{\alpha}+\boldsymbol{\pi}$ and $\boldsymbol{\alpha}+\boldsymbol{\pi}$) is used to determine the following two parameters (ε_{α_1} and ε_{α_2}), which is expressed as follows:

$$\varepsilon_{\alpha_1} = \frac{1}{2}[(\varepsilon_\alpha - \varepsilon_{\alpha+\boldsymbol{\pi}}) + (\varepsilon_{-\alpha} - \varepsilon_{-\alpha+\boldsymbol{\pi}})] \tag{3.4}$$

$$\varepsilon_{\alpha_2} = \frac{1}{2}[(\varepsilon_\alpha - \varepsilon_{\alpha+\boldsymbol{\pi}}) - (\varepsilon_{-\alpha} - \varepsilon_{-\alpha+\boldsymbol{\pi}})] \tag{3.5}$$

The slope of the linear relationship between the above two equations and cos $\boldsymbol{\alpha}$, determines the residual stress σ_x, which can be expressed as [169]:

$$\sigma_x = -\left(\frac{E}{1+\nu}\right)\left(\frac{1}{sin2\eta sin\psi_0}\right)\left(\frac{\partial\varepsilon_{\alpha_1}}{\partial\cos\alpha}\right) \tag{3.6}$$

where, $\left(\frac{\partial\varepsilon_{\alpha_1}}{\partial\cos\alpha}\right)$ is the slope between the parameter ε_{α_1} and $cos\ \alpha$.

The information about residual stresses improves the design engineer's understanding and provides valuable insight into the deformation behavior during forming operations. The distribution of these stresses can influence the service performance of

welded components, particularly in terms of fatigue resistance and corrosion properties, which may lead to a potential failure.

3.7.3 Microstructural characterization

The specimens from the weld region and parent sheets were prepared using standard metallographic techniques to achieve reliable microstructural investigation. The sample was cold mounted using a resin containing a hardener accelerator, which provided enough gripping, stability, and placement for the next preparation stages. Polishing was done in two steps, first with dry polishing to remove surface imperfections and achieve initial planarization, then with wet polishing to provide a smooth and scratch-free finish. The final wet polishing was done with alumina powder on a velvet cloth, which produced a mirror-like quality suited for microstructural investigation. To show the microstructural characteristics of the weld region, the polished specimen was etched with a picral solution, which efficiently emphasized grain boundaries and phase distributions for comprehensive metallographic analysis.

3.7.4 Microhardness of welded region

Microhardness of the weld region was tested on the samples taken from FSTWBs through a line mapping across its cross-section. The Vickers method with a microhardness scale of HV0.05 was applied with a dwell time of 10 seconds. A 500 gf load was applied using a STRUER make DURAMIN 40 model employing a diamond pyramid indenter. The microhardness values were measured by first loading the specimen and then letting the material settle for a while after indentation, followed by measuring both the indentation diagonals.

3.8 Formability study of TWB using limiting dome height tests

FSTWBs were laser marked on one side of the sheet with a circular grid pattern of 5mm diameter circles. The speed of laser marking operation was set at 500 mm/s with a frequency of 20kHz. The laser marking circular grid pattern on a FSTWB is shown in the Figure 3.8.

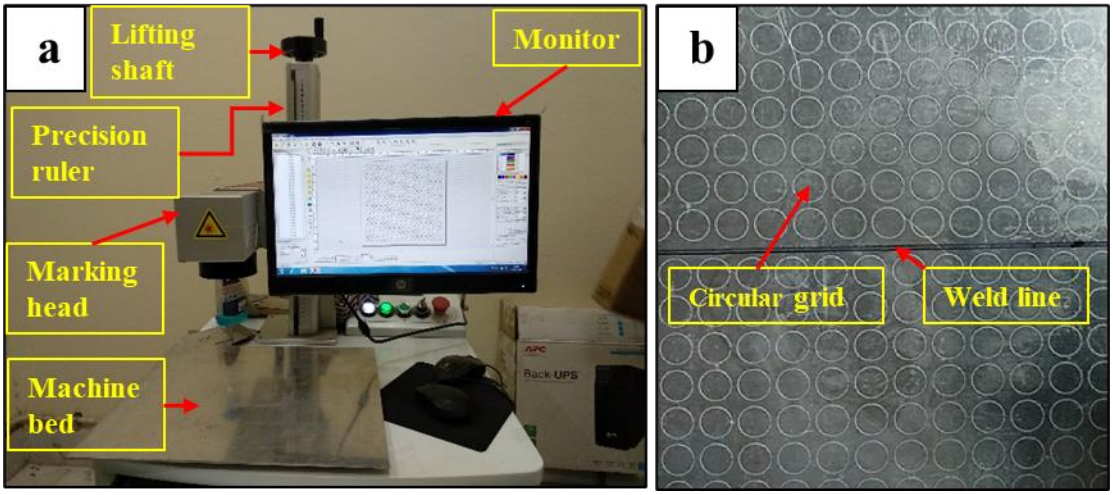

Figure 3.8 (a) Computerized laser marking setup and (b) a laser marked grid pattern on the backside of a TWB

Samples required to perform the formability test in different modes were prepared with the help of a 1 kW hydraulic operated optical fibre laser cutting machine (HSG LASER make) as shown in Figure 3.9 (a). The widths of the samples in the central region were taken as 20mm, 30mm, 40mm, 50mm, 60mm, 70mm, 80mm and 100mm. The weld line was kept along the length of the specimens in order to evaluate the weld zone effect on different modes of deformation during the limiting dome height experiments.

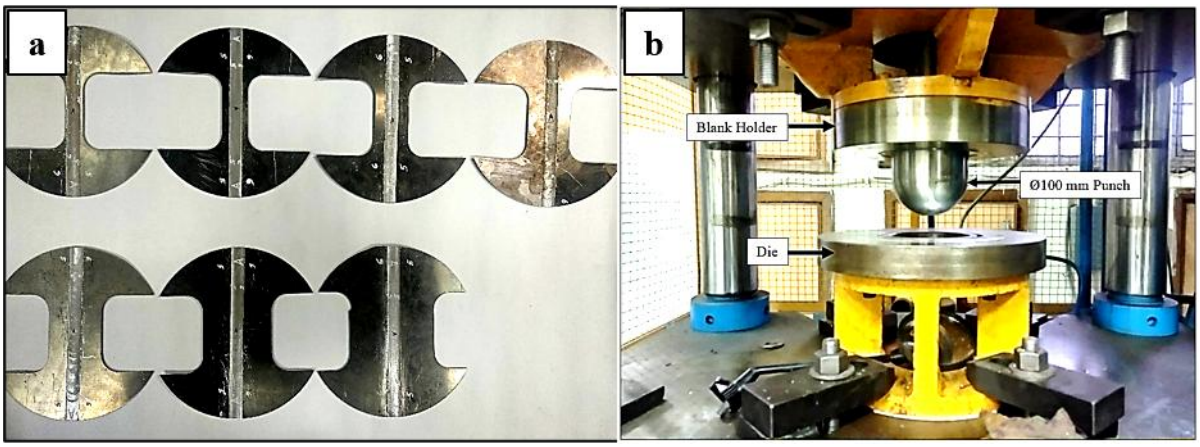

Figure 3.9 (a) Laser cut samples for LDH test and (b) experimental setup

All the forming limit experiments were carried out on a 100 Ton double action hydraulic press as shown in Figure 3.9(b). For accurate stroke measurement and control, a dedicated encoder is offered in the machine for data acquisition. The encoder uses an analog card and programmable logistic controller (PLC) to sense the data, and it displays the data on a touch screen with a minimum count of 0.1 mm. To capture the load and displacement data, a load cell is fitted in the main cylinder. Initially, the blank holder was lowered manually on the die to lock down the sheet in place. Then, depending on the sample width, the punch was moved downward to deform the locked blank in various modes of deformation till necking appears in the deformation zone. The dome heights of stretch formed samples were measured with the help of a digital vernier height gauge.

The major and minor diameters of the deformed circle i.e. ellipse were measured with the help of a trinocular stereo zoom microscope as shown in Figure 3.10. The major and minor strains were calculated at the necked and failure regions and plotted to get the forming limit diagram for annealed and non-annealed FSTWBs.

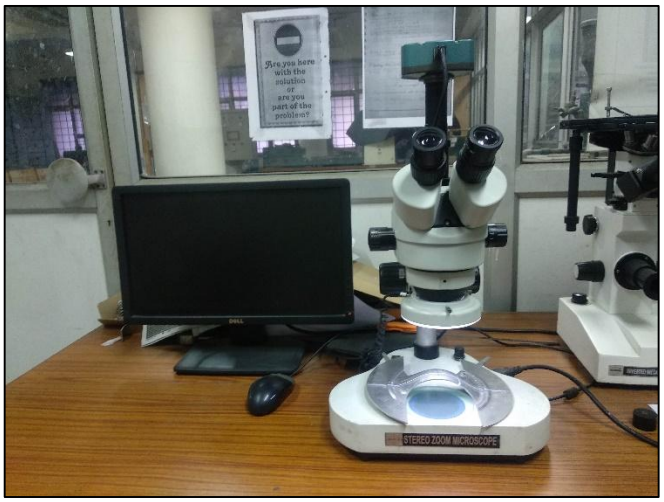

Figure 3.10 Measurement of major and minor diameters on a tested sample

3.9 Simulations for LDH

Simulations were conducted to predict the formability of FSTWBs for both annealed and non-annealed materials using ABAQUS/CAE 6.14-2 software. The blank was modeled as a 3D deformable shell, while the punch, die, and blank holder were rendered as 3D discrete rigid bodies. The sketcher tool was employed to design the FSTWB, which was divided into three distinct segments: AA5083, AA6082, and the welded region at the center. Material properties were assigned to each partitioned region, and the blank was meshed with the S4R elements (a 4-node doubly curved thin shell, with reduced integration, hourglass control, and finite membrane strain capabilities). The complete tooling assembly with the FSTWB in position, is illustrated in Figure 3.11.

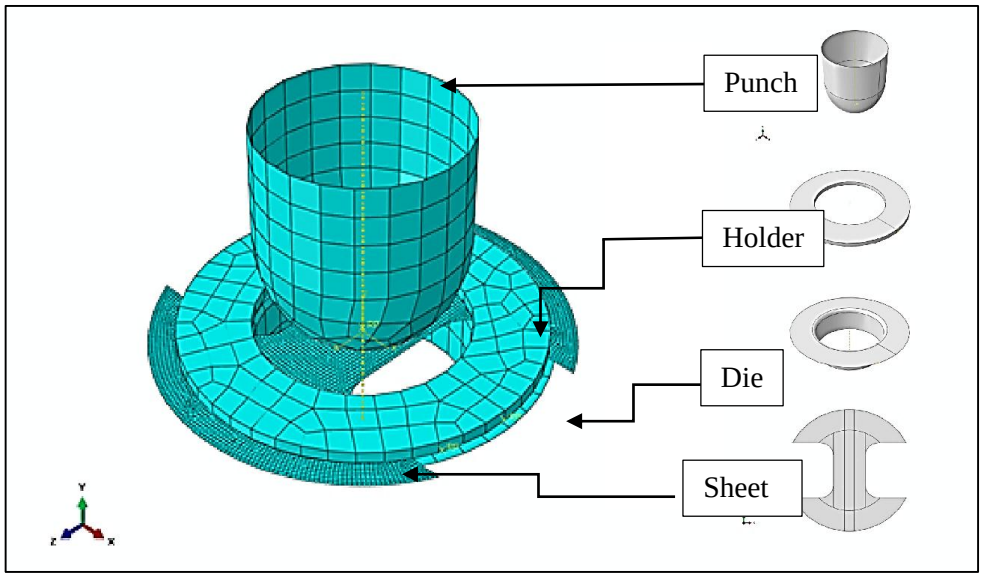

Figure 3.11 Assembly of the parts to perform simulations

The interacting surfaces of toolings and blank were given interaction attributes. To execute the simulation, the boundary conditions were provided. The tools were designated as the master surface, while the blank was designated as slave surface. A one-way surface-to-surface contact was used to specify the surface between the blank and each tool. All of the tools were aligned with the working direction (y-axis). To avoid initial tool penetration, a space equal to the blank thickness was provided between the blank and the tools. The punch was given a displacement equal to the displacement given in experiments till necking occurs in the specimens.

To allow material in contact with punch to flow into the die, a blank holding force of 2kN to 3kN was applied on the blank. A Coloumb's friction model was considered to define a friction value of 0.05 between the blank and the punch surfaces and a value of 0.10 between blank and the die surfaces.

The plastic data obtained from tensile experiments were used to define the material model. Anisotropy of sheets was also incorporated into material model using Hill's

plasticity model, also referred to as Hill's 1948 yield potential [170]. It is expressed in terms of rectangular Cartesian stress components as follows:

$$f(\sigma) = \sqrt{F(\sigma_{22}-\sigma_{33})^2 + G(\sigma_{33}-\sigma_{11})^2 + H(\sigma_{11}-\sigma_{22})^2 + 2L\sigma_{23}^2 + 2M\sigma_{31}^2 + 2N\sigma_{12}^2} \quad (1)$$

where, F, G, and H are constants obtained by uniaxial tension tests and L, M and N are determined by shear tests on the material in different orientations.

The user defined reference yield stress is denoted by σ_0; anisotropic yield stress ratios are represented by R_{11}, R_{22}, R_{33}, R_{12}, R_{13} and R_{23}; and each $\bar{\sigma}_{ij}$ is the measured yield stress value when $\bar{\sigma}_{ij}$ is applied as the only non-zero stress component. The ratios, $\frac{\bar{\sigma}_{11}}{\sigma_0}, \frac{\bar{\sigma}_{22}}{\sigma_0}, \frac{\bar{\sigma}_{33}}{\sigma_0}, \frac{\bar{\sigma}_{12}}{\tau_0}, \frac{\bar{\sigma}_{13}}{\tau_0}$ and $\frac{\bar{\sigma}_{23}}{\tau_0}$ are the yield stress ratios for the material, where $\bar{\sigma}_{11}$, $\bar{\sigma}_{22}$, $\bar{\sigma}_{33}$, and $\bar{\sigma}_{13}$ are the yield stresses along the rolling, transverse and diagonal directions, respectively. Therefore, the following expressions are used to calculate the yield stress ratios,

$$R_{11} = R_{12} = R_{23} = 1 \quad (2)$$

$$R_{22} = \sqrt{\frac{R_{90}(R_0+1)}{(R_0+R_{90})}} \quad (3)$$

$$R_{33} = \sqrt{\frac{R_{90}(R_0+1)}{R_0(R_{90}+1)}} \quad (4)$$

$$R_{13} = \sqrt{\frac{3(R_0+1)R_{90}}{(R_{90}+R_0)(2R_{45}+1)}} \quad (5)$$

where R_0, R_{45} and R_{90} are the experimentally obtained plastic strain ratios for the specimens orientated with respect to the RD at 0°, 45°, and 90°. Table 3.4, provides

the different yield stress ratios that were employed in the simulations to account for anisotropy in the cases of AA5083 and 6082 alloys. It is assumed that the weld zone is composed of an isotropic material, its yield stress ratio values were defined as unity in the simulations.

Table 3.4 Yield stress ratios used in FEA to incorporate anisotropy of EDD steels

Al alloys	R_{11}	R_{22}	R_{33}	R_{12}	R_{13}	R_{23}
5083	1	0.929	1.023	1	0.976	1
6082	1	0.939	1.058	1	1.078	1
Weld zone	1.0	1.0	1.0	1.0	1.0	1.0

The individual material properties were assigned for the three different regions i.e. two different parent materials on either side of the weld zone, in the simulations of FSTWBs during deformation.

CHAPTER 4

RESULTS AND DISCUSSION

4.1 Tensile properties

The tensile properties of AA5083 and AA6082 are presented in Table 4.1. It is observed that the yield and tensile strengths on an average basis for AA5083 are observed to be 204MPa and 261MPa, respectively. A value of 14% elongation and strain hardening exponent of 0.21 indicates moderate formability for this alloy. AA6082 possesses a yield strength of 86MPa and a tensile strength of 138MPa on an average basis indicating it as a softer material than AA5083. A higher value of ductility and strain hardening exponent renders this material to possess a higher formability when compared to AA5083.

Table 4.1 Tensile properties of parent sheets

Al Alloys	Yield stress (MPa)	UTS (MPa)	% Elongation	Strain hardening exponent (n)	Strength coefficient (MPa) (K)	Normal anisotropy ($\bar{R}$)
AA5083-O	204±2.05	261±2.49	13.9±0.33	0.21	329	0.779
AA6082-O	88±1.63	138±1.24	20.5±1.28	0.27	288	0.652

The mechanical properties for the welded region of FSTWB obtained at different annealing temperatures are given in Table 4.2. The plots of engineering stress-engineering strain obtained at different annealing temperatures are shown in Figure 4.1. A slight reduction in strength and increase in ductility and strain hardening exponent is observed in the specimens annealed at 150ºC. As the annealing

temperature increases to 300 ºC, the effect becomes more pronounced on tensile properties. It is interesting to observe that at 350 ºC, the material shows lower in strength but higher in ductility and the value of strain hardening exponent is also higher at 0.28. At 400 ºC, the properties like tensile strength and strain hardening exponent are further reduced indicating a reduction in stretching with uniform elongation. Therefore, an annealing temperature of 350 ºC offers the best combination of tensile properties required for higher formability and hence this temperature has been chosen for characterizing the formability.

Table 4.2 Mechanical properties of welded region

Annealing temperature (°C)	Yield strength (MPa)	UTS (MPa)	% Elongation	Strain hardening exponent (n)	Strength coefficient (MPa) (K)
150	221±2.86	292±3.29	15.5±0.16	0.19	495
300	90±2.45	136±3.09	21.2±0.33	0.25	286
350	75±1.24	120±1.24	25.1±0.20	0.28	239
400	69±1.63	114±1.24	24.1±0.24	0.19	188

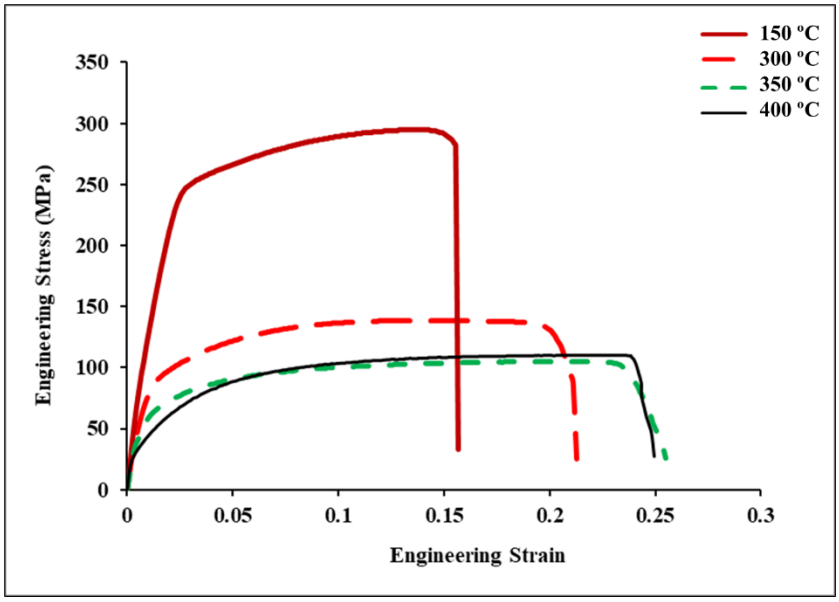

Figure 4.1 Engineering stress vs. engineering strain plots of the welded region annealed at different temperatures

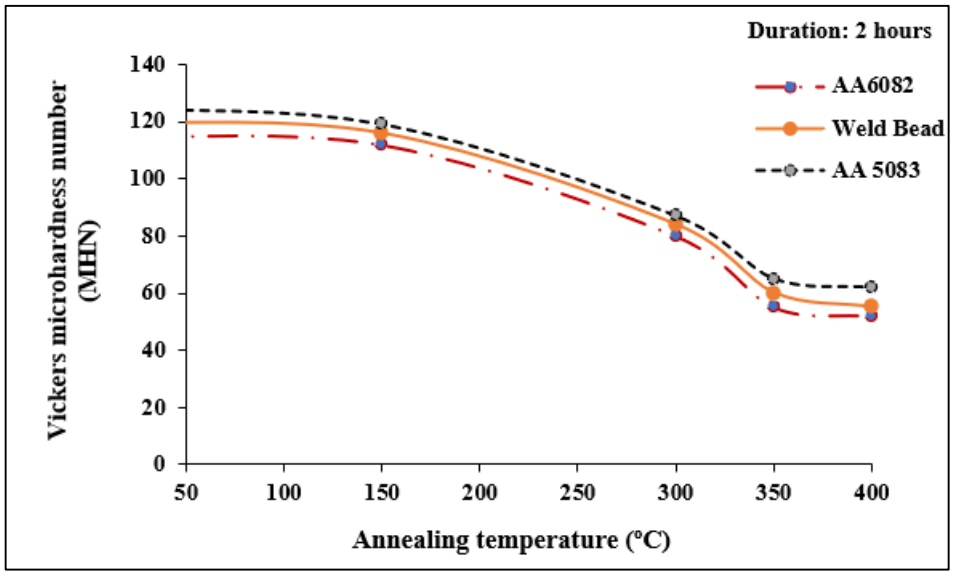

Figure 4.2 Variation of Vickers hardness at different annealing temperatures

The variation of microhardness with the annealing temperatures are shown in Figure 4.2. The microhardness of different regions in a welded sheet specimen varies significantly with the annealing temperatures. The value of hardness remains almost

constant till 150°C and drops significantly at 300°C owing to the softening of the material. The drop in the hardness values becomes more significant at higher temperatures of 350°C and then stabilizes at 400°C. The variation in the hardness of AA6082, AA 5083 and weld bead regions at different temperatures are observed to be similar due to diffusion and dissolution of hardening precipitates in the stir zone. The final annealing temperature of 350°C is selected on the basis of the tensile properties and hardness values.

4.2 Residual stress in the welded blanks before and after annealing

The characterization of residual stress set up in the blank, either tensile or compressive in nature, plays an important role to understand the behaviour of material during plastic deformation. The distribution of residual stress is mapped across the weld zone on the tool side (top side_T) and table side (bottom side_B) before and after the annealing and the results are plotted in Figure 4.3 (a) and (b).

During residual stress measurement for the blank without annealing, the position of the X-ray beam was taken 3mm apart between two consecutive points of measurements from the centre line of the welded region and on both the sides (left- and right-hand side) of the FSTWB up to 15 mm which includes the welded region and parent materials. The residual stresses were measured on a (311) lattice plane of the blank. It is observed that the residual stress is compressive in nature in both the cases of top and bottom sides of the FSTWB, although the distribution pattern is seen to follow an increasing and decreasing trend of stress across the weld zone. It is interesting to observe that the distribution of RS is more or less uniform on the parent side of AA5083 but lesser in magnitude and increases slightly at the interface of

welded region and parent material. The variation of RS remains uniform from the centre of the weld towards AA6082 (till 5mm from the centre) but it becomes abruptly highest at a distance of 10mm and then reduces to a lowest value at the interface of weld and parent AA6082 (at a distance of 15mm across the weld on right hand side) and then increases rapidly in the parent sheet. This reduction in the magnitude of RS can be attributed to the rotation of the tool away from the AA6082 so that the softer material is pulled in tension and accumulated at the centre of the weld to mix with AA5082 which is comparatively stronger. The broad serrated marks on the top surface of the welded region are clearly seen near interface of AA6082 whereas the top surface is more uniform on the welded region towards the interface of AA5083. A smooth burnishing mark of width equal to the shoulder of the tool is observed to appear on the bottom surface of the FSTWB which could be attributed to the forging pressure applied during welding.

It is observed that after annealing, the residual stress is reduced significantly and the results are displayed in Figure 4.3 (a). It is also observed that the variation of RS is more or less uniform in both welded region and parent sheets after the annealing. The residual stress is also measured on the bottom surface of the FSTWB and the results are plotted in Figure 4.3 (b). The bottom surface appears much smoother as the tool did not dig till the bottom surface which may be attributed to the design of the tool tip. It is observed that the RS across the weld region from parent material AA5083, is compressive in nature and increases gradually towards the weld centre. The RS falls rapidly till 5mm away from the weld centre and becomes minimum (value) owing to the fact that no plastic deformation has taken place at the bottom surface. The magnitude of RS increases abruptly to (value) and then decreases again in the parent

AA6082. The variation of RS in the bottom surface of the blank can be attributed to the forging pressure applied during the welding of the sheets. It is also observed that after annealing, the residual stress has been reduced significantly in the welded region but some RS is still seen in the parent material (AA6082) and the results are displayed in Figure 4.3 (b).

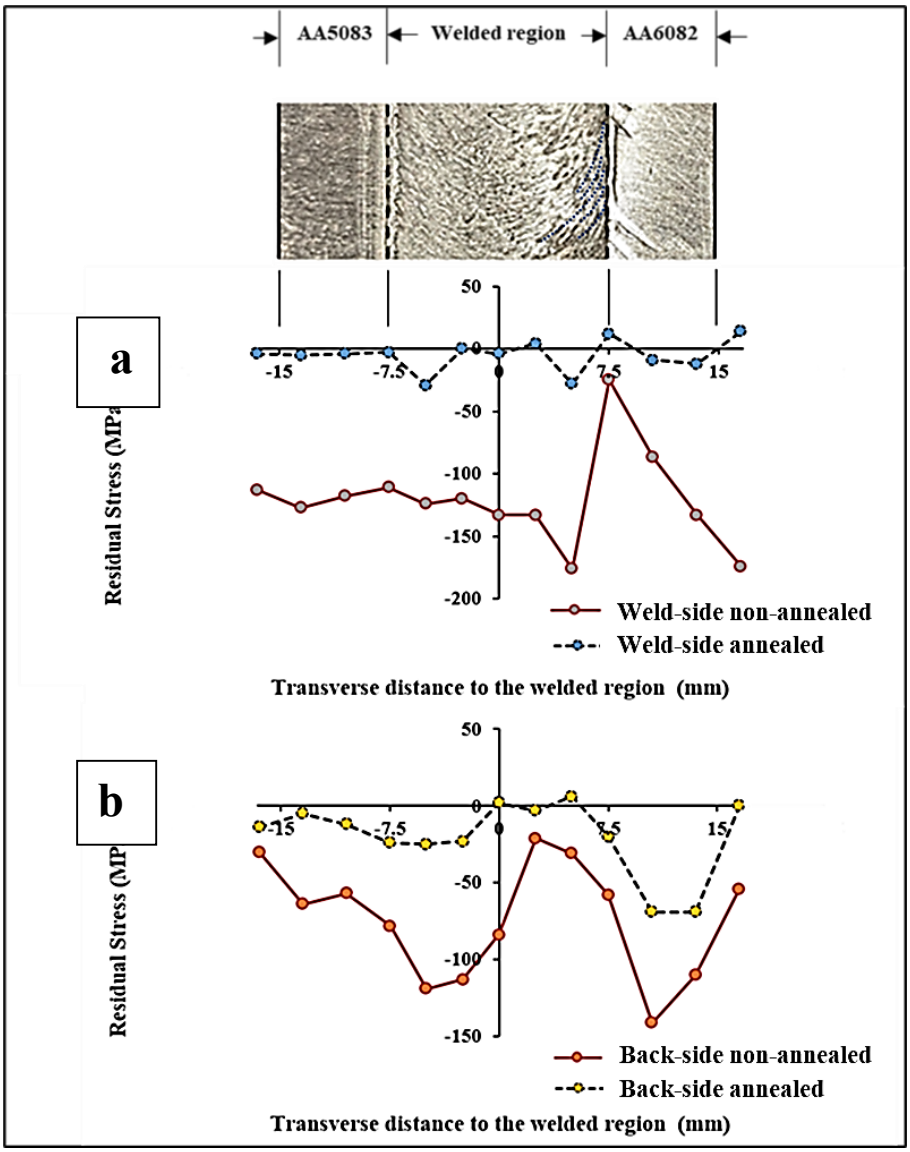

Figure 4.3 Residual stress distribution across the weld zone on (a) the top weld side surface and (b) bottom surface of FSTWB

4.3 Taguchi analysis

Experimentally measured values of UTS, % Elongation (ES) and % Elongation (EI) are shown in the Table 4.3. The Table serves as a foundation dataset for conducting Taguchi analysis to optimize the welding process parameters. It includes key experimental outcomes such as the tensile strength of the weld and the percentage elongation in both longitudinal and transverse directions. These metrics are critical in assessing the mechanical performance of welds under varying experimental conditions, providing insights on process parameters which influence strength and ductility.

Table 4.3 Experimental Results of Welded specimens

Experimental run	UTS for weld (MPa)	% Elongation (ES) (Longitudinal)	% Elongation (EI)(Transverse)
1	220	22.6	18.0
2	235	24.5	20.4
3	230	20.1	17.5
4	222	20.0	18.9
5	232	26.5	24.2
6	231	17.6	18.0
7	235	24.7	18.2
8	239	26.0	23.0
9	231	18.0	17.5

As per objective function (UTS, %Elongation (ES) and %Elongation (EI)) larger is Better control function was used to get the signal-to-noise ratio which is shown in Table 4.4.

Table 4.4 S/N ratio for different experimental run

Experimental run	S/N ratio (dB) for UTS	S/N ratio (dB) for % Elongation (ES)	S/N ratio (dB) for % Elongation (EI)
1	46.84	27.08	25.11
2	47.42	27.78	26.19
3	47.23	26.06	24.86
4	46.93	26.02	25.53
5	47.31	28.46	27.68
6	47.27	24.91	25.10
7	47.42	27.85	25.20
8	47.57	28.29	27.23
9	47.27	25.10	24.86

The average of the signal to noise ratios for UTS is shown in Figure 4.4 and the values are given in Table 4.5.

Table 4.5 The average of the signal to noise ratios for UTS

Level	Tool Travel Speed		Tool Rotational Speed	
	Sum	Avg. S/N ratio	Sum	Avg. S/N ratio

1	141.49	47.16	141.20	47.06
2	141.51	47.17	142.30	47.43
3	142.26	47.42	141.78	47.26

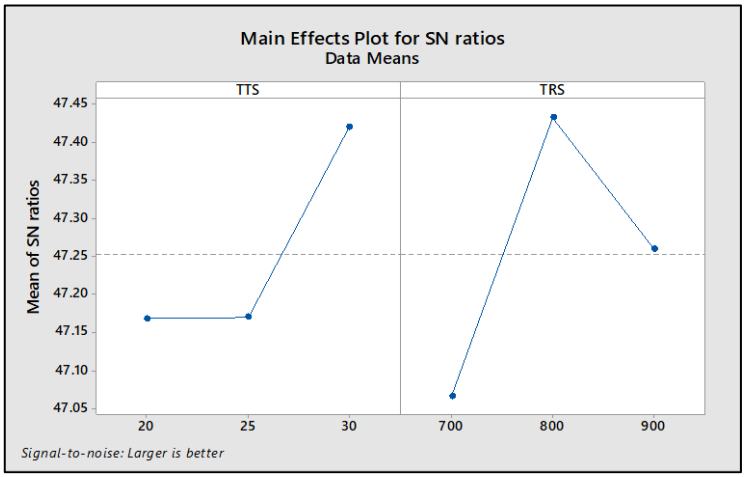

Figure 4.4 Graphical plot of mean of S/N ratios -TTS and TRS for UTS

The average of the signal to noise ratios for % Elongation (ES) is shown in Figure 4.5 and the respective values are given in Table 4.6.

Table 4.6 Average of the signal to noise ratios for % Elongation (ES)

Level	Tool Travel Speed		Tool Rotational Speed	
	Sum	Avg. S/N ratio	Sum	Avg. S/N ratio
1	80.94	26.98	80.97	26.99
2	79.41	26.47	84.54	28.18
3	81.27	27.09	76.08	25.36

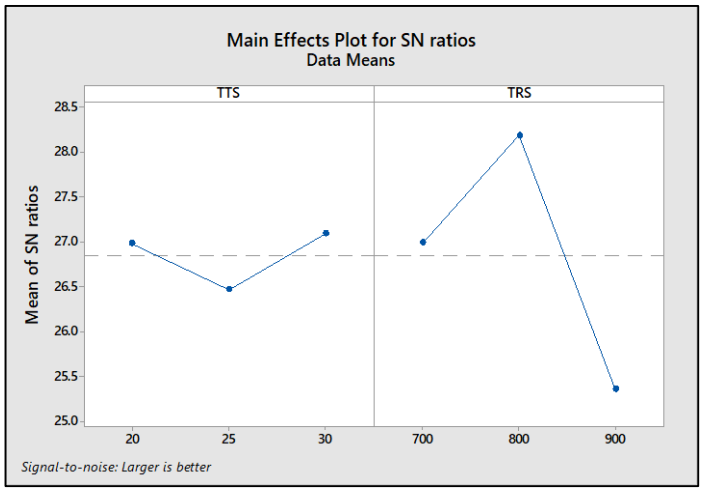

Figure 4.5 Graphical plot of mean of S/N ratios -TTS and TRS for % Elongation (ES)

The average of the signal to noise ratios for % Elongation (EI) is shown in Figure 4.6 and the values are given in Table 4.7.

Table 4.7 The average of the signal to noise ratios for % Elongation (EI)

Level	Tool Travel Speed		Tool Rotational Speed	
	Sum	Avg. S/N ratio	Sum	Avg. S/N ratio
1	76.17	25.39	75.84	25.28
2	78.30	26.10	81.09	27.03
3	77.31	25.77	74.82	24.94

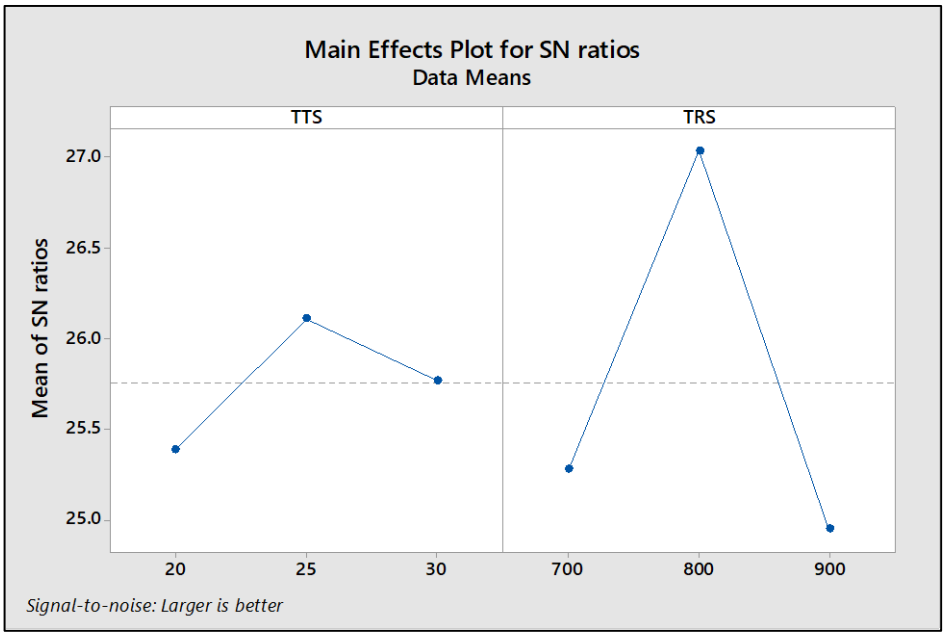

Figure 4.6 Graphical plot of mean of S/N ratios -TTS and TRS for % Elongation (I)

The Table 4.7 presents the average signal-to-noise ratios for percentage elongation based on two process parameters: TTS and TRS, each evaluated at three different levels. For TTS, the total S/N ratios at Levels 1, 2, and 3 are 76.17, 78.30, and 77.31, respectively, resulting in average S/N ratios of 25.39, 26.10, and 25.77. Similarly, for TRS, the total S/N ratios at Levels 1, 2, and 3 are 75.84, 81.09, and 74.82, with corresponding average S/N ratios of 25.28, 27.03, and 24.94. These results highlight that Level 2 is optimal for both parameters, producing the highest average S/N ratios (26.10 for TTS and 27.03 for TRS), which indicates improved and consistent % Elongation. In contrast, Level 1 for TTS and Level 3 for TRS show relatively lower average S/N ratios, reflecting suboptimal performance for elongation. Thus, Level 2 of both TTS and TRS provides the most favourable conditions for maximizing the % Elongation. In view of the above analysis, it is also observed, that the optimum values for tool travel and tool rotation are 30mm/min and 800rpm, respectively.

4.4 ANOVA RESULTS

Analysis of variance is used to calculate response data of each parameter in the selected orthogonal array experiments. The Table 4.8 presents the results of the ANOVA for evaluating the influence of TTS and TRS on the response variable, such as % Elongation, in a friction stir welding process. The analysis includes degrees of freedom (DF), adjusted sums of squares (Adj SS), adjusted mean squares (Adj MS), F-values, and P-values. For TTS, the DF is 2, the Adj SS is 4.516, the Adj MS is 2.2578, and the F-value is 2.48, with a P-value of 0.199, indicating that TTS does not have a statistically significant effect on the response at the 0.05 significance level. On the other hand, TRS shows a higher Adj SS of 41.536, an Adj MS of 20.7678, an F-value of 22.79, and a P-value of 0.007, highlighting its statistically significant impact on the response. The error term has a DF of 4, an Adj SS of 3.644, and an Adj MS of 0.9111, contributing to the total Adj SS of 49.696. These findings suggest that TRS has a dominant and significant influence on the response, while the effect of TTS is comparatively smaller and not statistically significant under the given experimental conditions.

40

Table 4.8 Analysis of variance for TTS and TRS

Source	DF	Adj SS	Adj MS	F-value	P-value
TTS	2	4.516	2.2578	2.48	0.199
TRS	2	41.536	20.7678	22.79	0.007
Error	4	3.644	0.9111		
Total	8	49.696			

The maximum value of SN ratio is selected to get the optimum mechanical properties and FSW was done at 800 rotational speed and 30 mm/min for all the specimens for further study.

4.5 Microstructural examination

The microstructures of parent sheets AA 5083-O and AA6082-O are presented in Figure 4.7 (a) and 4.7 (b), respectively. A fine precipitate of Mg-Si particles is observed to be scattered in the matrix of aluminium as shown in Figure 4.7 (a). A dark speck of Al-Mn-Si precipitate are seen to be uniformly distributed in the matrix of aluminium in AA5083 as shown in Figure 4.7 (b). The graphs of friction stir weld region before and after annealing is presented in Figure 4.7 (c)-(d), respectively. Multiple broad streaks of material flow of AA6082 due to friction are observed in the micrograph of weld region before annealing. After annealing, these streaks of material flow are observed to completely merge in the matrix of both the materials leaving a sign of a mixing boundary as also shown in Figure 4.7 (c) Annealing results in the consolidation of the materials in a uniform manner and plays a major role in removal of the dislocations so that stress concentration is reduced in the welded region.

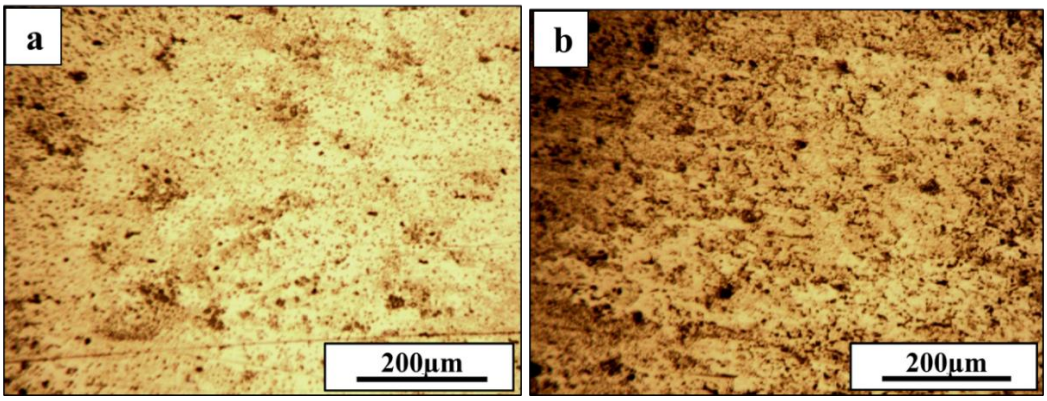

Figure 4.7 Micrographs of (a) AA5083-O, (b) Microstructure of AA6082-O

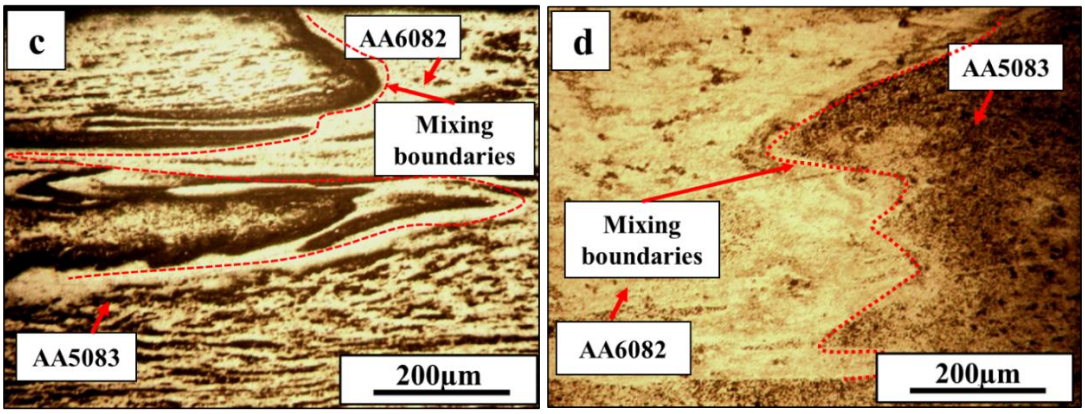

Figure 4.7 Micrographs of (a) AA5083-O, (b) AA6082-O Microstructure of (c) weld zone before annealing and (d) weld zone after annealing

4.6 Microhardness

The results of Microhardness obtained across weld region over a line mapping is plotted and shown in Figure 4.8 (a) and (b) for annealed and non-annealed specimens. The line mapping was done on the cross-section of the FSTWB of a total length of 25 mm which comprises of 5mm of AA5083 (parent sheet) towards the weld region, 15 mm of weld region and 5mm of AA6082 (parent sheet) away from the weld region. Form the plot, it can be concluded that the hardness of AA5083-O has a higher value of hardness as compare to AA6082-O. The microhardness value on an average basis for AA5083-O measured up to 5 mm is 91 HV0.05 followed by a gradual rise and fall in hardness at the interface of weld while entering into the weld region with an average value of 95 HV0.05. There is slight rise in the hardness of the weld zone towards the mixing zone of AA5083 but the rise is significant in the weld zone towards AA6082.

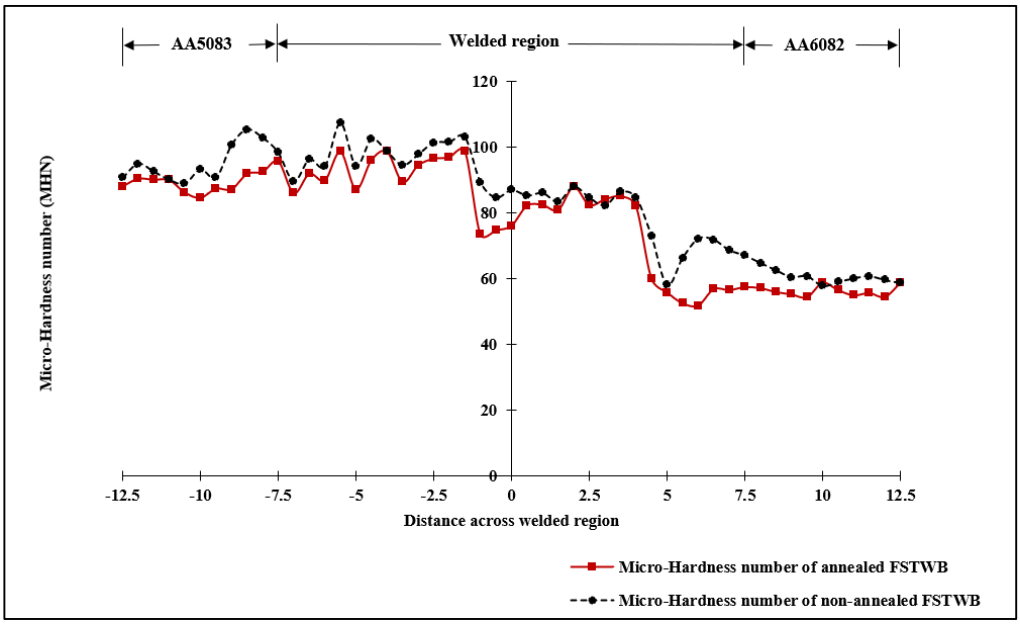

Figure 4.8 Variation of hardness across the welded region of a (a) annealed and (b) non-annealed FSTWB

Since the material has interlocked with severe strain hardening and plastic deformation, the centre region of the weld bead has the highest average hardness, measuring 105 HV. The average hardness value declines as it gets closer to AA6082-O, ending with an average value of 70 HV for the entire sample. The hardness data points for annealed FSTWB are also displayed in Figure 4.8. It is found that after annealing, the welded sheet's hardness has decreased significantly. Similar results are observed in the hardness profile of the annealed sheets. Annealing has slightly reduced the hardness in the weld zone which could be attributed to the grain refinement due to severe plastic deformation. The average hardness value of an annealed welded blank is 72 HV when it is measured from the AA5083-O side, approximately 74 HV inside the weld region moving towards the centre, 83 HV in the centre region, and 54 HV in the parent sheet of AA6082-O as depicted in Figure 4.8.

4.7 Fractography, EDX analysis and XRD

The fractured surfaces of the parent materials and the weld zone of FSTWB are studied using scanning electron microscopy technique. The fracture surfaces of AA5083, weld region and AA6062 samples tested in uniaxial tension are shown in Figure 4.9 (a)-(c), respectively. The fracture micrographs are compared on the basis of the formation of micro-voids and cleavage crack surfaces.

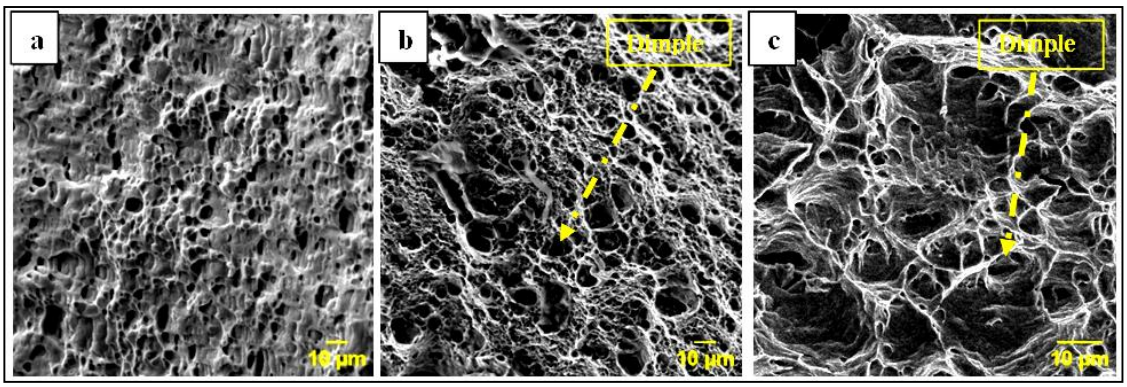

Figure 4.9 Fractographs for (a) AA5083, (b) weld region of FSTWB and (c) AA6082

The micro-voids appeared in the AA5083 are comparatively smaller in size which indicates lower ductility and higher strength. A majority of the micro-voids are observed to have closed surfaces. In the case of the fracture surface of the weld zone, a mix of very fine and coarse micro-voids are observed indicating a reduction in strength but a slight improvement in ductility after annealing. It is also observed in the fracture surfaces of parent AA6062, the depth and size of dimples appear to have increased which indicates larger deformation prior to failure (higher limit strains). The fracture surface shows a combination of elongated and bigger micro-voids when compared to other micrographs. In almost all the cases the failure seems to have occurred due to nucleation and growth of micro-voids at or near inclusions/second

phase particles which are found at many locations near the cavities in the fractured areas. The spectrum obtained by the EDX microanalysis in Figure 4.10 shows evidence of the presence of elements like Fe, Mg, C, Si and O in the parent materials and in the welded region. The microanalysis confirms the presence of elements in the weld region contributed by the parent materials. The figure shows the presence of Al, Si, Mg, Mn, Fe in the AA6082. The welded region confirms the presence of Al, Mg, Mn, Fe which confirms the mixing of the parent material in the welded region.

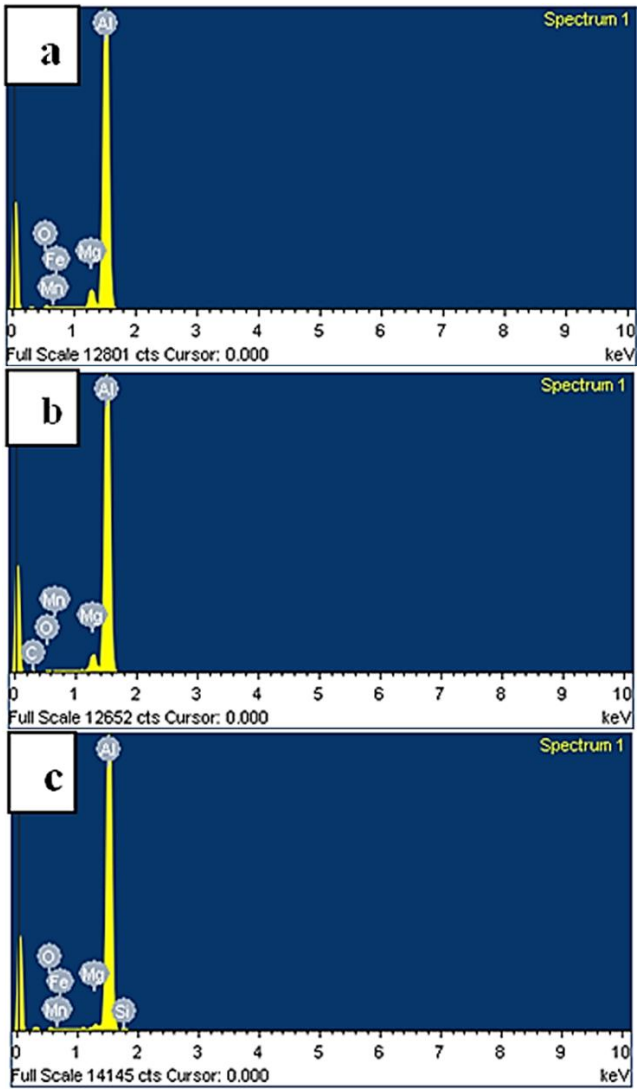

Figure 4.10 EDX microanalysis of (a) AA5083 (b) welded region of FSTWB (c) AA6082

The presence of metallic compounds has been confirmed by the spectrum obtained by XRD analysis. The analysis shows the presence of $Al_{12}Mg_{17}$, Al, Al_3Mg_2, Mg_2Si, Al_6Mn, AlFe, and AlNi in the non-annealed welded region of the FSTWB as shown in Figure 4.11 (a) and (b), respectively.

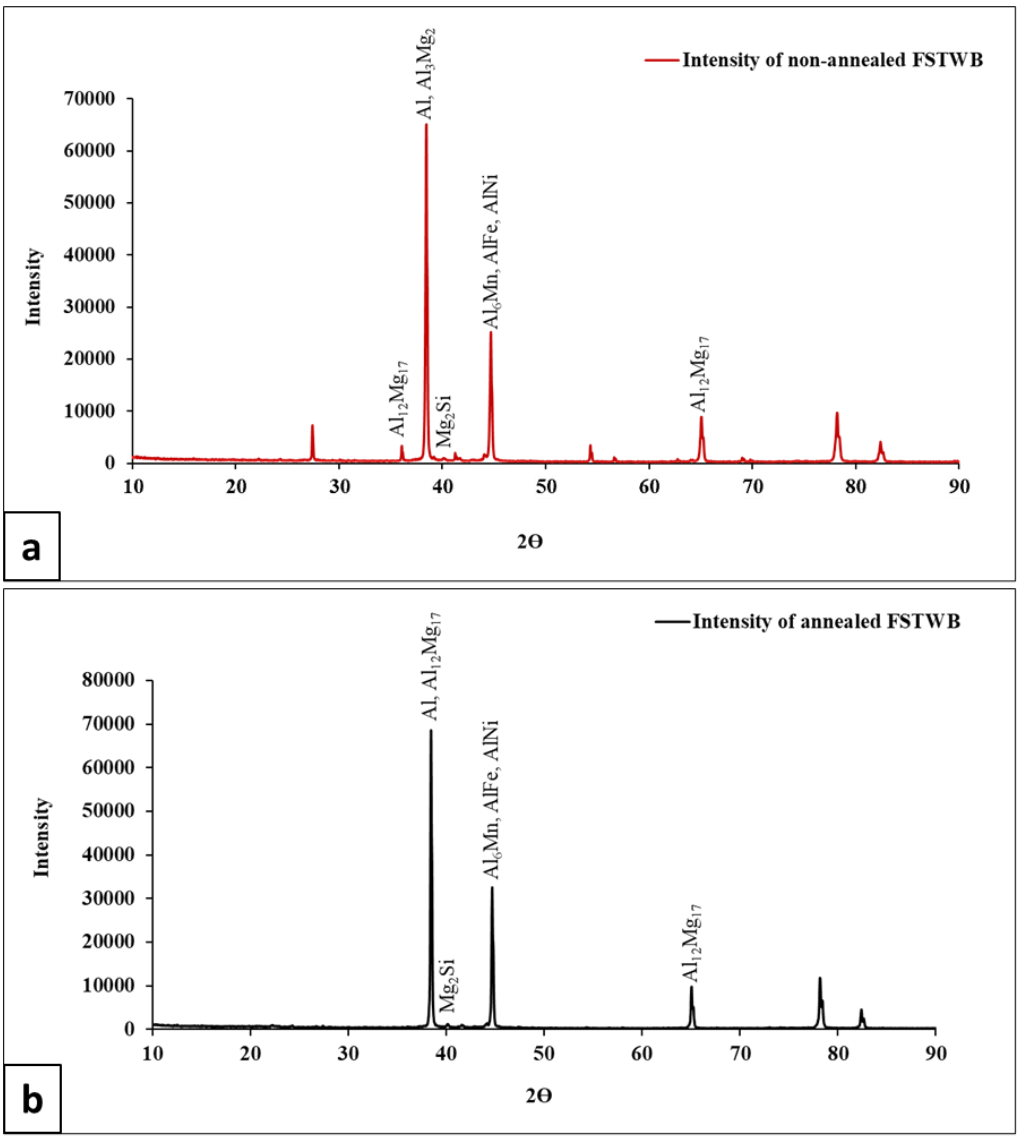

Figure 4.11 XRD pattern of a non-annealed and annealed FSTWB

4.8 Formability of FSTWB

Both major and minor strains data obtained from the experiments are assessed in the safe, necked, and failure regions, and the forming limit diagram (FLD) is constructed such that strains at necking or fracture are positioned at or above the line and are shown in Figure 4.12. The recorded limit stresses are probably the maximum safe strains for these materials, and the dome height at failure may be marginally less than the true limiting dome height. The punch stroke at which necking or a fracture in the sheet initiates is referred to as the stretch height.

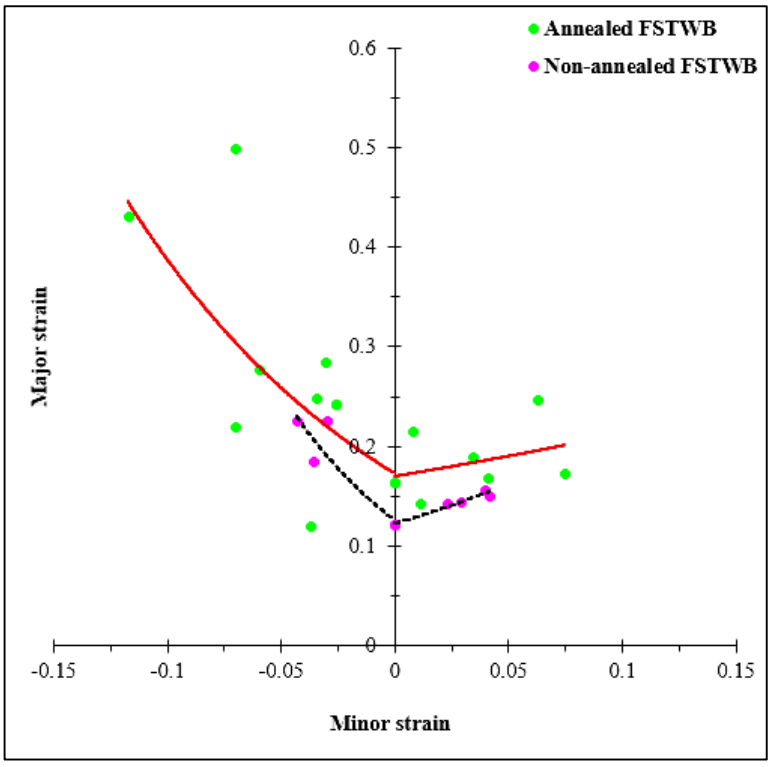

Figure 4.12 Combined forming limit diagram of FSTWB non-annealed and annealed sheet

The Table 4.9 gives the experimental and predicted values of dome heights of specimens with different widths resulting from punch stretching for both annealed and non-annealed FSTWBs. The percentage error between the experimental and FEA data

is determined and is also presented in the Table. The annealed specimen, measuring 60 mm in width, demonstrates a minimal dome height of 18.30 mm, conforming to the FLD_0 under plane strain conditions, with major and minor strains of 0.17 and 0.02, respectively.

Table 4.9 Comparison of dome heights obtained by experiments and simulations

Width (mm)	Dome heights in FSW Annealed			Dome heights in FSW Non-Annealed		
	Experiment (mm)	FEA (mm)	% Error	Experiment (mm)	FEA (mm)	% Error
20	21.90±0.44	22.19	1.32	21.16±0.17	21.03	0.61
30	21.74±0.08	21.76	0.10	20.57±0.35	20.17	1.94
40	21.43±0.15	20.33	5.13	20.44±0.22	18.13	11.30
50	20.68±0.32	18.30	11.50	18.00±0.17	16.32	9.33
60	18.28±0.45	15.80	13.56	15.88±0.32	14.35	9.63
70	19.32±0.09	17.50	9.42	17.45±0.28	14.98	14.15
80	18.00±0.30	17.74	1.44	15.50±0.10	15.53	0.19
100	20.04±0.17	19.72	1.59	17.57±0.03	17.50	0.39

For the non-annealed samples, a width of 60mm demonstrates a dome height of 15.88mm, with associated major and minor strains of 0.12 and 0.018, respectively. Consequently, in both instances, FLD_0 is observed to be positioned to the right of the

plane strain condition. The deformed sample displays positive major and minor stresses, signifying a biaxial stretching (tension-tension) condition that may have led to reduced dome heights in both experiment and the prediction. The predicted results for dome heights demonstrate an agreement with the experimental findings except a few case. The formability of the annealed samples is superior to that of non-annealed samples, which may be attributed to greater ductility, strain hardening exponent and decreased hardness in the former. Overall, the FEA findings match well with experimental observations, especially at lower and greater widths, where the percentage error is negligible. For FSW annealed samples, relatively modest errors are detected at widths of 20, 30, 80, and 100 mm, whereas significant deviations occur at intermediate widths, indicating that formability is more sensitive to width and material condition.

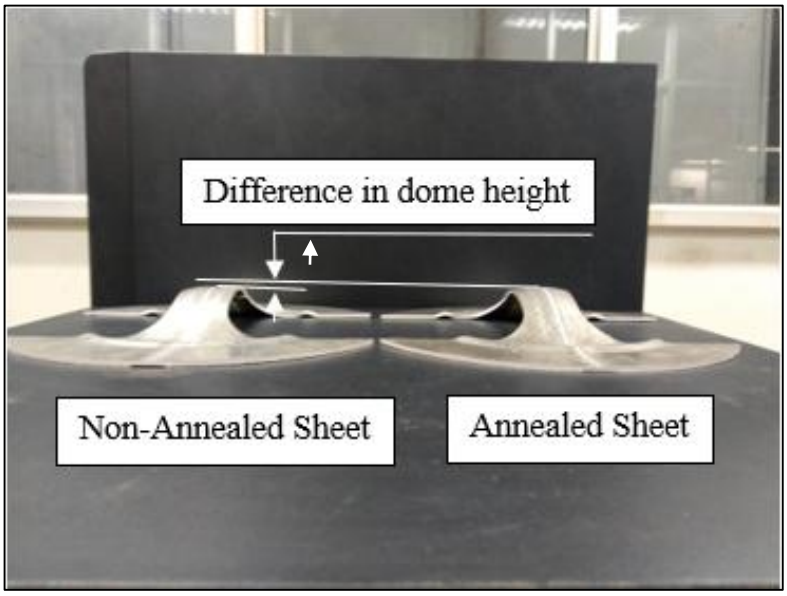

Figure 4.13 FSTWB samples after forming operation

The results for the experimental dome heights are shown in Figure 4.13. It demonstrates that the annealed samples of FSTWB has a higher dome height than a non-annealed sample. Due to the annealing, atomic mobility within the matrix of the alloy increases, allowing the rearrangement of dislocations and reduction of locked-in stresses. This further reduces the residual stresses by promoting stress relaxation through recovery, recrystallization, and grain growth. Furthermore, the annealing homogenizes the variation in residual stresses across the weld zone and parent materials, reducing stress concentration and ensuring more uniform mechanical behaviour. Annealing is also observed to enhance ductility by recrystallizing the weld zone and parent materials, replacing strained grains with equiaxed ones. The resulted grain refinement improves the uniform distribution of stress during forming preventing the localized thinning or fracture during forming. Also, annealing ensures the weld zone and parent materials deform cohesively during forming, reducing the risk of cracking or necking enhancing the formability.

The variation in stress distribution for both non-annealed and annealed samples across the width along a specified nodal path (20mm width) obtained from the simulations are illustrated in Figure 4.14 (a)-(b) and 4.15 (a)-(b), respectively. In the case of a non-annealed sheet exhibiting predominantly tensile deformation during LDH simulation, the von-Mises stress in the parent sheet reaches 300 MPa (in AA5083) and subsequently drops sharply to 200 MPa in the contiguous welded region, maintaining a near-constant value throughout the welded area until it transitions to the other parent material (AA6082), where it is observed to decrease slightly to 160 MPa. In the case of an annealed specimen, the stress value decreases to 251 MPa in the parent sheet (AA5083) and further drops sharply to 149 MPa in the welded zone, remaining contant

throughout the weld zone. Post-annealing, the stress values of the welded region and AA6082 are nearly identical, indicating that the FSTWB can accommodate greater deformation at reduced loads.

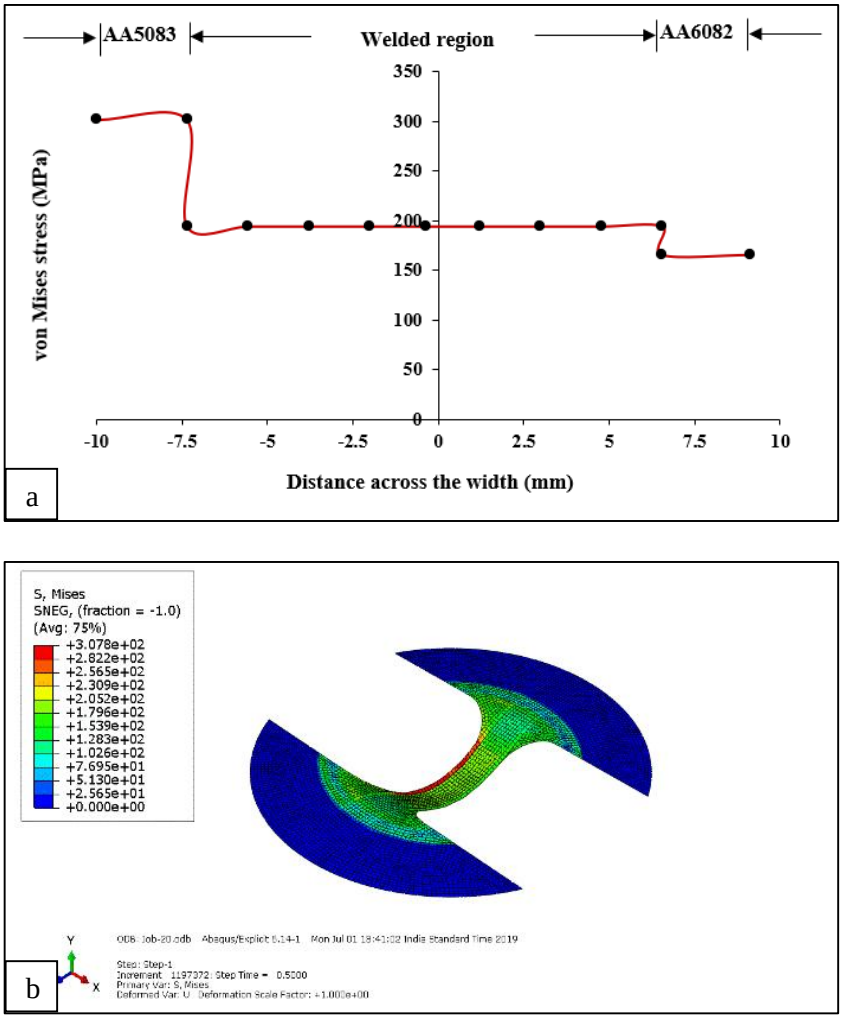

Figure 4.14 (a) Variation of von-Mises stress at different points across the width, (b) Contours of formed sheet for a punch profile radius of 20mm (non-annealed)

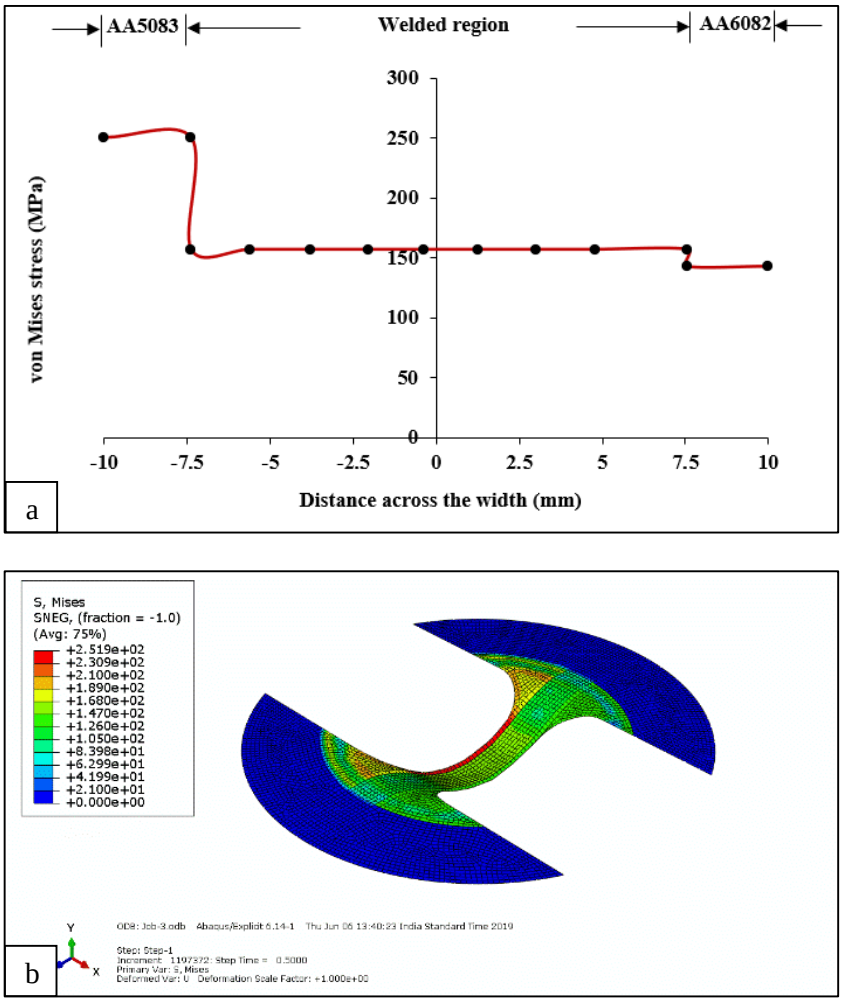

Figure 4.15 (a) Variation of von-Mises stress at different points across the width, (b) Contours of formed sheet for a punch profile radius of 20mm (annealed)

The stress distribution for 60mm width of the specimen which experiences minimum dome height in both the cases for non-annealed and annealed (near to a plane strain deformation) is minimum 150MPa and steadily rises to a maximum of 250MPa in AA5083 portion of TWB as shown in Figure 4.16 (a)-(b) and 4.17 (a)-(b), respectively. The stress abruptly drops to 200MPa for non-annealed and 151MPa for annealed as the welded zone is reached and remains constant throughout the remaining width across AA6082.

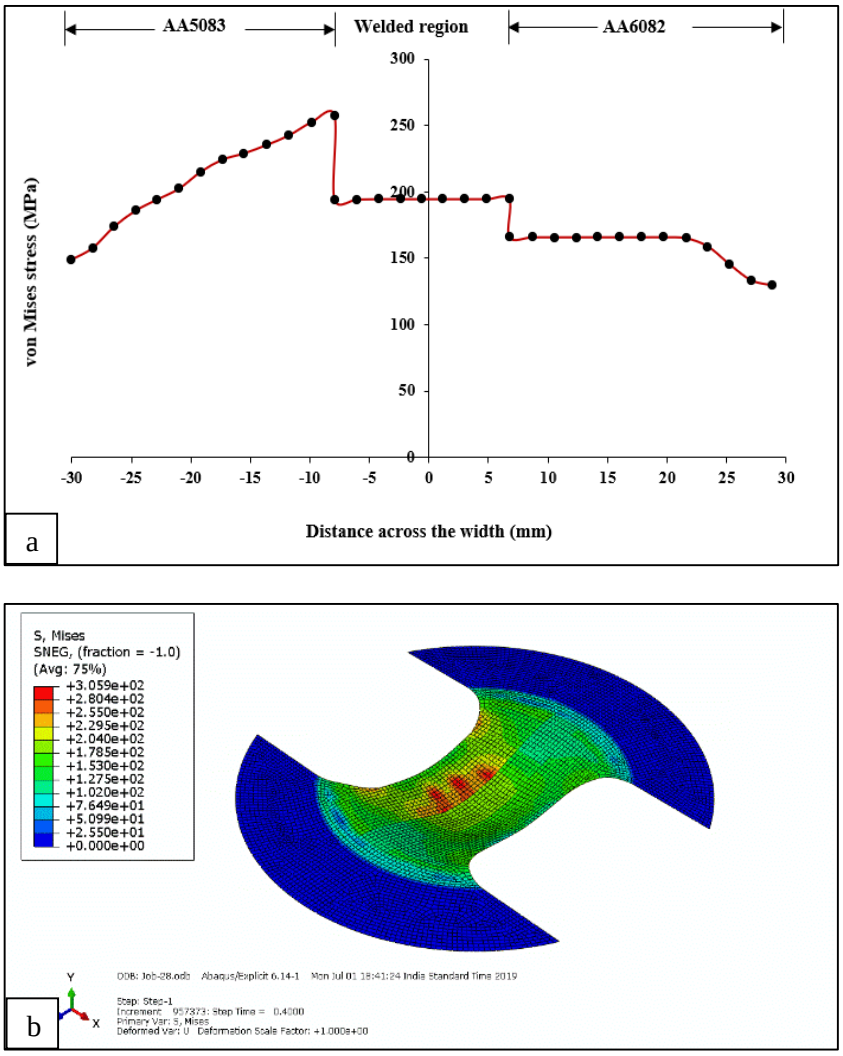

Figure 4.16 (a) Variation of von-Mises stress at different points across the width, (b) Contours of formed sheet for a punch profile radius of 60mm (non-annealed)

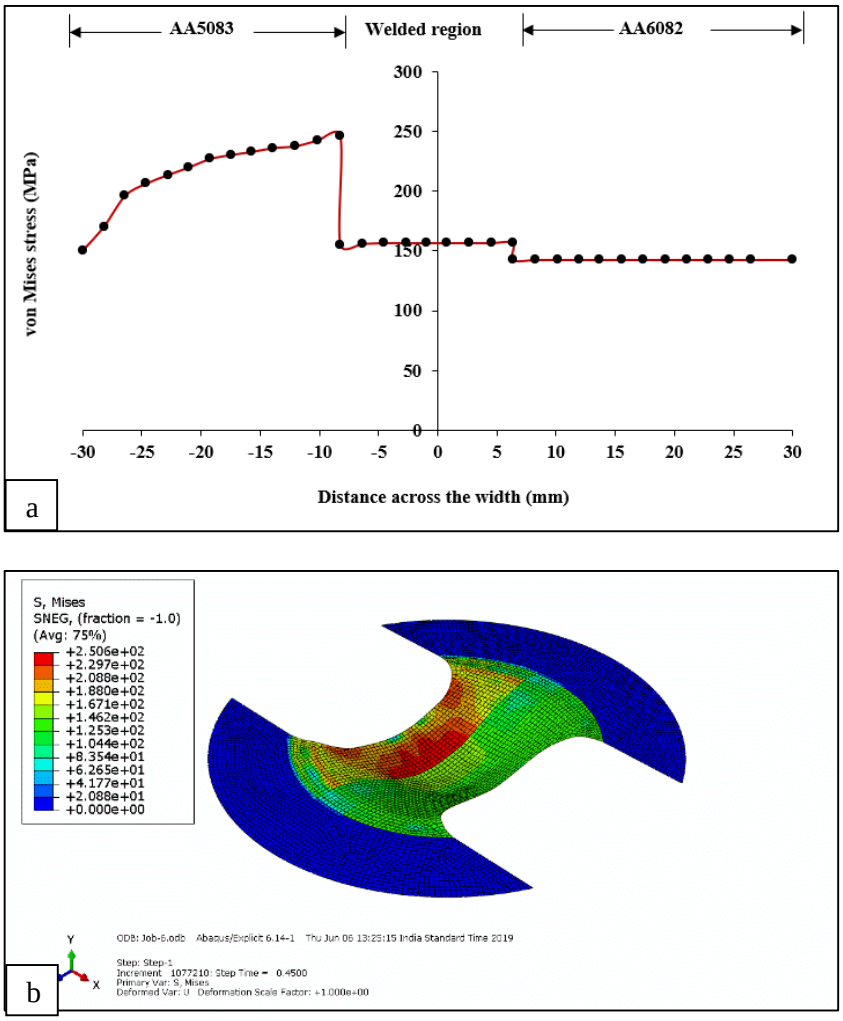

Figure 4.17 (a) Variation of von-Mises stress at different points across the width, (b) Contours of formed sheet for a punch profile radius of 60mm (annealed)

The variation in stress distribution for both non-annealed and annealed sheets across the width along a designated nodal path for (100mm of width) obtained by simulations are shown in Figure 4.18 (a)-(b) and 4.19 (a)-(b), respectively. In both the cases of simulations the mode of deformation is of drawing i.e. a combination of tesile and compressive stresses. In the case of a non-annealed sheet during LDH simulation, the von Mises stress value in the parent sheet steadily rises to approximately 300MPa (in AA5083) and the value drops sharply to 200MPa as the welded region starts and

remains almost constant across the welded region till the other parent material (AA6082) and then drops slightly to 160MPa. Whereas, in the case of an annealed, the stress value is observed to drop to 251MPa in the parent sheet (AA5083) and the value drops to 149MPa in the welded region and remains almost constant across the weld region.

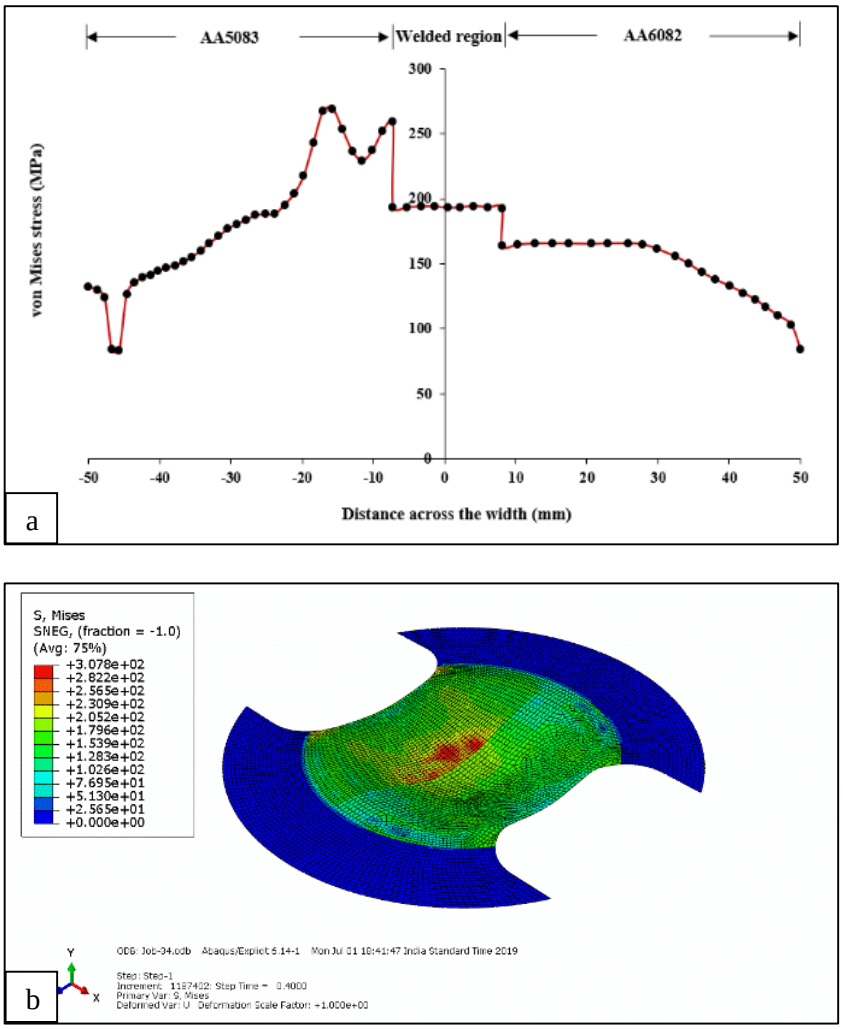

Figure 4.18 (a) Variation of von-Mises stress at different points across the width, (b) Contours of formed sheet for a punch profile radius of 100mm (non-annealed)

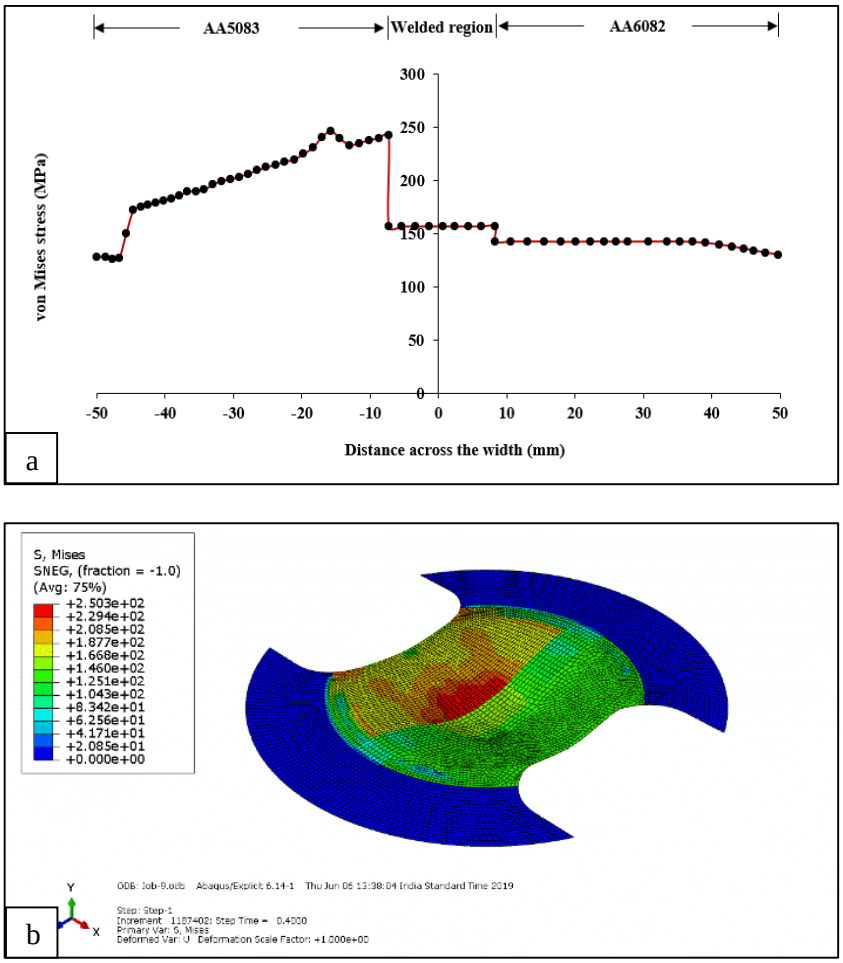

Figure 4.19 (a) Variation of von-Mises stress at different points across the width, (b) Contours of formed sheet for a punch profile radius of 100mm (annealed)

The following figure shows the Max. In-Plane Strain distribution for both non-annealed and annealed sheets across the width along a designated nodal path for (20mm of width) obtained by simulations are shown in Figure 4.20 (a)-(b) and 4.21 (a)-(b), respectively. In both the cases of simulations the mode of deformation is of drawing i.e. a combination of tesile and compressive stresses. In the case of a non-annealed sheet during LDH simulation, the Max. In-Plane Strain value in the parent sheet steadily rises to approximately 0.15 (in AA5083) and the value rises sharply to 0.24 as the welded region starts and shows a curve across the welded region till the

other parent material (AA6082) and then drops slightly to 0.21 and remians almost stable in the parent sheet (AA 6082). Whereas, in the case of an annealed, the strain value is observed to 0.17 in the parent sheet (AA5083) and and the value rises sharply to 0.25 as the welded region starts and shows a curve across the welded region till the other parent material (AA6082) and then drops slightly to 0.24 and re,ails almost stable in the parent sheet (AA6082).

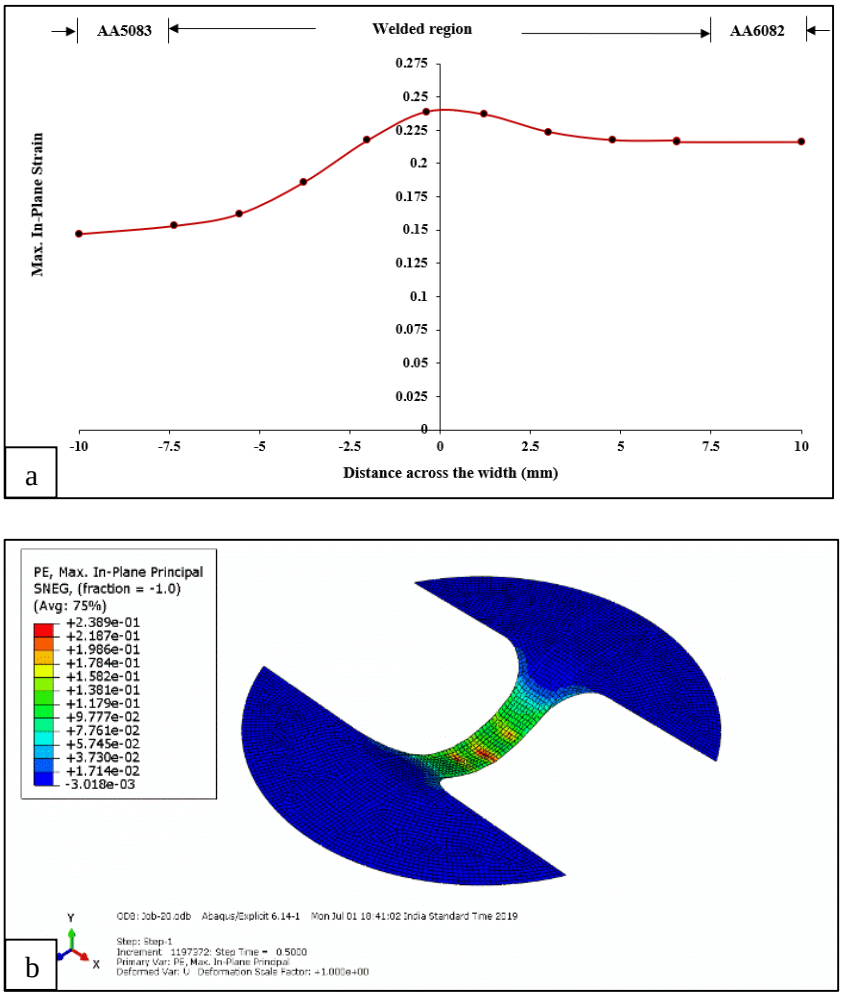

Figure 4.20 (a) Variation of Max. In-Plane Strain at different points across the width, (b) Contours of formed sheet for a punch profile radius of 20mm (non-annealed)

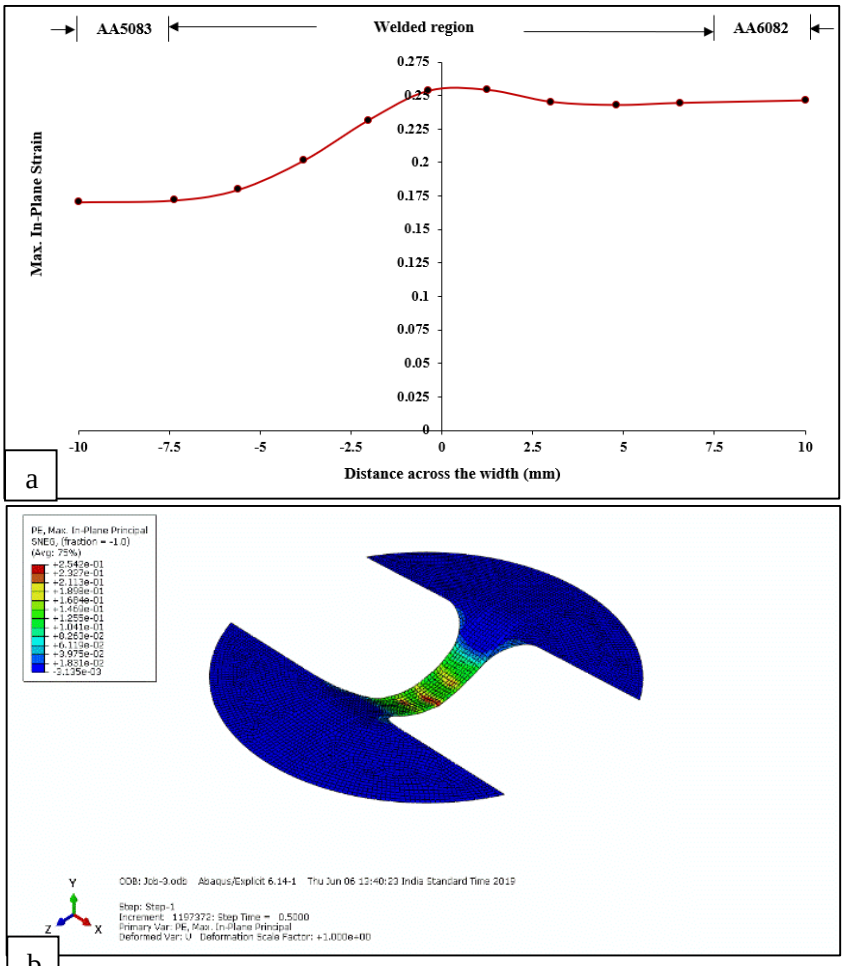

Figure 4.21 (a) Variation of Max. In-Plane Strain at different points across the width, (b) Contours of formed sheet for a punch profile radius of 20mm (annealed)

The following figure shows the Max. In-Plane Strain distribution for both non-annealed and annealed sheets across the width along a designated nodal path for (60mm of width) obtained by simulations are shown in Figure 4.22 (a)-(b) and 4.23 (a)-(b), respectively. In both the cases of simulations the mode of deformation is of drawing i.e. a combination of tesile and compressive stresses. In the case of a non-annealed sheet during LDH simulation, the Max. In-Plane Strain value in the parent sheet steadily rises to approximately 0.09 (in AA5083) and the value rises sharply to 0.19 as the welded region starts and shows a drops to 0.14 and again increases to 0.15

across the welded region till the other parent material (AA6082) and then increases to 0.13 and again it increases to 0.17 in the AA66082 region. Whereas, in the case of an annealed, the strain value is observed to 0.14 in the parent sheet (AA5083) and and the value rises sharply to 0.26 as the welded region starts and shows a curve across the welded region and drops to 0.22 and increases again to 0.23 till the other parent material (AA6082) and then increases to 0.25 in the AA6082 region.

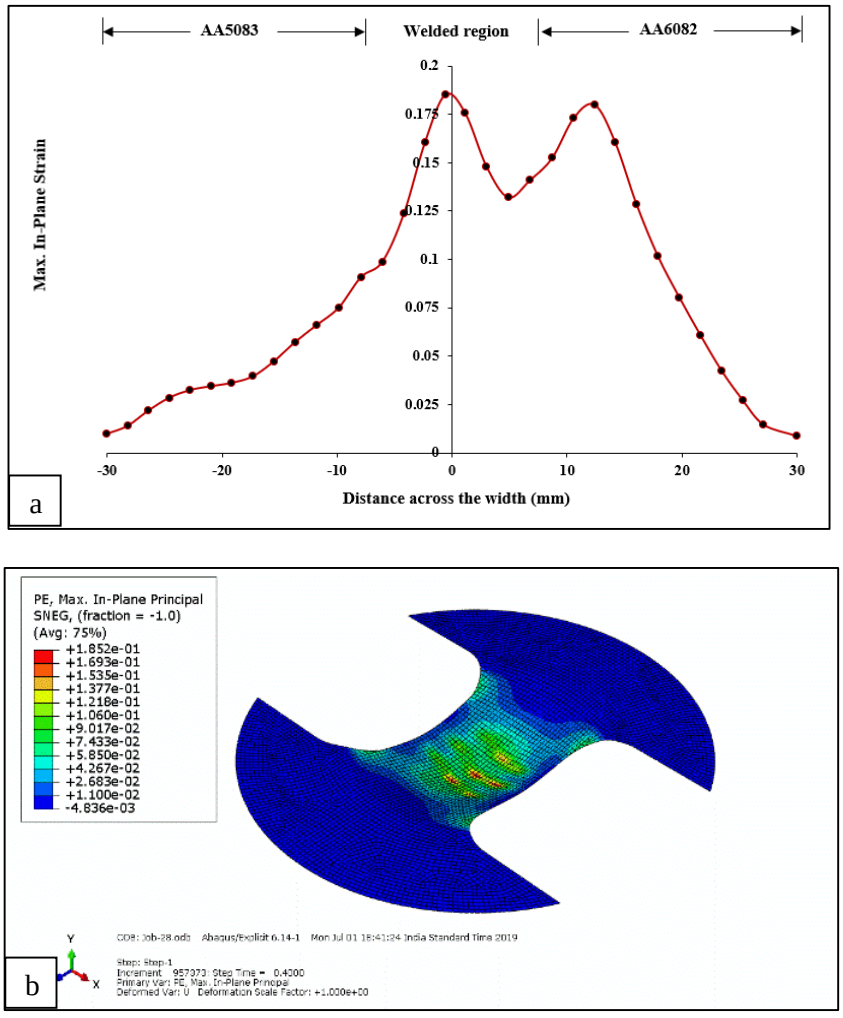

Figure 4.22 (a) Variation of Max. In-Plane Strain at different points across the width, (b) Contours of formed sheet for a punch profile radius of 60mm (non-annealed)

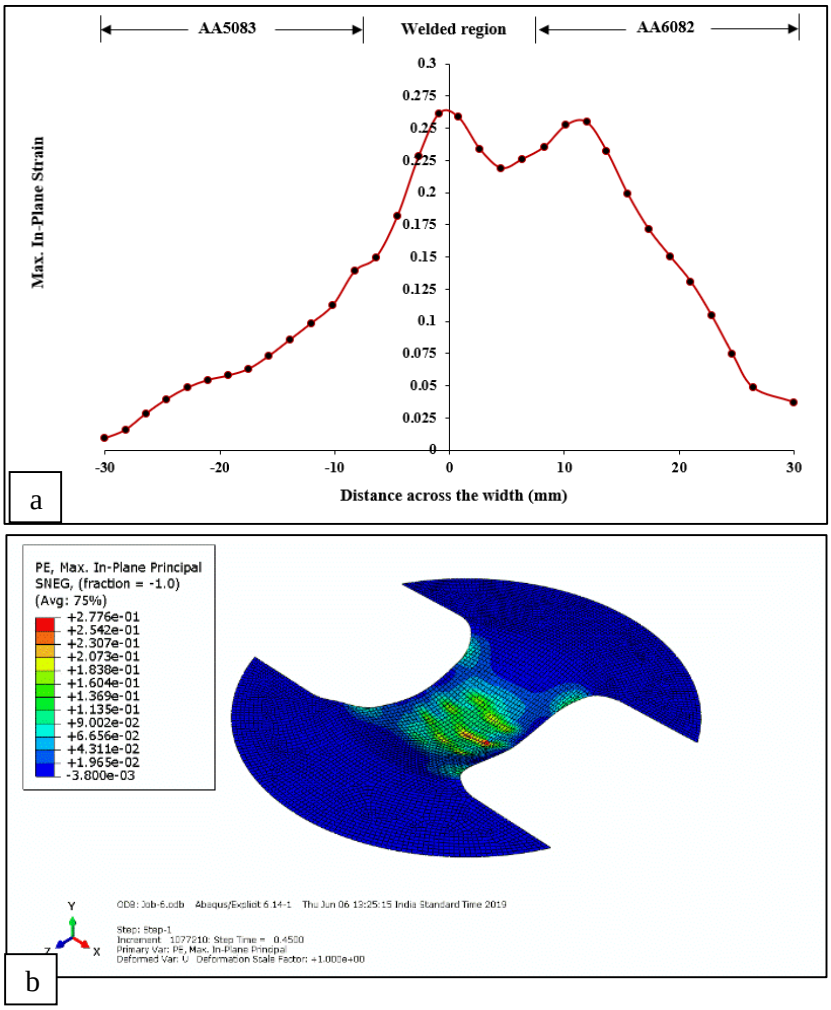

Figure 4.23 (a) Variation of Max. In-Plane Strain at different points across the width, (b) Contours of formed sheet for a punch profile radius of 60mm (annealed)

The following figure shows the Max. In-Plane Strain distribution for both non-annealed and annealed sheets across the width along a designated nodal path for (60mm of width) obtained by simulations are shown in 4.24 (a)-(b) and 4.25 (a)-(b), respectively. In both the cases of simulations the mode of deformation is of drawing i.e. a combination of tesile and compressive stresses. In the case of a non-annealed sheet during LDH simulation, the Max. In-Plane Strain value in the parent sheet steadily rises to approximately 0.08 (in AA5083) and the value rises sharply to 0.2 as the welded region starts and shows a curve across the welded region and drops to 0.15

and increases again 0.16 till the other parent material (AA6082) and then increases to 0.19 in the AA66082 region. Whereas, in the case of an annealed, the strain value is observed to 0.11 in the parent sheet (AA5083) and and the value rises sharply to 0.22 as the welded region starts and shows a curve across the welded region and drops to 0.2 and again increases to 0.22 till the other parent material (AA6082) and again rises to 0.27 in the AA6082 region.

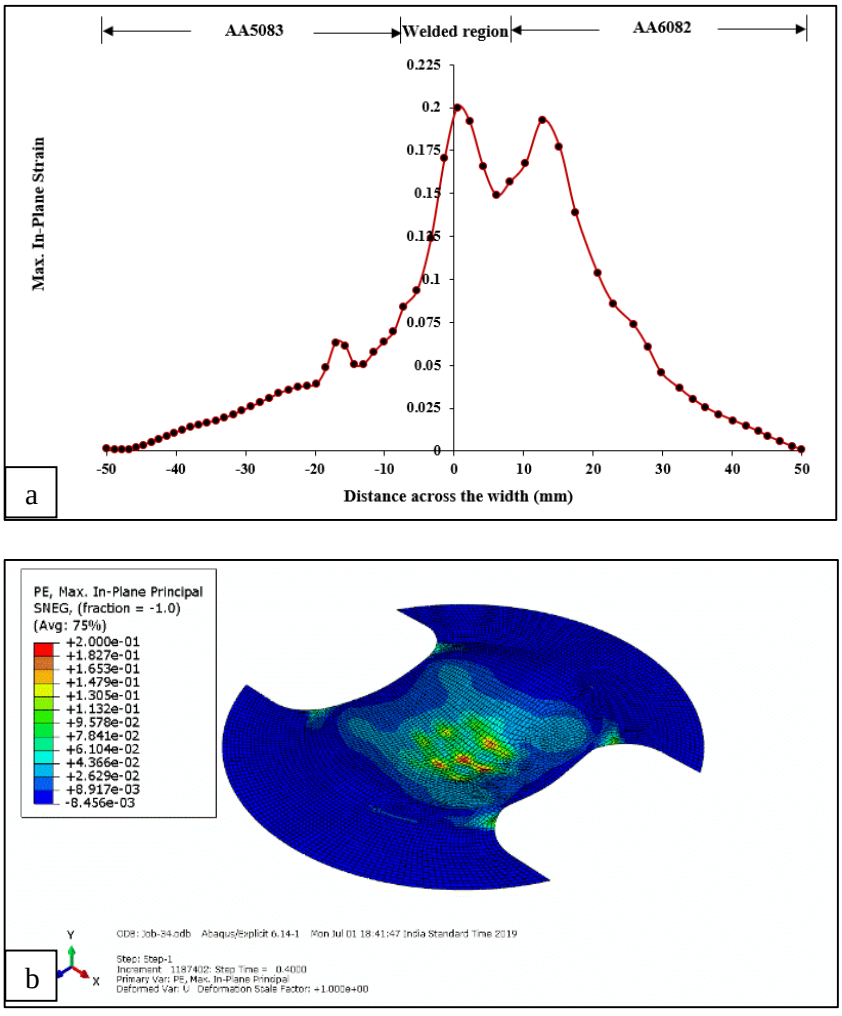

Figure 4.24 (a) Variation of Max. In-Plane Strain at different points across the width, (b) Contours of formed sheet for a punch profile radius of 100mm (non-annealed)

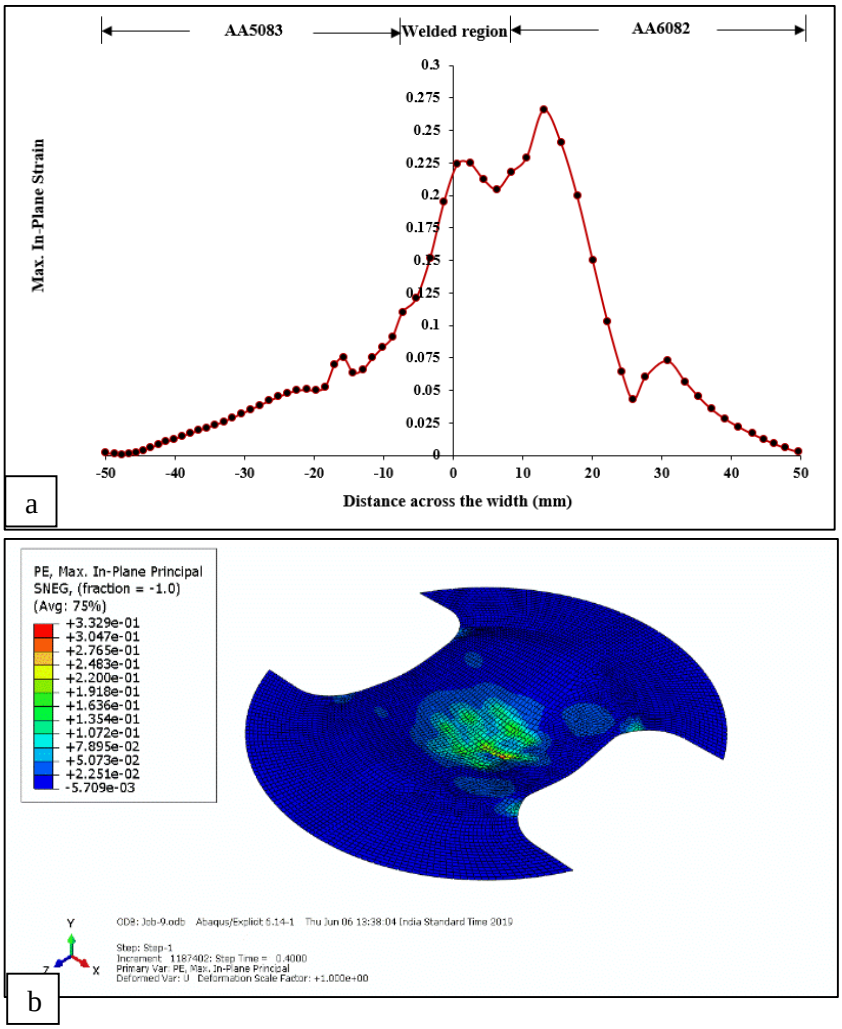

Figure 4.25 (a) Variation of Max. In-Plane Strain at different points across the width, (b) Contours of formed sheet for a punch profile radius of 100mm (annealed)

The following figure shows the Min. In-Plane Strain distribution for both non-annealed and annealed sheets across the width along a designated nodal path for (20mm of width) obtained by simulations are shown in 4.26 (a)-(b) and 4.27 (a)-(b), respectively. In both the cases of simulations the mode of deformation is of drawing i.e. a combination of tesile and compressive stresses. In the case of a non-annealed sheet during LDH simulation, the Min. In-Plane Strain value in the parent sheet steadily rises to approximately -0.07 (in AA5083) and the value rises sharply to 0.04 as the

welded region starts and shows a curve across the welded region and drops to -0.07 and increases again -0.06 till the other parent material (AA6082) and then remains constant in the AA66082 region. Whereas, in the case of an annealed, the strain value is observed to -0.08 in the parent sheet (AA5083) and and the value rises sharply to 0.02 as the welded region starts and shows a curve across the welded region and drops to -0.07 and again increases to -0.06 till the other parent material (AA6082) and remains constant in the AA6082 region.

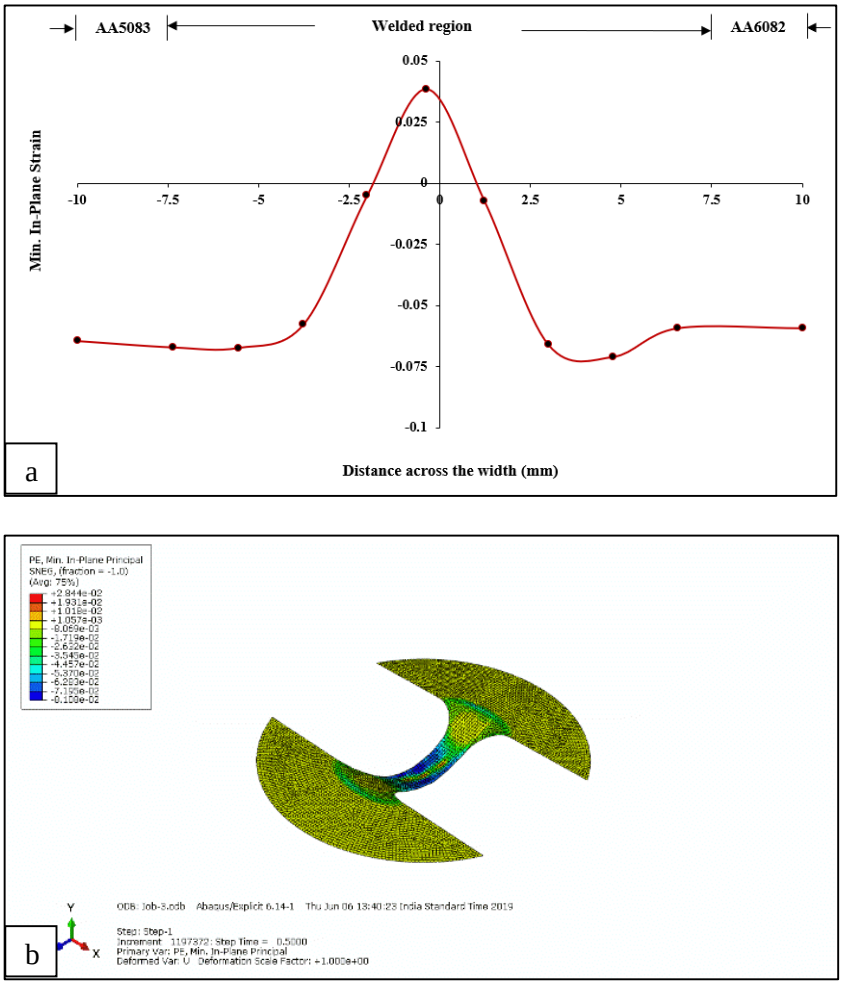

Figure 4.26 (a) Variation of Min. In-Plane Strain at different points across the width, (b) Contours of formed sheet for a punch profile radius of 100mm (non-annealed)

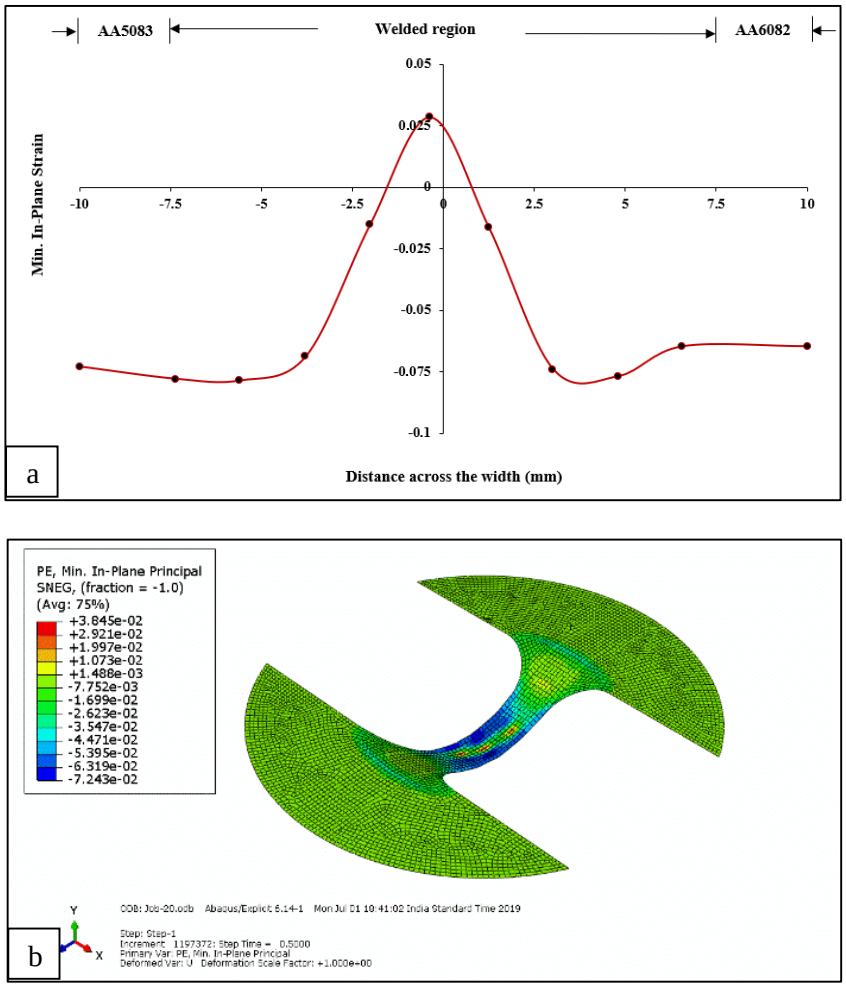

Figure 4.27 (a) Variation of Min. In-Plane Strain at different points across the width, (b) Contours of formed sheet for a punch profile radius of 100mm (annealed)

The following figure shows the Min. In-Plane Strain distribution for both non-annealed and annealed sheets across the width along a designated nodal path for (60mm of width) obtained by simulations are shown in 4.28 (a)-(b) and 4.29 (a)-(b), respectively. In both the cases of simulations the mode of deformation is of drawing i.e. a combination of tesile and compressive stresses. In the case of a non-annealed sheet during LDH simulation, the Min. In-Plane Strain value in the parent sheet steadily rises to approximately -0.02 (in AA5083) and the value rises sharply to 0.1 as the welded region starts and drops to -0.02 till the other parent material (AA6082) and then shows

a peak at 0.06 and again a drop to -0.06 then remains gradually increasing in the AA66082 region. Whereas, in the case of an annealed, the strain value is observed to -0.01 in the parent sheet (AA5083) and and the value rises sharply to 0.13 as the welded region starts and shows a curve across the welded region and drops to -0.03 and again increases to 0.06 till the other parent material (AA6082) and remains constant in the AA6082 region.

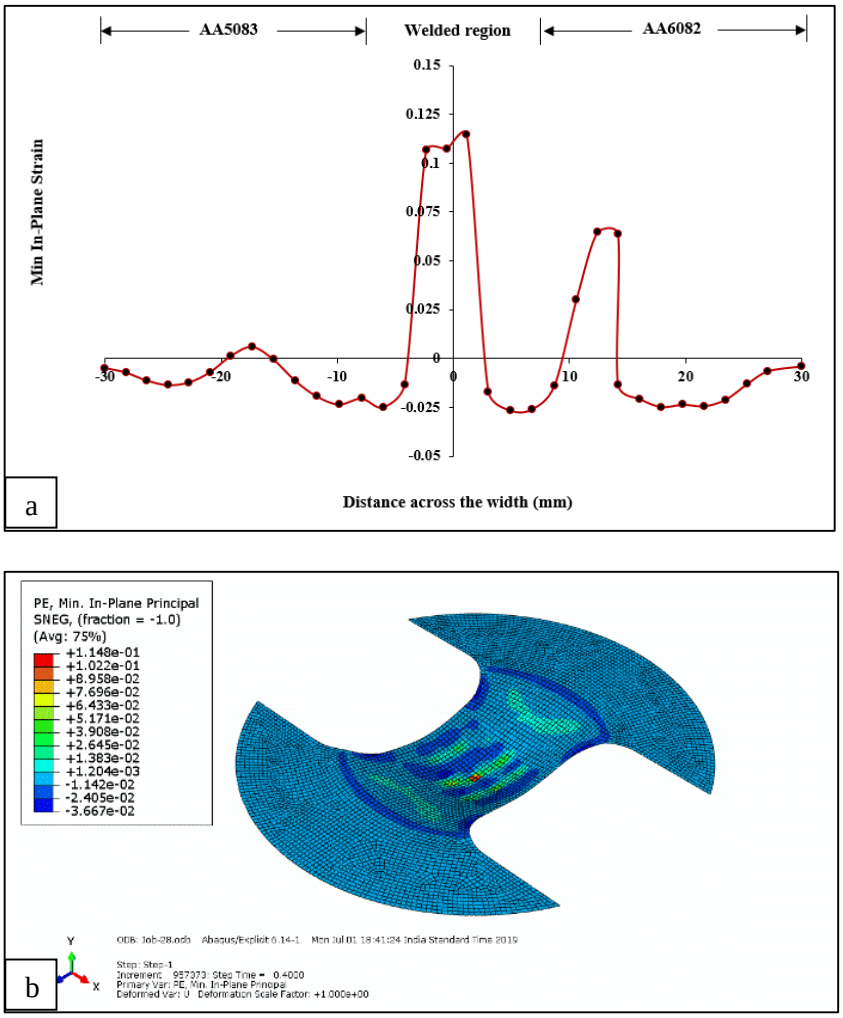

Figure 4.28 (a) Variation of Min. In-Plane Strain at different points across the width, (b) Contours of formed sheet for a punch profile radius of 100mm (non-annealed)

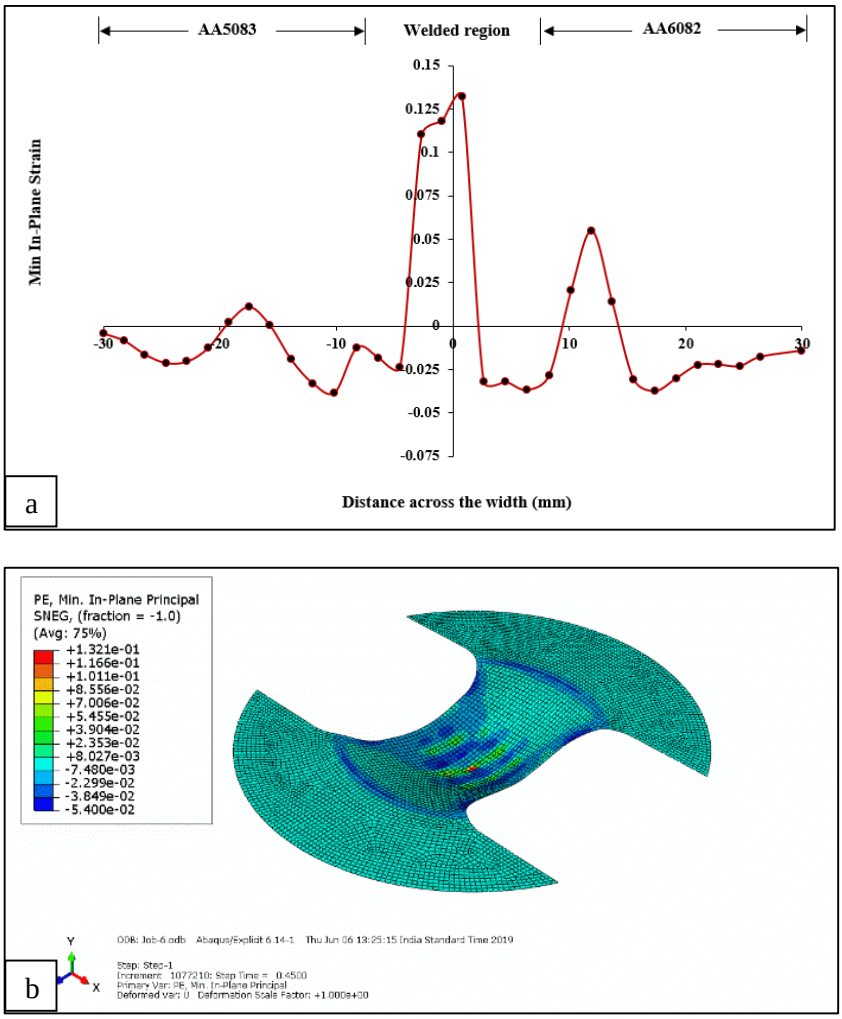

Figure 4.29 (a) Variation of Min. In-Plane Strain at different points across the width, (b) Contours of formed sheet for a punch profile radius of 100mm (annealed)

The following figure shows the Min. In-Plane Strain distribution for both non-annealed and annealed sheets across the width along a designated nodal path for (60mm of width) obtained by simulations are shown in 4.30 (a)-(b) and 4.31 (a)-(b), respectively. In both the cases of simulations the mode of deformation is of drawing i.e. a combination of tesile and compressive stresses. In the case of a non-annealed sheet during LDH simulation, the Min. In-Plane Strain value in the parent sheet steadily rises to approximately 0.03 (in AA5083) and the value rises sharply falls to 0.01 and again

rises to 0.16 as the welded region starts and drops to 0.002 and rises to 0.03 till the other parent material (AA6082) and then shows a peak at 0.06 and again a drop to –0.003 then remains gradually increasing in the AA66082 region. Whereas, in the case of an annealed, the strain value is observed to 0.07 in the parent sheet (AA5083) then takes a drop at 0.03 and the value rises sharply to 0.18 as the welded region starts and shows a curve across the welded region and drops to 0.02 and again increases to 0.1 till the other parent material (AA6082) and drops to -0.05 and slightly increases in the AA6082 region.

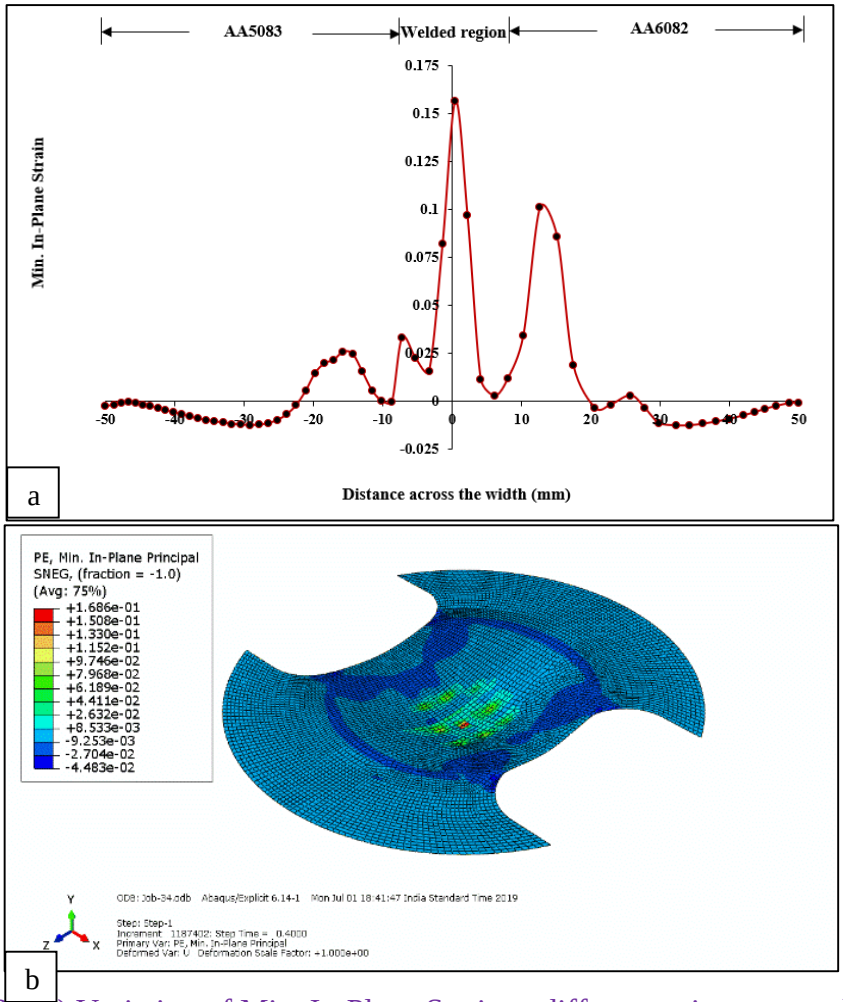

Figure 4.30 (a) Variation of Min. In-Plane Strain at different points across the width, (b) Contours of formed sheet for a punch profile radius of 100mm (non-annealed)

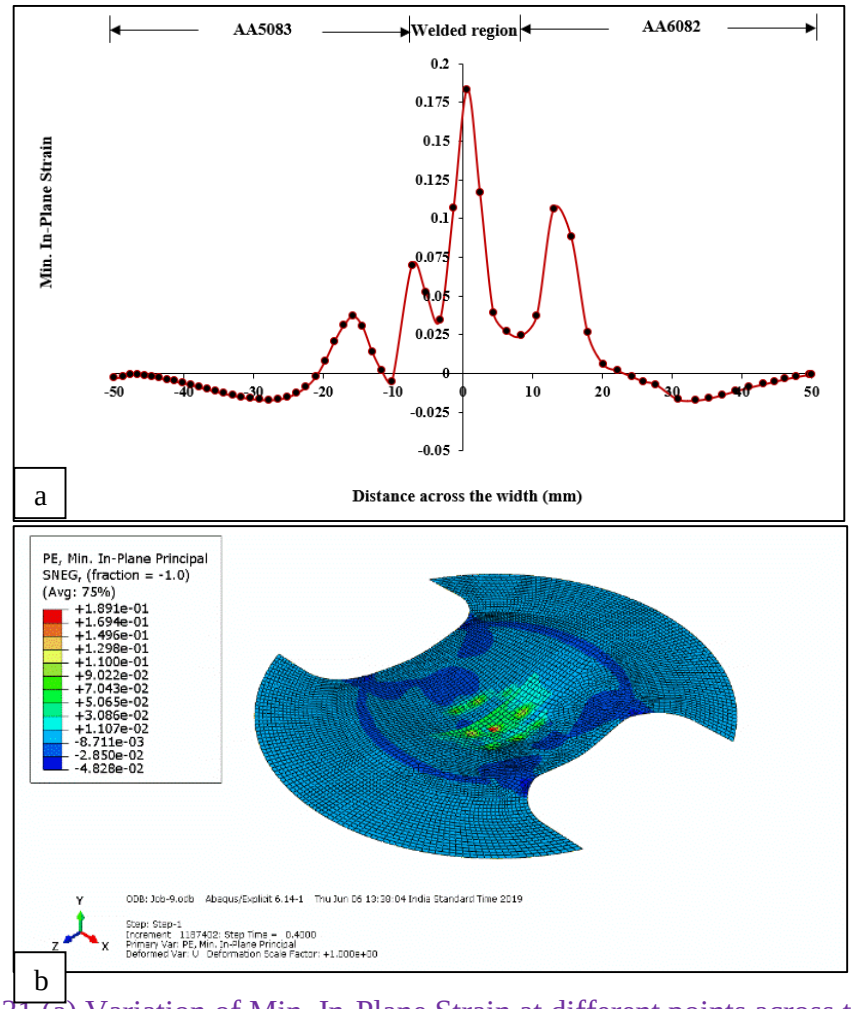

Figure 4.31 (a) Variation of Min. In-Plane Strain at different points across the width, (b) Contours of formed sheet for a punch profile radius of 100mm (annealed)

FEA representation shows that failure initiates from the right-hand side of the sheet (Side in the positive "X" axis direction.). As right-hand side of the sheet contains AA6082, a softer material, prediction of failure initiation worked properly. Max. In-Plane Principal Strain-Distance across sheet shows that maximum strain occurs at the centre position of the sheet below the punch.

The comparison in variation of thickness across the width of the specimens for 20mm, 60mm and 100mm in both the cases of annealed and non-annealed, obtained by LDH simulation are shown in Figure 4.32. In the case of 20mm width, it is observed that the

minimum thickness reduces to 1.76mm from 1.84mm after annealing which indicates the softening of the material and resulting in a higher dome height in this mode of deformation. The necking occurs in the middle of welded region as the mode of deformation is majorly tensile.

The thickness variation in the cases of 60mm width specimens in the plane strain condition obtained by LDH simulation is shown in Figure 4.33, and it is observed that the minimum thickness at which necking occurs is 1.82mm which reduces to 1.76mm after annealing. In both the cases of annealed and non-annealed, the necking occurs at the interface of welded region and parent sheet of AA6082. In both the cases, the dome height is the minimum when compared to LDH deformation of other widths of the specimens.

The variation of thickness across a width of 100mm, obtained by simulations for annealed and non-annealed specimens is shown in Figure 4.34. The minimum thickness at which necking occurs is 1.76mm which further reduces to 1.66mm after annealing. In both the cases, the necking occurs at the interface of welded region and AA6082 and also the thinning pattern remains the same.

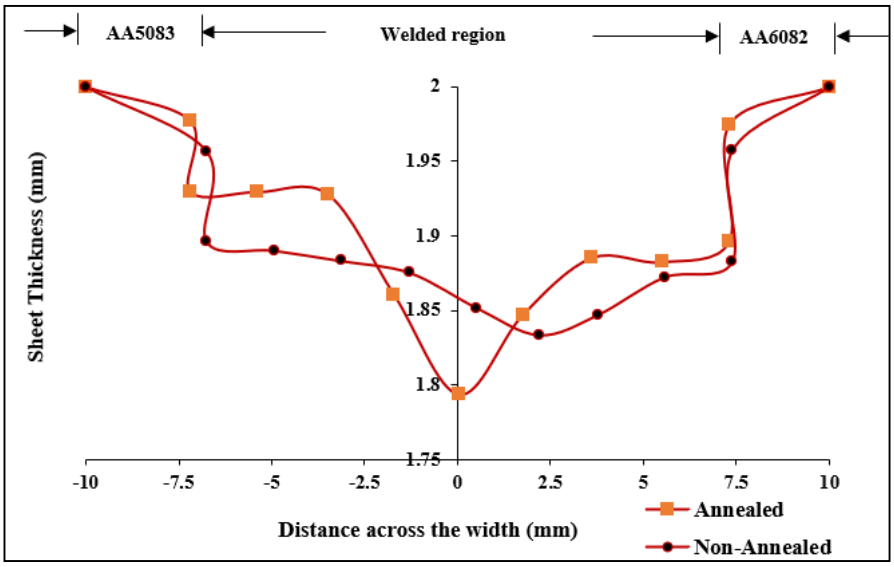

Figure 4.32 Variation of thickness across the width of 20mm in cases of annealed and non- annealed

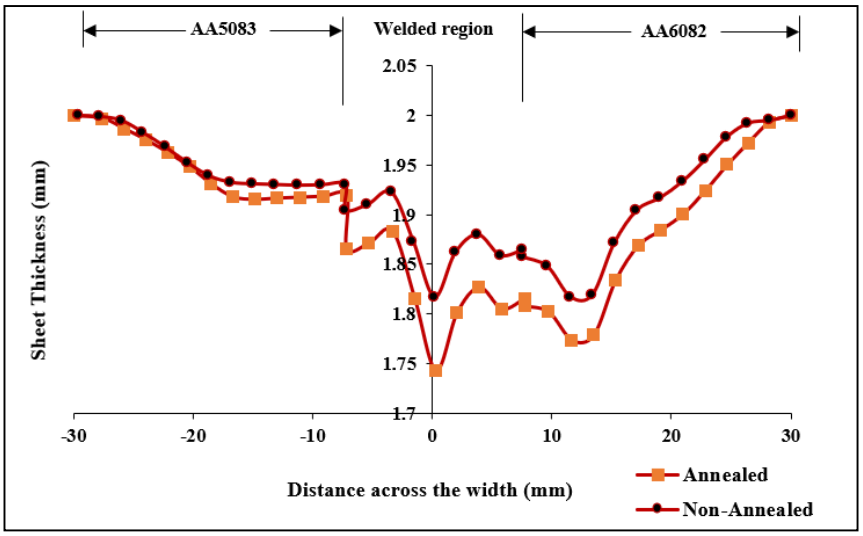

Figure 4.33 Variation of thickness across the width of 60mm in cases of annealed and non- annealed

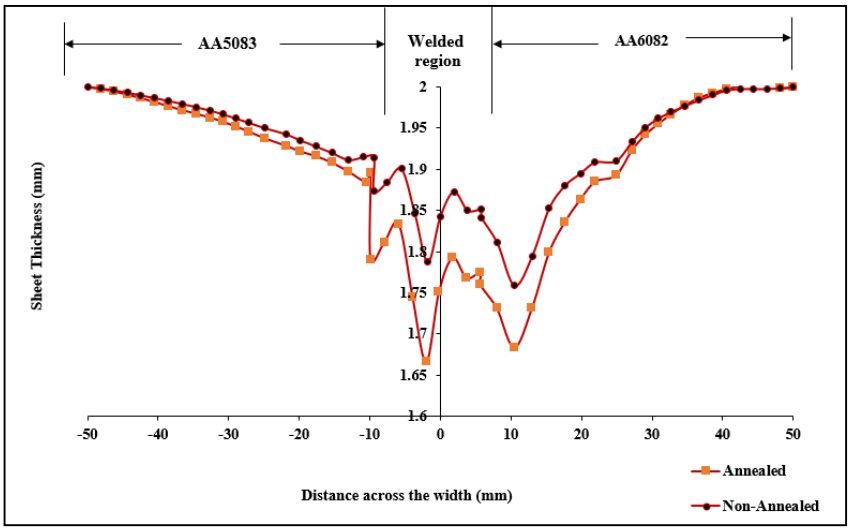

Figure 4.34 Variation of thickness across the width of 100mm in cases of annealed and non- annealed

CHAPTER 5

CONCLUSIONS

The present study is based on the experimental and numerical investigations on the formability of TWBs prepared by friction stir welding process. It is also attempted to enhance the formability of the prepared blanks by annealing operation. The conclusions which can be drawn from the study are as below:

1. It is observed that the yield and tensile strengths on an average basis for AA5083 are observed to be 204MPa and 261MPa, respectively. A value of 14% elongation and strain hardening exponent of 0.21 indicates moderate formability for this alloy.
2. In annealed state, AA6082-O possesses a yield strength of 86MPa and a tensile strength of 138MPa on an average basis indicating it as a softer material than AA5083. A higher value of ductility and strain hardening exponent renders this material to possess a higher formability when compared to AA5083.
3. In order to get the optimum mechanical properties obtained by Taguchi and ANOVA techniques, the welding was done at 800 rotational speed and traversing speed of 30 mm/min for all the TWB specimens. The results were verified by conducting weld integrity tests in uniaxial tensile experiments.
4. Annealing of the welded sheets at 150ºC results in decreased strength, increased ductility, and a strain hardening exponent. Increasing the annealing temperature to 300 ºC enhances tensile characteristics. At 350 ºC, the material exhibits reduced strength but increased ductility. Additionally, the strain hardening exponent is higher at 0.28. At 400 ºC, characteristics like as tensile

strength and strain hardening exponent decrease, indicating less stretching and consistent elongation. An annealing temperature of 350 ºC provides optimal tensile characteristics for higher formability, making it the preferred temperature for characterizing formability.

5. The value of hardness remains almost constant till 150°C and drops significantly at 300°C owing to the softening of the material. The drop in the hardness values becomes more significant at higher temperatures of 350°C and then stabilizes at 400°C. The variation in the hardness of AA6082, AA 5083 and weld bead regions at different temperatures are observed to be similar due to diffusion and dissolution of hardening precipitates in the stir zone.
6. It is observed that the residual stress is compressive in nature in both the cases of top and bottom sides of the FSTWB specimens, although the distribution pattern is seen to follow an increasing and decreasing trend of stress across the weld zone. The residual stress has been reduced significantly by annealing and also the resultant variation of residual stress is more or less uniform in both welded region and parent sheets after the annealing. Before annealing, a highest value of average hardness is observed in the AA5083 parent sheet followed by the hardness in the weld region and lowest in AA6082 parent sheet. The hardness values are also reduced after annealing. An annealing temperature of 350ºC gives the best combination of properties required for higher formability.
7. The bottom surface of FSTWB appears much smoother as the tool did not dig till the bottom surface which may be attributed to the design of the tool tip. It

is observed that the RS across the weld region from parent material AA5083, is compressive in nature and increases gradually towards the weld centre.

8. The micro-voids appeared in the AA5083 are comparatively smaller in size which indicates lower ductility and higher strength. A majority of the micro-voids are observed to have closed surfaces. In the case of the fracture surface of the weld zone, a mix of very fine and coarse micro-voids are observed indicating a reduction in strength but a slight improvement in ductility after annealing.
9. It is o observed in the fracture surfaces of parent AA6062 specimens, the depth and size of dimples appear to have increased which indicates larger deformation prior to failure. The fracture surface shows a combination of elongated and bigger micro-voids when compared to other micrographs. In almost all the cases the failure seems to have occurred due to nucleation and growth of micro-voids at or near inclusions/second phase particles which are found at many locations near the cavities in the fractured areas.
10. In the case of FSTWB specimens, XRD confirms the presence of $Al_{12}Mg_{17,}$ Al, Mg_2Si, Al_6Mn, AlFe, and AlNi are evident in the welded region indicating a thorough mixture of elements in both alloys by friction stir procedure. The fracture surface shows a combination of elongated and bigger micro-voids. In almost all the cases the failure seems to have occurred due to nucleation and growth of micro-voids at or near inclusions/second phase particles which are found at many locations near the cavities in the fractured areas.
11. The annealed sample with a width of 60 mm exhibits a minimal dome height of 18.28 mm, or the FLD_0 in plane strain condition, with corresponding major

and minor strains of 0.17 and 0.02, respectively. In the case of non-annealed samples, for the same width it exhibits a dome height of 15.88mm with corresponding major and minor strains of 0.12 and 0.018 indicating an enhanced formability after annealing. The results obtained by simulations agrees well with the experimental results. The annealing is observed to enhance the formability of the FSTWB by 13% in plane strain condition and equibiaxial stretch.

12. Overall, the FEA findings match well with experimental observations, especially at lower and greater widths, where the %age error is negligible. For FSW annealed samples, relatively modest errors are detected at widths of 20, 30, 80, and 100 mm, whereas significant deviations occur at intermediate widths, indicating that formability is more sensitive to width and material condition.
13. In the case of FSW non-annealed TWBs, predicted dome heights roughly match experimental results at smaller widths, but greater differences arise at mid-range widths due to lower ductility and strain localization. These results show that the FEA model can reasonably anticipate formability trends, as well as the effect of annealing on dome height and overall forming behaviour.
14. In the case of plane strain condition, the stress distribution for 60mm width of the specimen which experiences minimum dome height in both the cases for non-annealed and annealed is minimum 150MPa and steadily rises to a maximum of 250MPa in AA5083 portion of TWB. But the von-Mises stress drops to 200MPa for non-annealed and 151MPa for annealed as the welded

zone is reached and remains constant throughout the remaining width across AA6082.

15. In all the cases of limiting dome height results obtained by experiments and simulations, the necking occurs at the interface of welded region and AA6082 and also the thinning pattern remains the same.

REFERENCES

[1] Gautam, V., Raut, V. M., and Kumar, D. R., 2018, "Analytical prediction of springback in bending of tailor-welded blanks incorporating effect of anisotropy and weld zone properties," Proceedings of the Institution of Mechanical Engineers, Part L: Journal of Materials: Design and Applications, 232(4), pp. 294-306.

[2] Wallentowitz, H., Leyers, J., and Parr, T., 2003, "Materials for future automotive body structures," Business Briefing: Global Automotive Manufacturing & Technology, pp. 1-4.

[3] Habibi, M., Hashemi, R., Tafti, M. F., and Assempour, A., 2018, "Experimental investigation of mechanical properties, formability and forming limit diagrams for tailor-welded blanks produced by friction stir welding," Journal of Manufacturing Processes, 31, pp. 310-323.

[4] Kesharwani, R., Panda, S., and Pal, S., 2015, "Experimental investigations on formability of aluminum tailor friction stir welded blanks in deep drawing process," Journal of Materials Engineering and Performance, 24, pp. 1038-1049.

[5] Sadoun, A., Meselhy, A., and Deabs, A., 2020, "Improved strength and ductility of friction stir tailor-welded blanks of base metal AA2024 reinforced with interlayer strip of AA7075," Results in Physics, 16, p. 102911.

[6] Avula, D., Singh, R. K. R., Dwivedi, D. K., and Mehta, N., 2011, "Effect of friction stir welding on microstructural and mechanical properties of copper alloy," World Academy of Science, Engineering and Technology, 74, pp. 214-222.

[7] El-Danaf, E. A., and El-Rayes, M. M., 2013, "Microstructure and mechanical properties of friction stir welded 6082 AA in as welded and post weld heat treated conditions," Materials & Design (1980-2015), 46, pp. 561-572.

[8] Mishra, R. S., and Ma, Z., 2005, "Friction stir welding and processing," Materials Science and Engineering: R: Reports, 50(1-2), pp. 1-78.

[9] Silva, M., Skjødt, M., Vilaça, P., Bay, N., and Martins, P., 2009, "Single point incremental forming of tailored blanks produced by friction stir welding," Journal of Materials Processing Technology, 209(2), pp. 811-820.

[10] Kim, D., Lee, W., Kim, J., Chung, K.-H., Kim, C., Okamoto, K., Wagoner, R., and Chung, K., 2010, "Macro-performance evaluation of friction stir welded automotive tailor-welded blank sheets: Part II–Formability," International Journal of Solids and Structures, 47(7-8), pp. 1063-1081.

[11] Nguyen, N. T., Hariharan, K., Chakraborti, N., Barlat, F., & Lee, M. G., 2015, "Springback reduction in tailor welded blank with high strength differential by using multi objective evolutionary and genetic algorithms," steel research international, 86(11), 1391-1402.

[12] Hariharan, K., Nguyen, N. T., Chakraborti, N., Lee, M. G., & Barlat, F., 2014, "Multi objective genetic algorithm to optimize variable drawbead geometry for tailor welded blanks made of dissimilar steels," steel research international, 85(12), 1597-1607.

[13] Hovanski, Y., Upadhyay, P., Carsley, J., Luzanski, T., Carlson, B., Eisenmenger, M., Soulami, A., Marshall, D., Landino, B., and Hartfield-Wunsch, S., 2015, "High-speed friction-stir welding to enable aluminum tailor-welded blanks," Jom, 67, pp. 1045-1053.

[14] Parente, M., Safdarian, R., Santos, A. D., Loureiro, A., Vilaca, P., and Jorge, R. N., 2016, "A study on the formability of aluminum tailor welded blanks produced by friction stir welding," The International Journal of Advanced Manufacturing Technology, 83, pp. 2129-2141.

[15] Khan, N. Z., Siddiquee, A. N., Khan, Z. A., and Mukhopadhyay, A. K., 2017, "Mechanical and microstructural behavior of friction stir welded similar and

dissimilar sheets of AA2219 and AA7475 aluminium alloys," Journal of Alloys and Compounds, 695, pp. 2902-2908.

[16] Bhukya, S., Wu, Z., and Elmustafa, A., 2022, "Effect of post weld heat treatment on donor material assisted friction stir welding of AA6061-T6 alloy on microstructure and mechanical properties," International Conference on Flexible Automation and Intelligent Manufacturing, Springer, pp. 80-91.

[17] Feyissa, F., Ravi Kumar, D., and Rao, P. N., 2018, "Characterization of Microstructure, Mechanical Properties and Formability of Cryorolled AA5083 Alloy Sheets," Journal of Materials Engineering and Performance, 27(4), pp. 1614-1627.

[18] V. Gautam, V. M. Raut, and D. R. Kumar, “Analytical prediction of springback in bending of tailor-welded blanks incorporating effect of anisotropy and weld zone properties,” Proc. Inst. Mech. Eng. Part L J. Mater. Des. Appl., vol. 232, no. 4, pp. 294–306, 2018.

[19] H. Wallentowitz, R. Dögl, J. Leyers, and T. Parr, “and their Effects on the Automotive Industry,” vol. 105, pp. 24–25, 2003.

[20] R. S. Mishra and Z. Y. Ma, “Friction stir welding and processing,” Mater. Sci. Eng. R Reports, vol. 50, no. 1–2, pp. 1–78, 2005.

[21] N. Zaman, A. Noor, Z. A. Khan, and A. K. Mukhopadhyay, “Mechanical and microstructural behavior of friction stir welded similar and dissimilar sheets of AA2219 and AA7475 aluminium alloys,” J. Alloys Compd., vol. 695, pp. 2902–2908, 2017.

[22] E. A. El-danaf and M. M. El-rayes, “Microstructure and mechanical properties of friction stir welded 6082 AA in as welded and post weld heat treated conditions,” Mater. Des., vol. 46, pp. 561–572, 2013.

[23] D. Avula, R. Kumar, and R. Singh, “Effect of Friction Stir Welding on Microstructural and Mechanical Properties of Copper Alloy,” World Acad. Sci. Eng. Technol., vol. 74, no. February, pp. 214–223, 2011.

[24] Kleiner, M.; Geiger, M.; Klaus, A. Manufacturing of lightweight components by metal forming. CIRP Annals-Manufacturing Technology 2003, 52 (2), 521-542.

[25] Hosford, W.F.; Caddell, R.M. Metal forming: Mechanics and Metallurgy; Cambridge University Press: New York, 2011; 331 pp.

[26] GmbH, S. Metal Forming Handbook; Springer-Verlag Berlin Heidelberg: Germany, 1998; 568 pp.

[27] Kalpakjian, S.; Schmid, S. Manufacturing Processes for Engineering Materials. 4th ed; Pearson Education: New Delhi, India, 2009; 950 pp.

[28] Erichsen, A. A new test for thin sheets. Stahl and Eisen 1914, 34, 879-882.

[29] Olsen, T. Machines for ductility testing. Proc Am Soc Mater 1920, 20, 398-403.

[30] http://www.tensile.com/pages/olson-cup-test.html accessed on 12-12-2016

[31] Hecker, S.S. Cup test for assessing stretchability. Met Eng Q 1974, 14 (4), 30-36.

[32] Miles, M.P.; Siles, J.L.; Wagoner, R.H.; Narasimhan, K. A better sheet formability test. Metallurgical Transactions A 1993, 24 (5), 1143-1151.

[33] Handbook, A. Vol 14B Metalworking: Sheet Forming; ASM International: Ohio, USA, 2006; pp.

[34] Duncan, J.; Kolodziejski, J.; Glover, G. Bulge testing as an aid to formability assessment. Sheet Metal Forming and Energy Conservation 1976, 9, 131-150.

[35] Altan, T.; Tekkaya, A.E. Sheet Metal Forming: Fundamentals; ASM International: Ohio, USA, 2012; 314 pp.

[36] Swift, H. The mechanism of a simple deep-drawing operation. Sheet Met Ind 1954, 31 (330), 817-828.

[37] R. Narayanasamy, R. Ponalagusamy, and S. Raghuraman, “The effect of strain rate sensitivity on theoretical prediction of limiting draw ratio for cylindrical cup drawing process,” Mater. Des., vol. 29, no. 4, pp. 884–890, 2008.

[38] F. Stachowicz, “Formability of aluminium-alloy sheets,” J. Mech. Work. Technol., vol. 13, no. 2, pp. 229–235, 1986.

[39] P. E. Smith and D. Lee, “SAE TECHNICAL Determination of Forming Limits for Aluminum Alloys,” no. 724, 2018.

[40] Ungureanu, C.; Das, S.; Jawahir, I. Life-cycle cost analysis: aluminum versus steel in passenger cars. TMS (the minerals, metals & materials society) 2007, 11-24.

[41] Mordike, B.L.; Ebert, T. Magnesium: Properties — applications — potential. Materials Science and Engineering: A 2001, 302 (1), 37-45.

[42] Miller, W.S.; Zhuang, L.; Bottema, J.; Wittebrood, A.J.; De Smet, P.; Haszler, A.; Vieregge, A. Recent development in aluminium alloys for the automotive industry. Materials Science and Engineering: A 2000, 280 (1), 37-49.

[43] Cole, G.S.; Sherman, A.M. Light weight materials for automotive applications. Materials Characterization 1995, 35 (1), 3-9.

[44] Roth, R.; Clark, J.; Kelkar, A. Automobile bodies: Can aluminum be an economical alternative to steel? JOM. Springer-Verlag, 2001, p. 28-32.

[45] http://www.aluminumintransportation.org/research-resources/2014-duckerworldwide-survey-of-automakers accessed on 21-01-2017

[46] Hirsch, J. Recent development in aluminium for automotive applications. Transactions of Nonferrous Metals Society of China 2014, 24 (7), 1995-2002.

[47] H. Hayashi and T. Nakagawa, “Recent trends in sheet metals and their formability in manufacturing automotive panels,” vol. 46, pp. 455–487, 1994.

[48] R. W. Davies, G. J. Grant, H. E. Oliver, M. A. Khaleel, and M. T. Smith, "Forming-Limit Diagrams of Aluminum Tailor-Welded Blank Weld Material," vol. 32, no. February, 2001.

[49] M. Merklein, M. Johannes, M. Lechner, and A. Kuppert, "Journal of Materials Processing Technology A review on tailored blanks — Production , applications and evaluation," J. Mater. Process. Tech., vol. 214, no. 2, pp. 151–164, 2014.

[50] M. Paridah, A. Moradbak, A. . Mohamed, F. abdulwahab taiwo Owolabi, M. Asniza, and S. H. . Abdul Khalid, "We are IntechOpen , the world ' s leading publisher of Open Access books Built by scientists , for scientists TOP 1 %," Intech, vol. i, no. tourism, p. 13, 2016.

[51] G. Mrówka-Nowotnik and J. Sieniawski, "Influence of heat treatment on the microstructure and mechanical properties of 6005 and 6082 aluminium alloys," J. Mater. Process. Technol., vol. 162–163, no. SPEC. ISS., pp. 367–372, 2005.

[52] H. Wang, P. A. Colegrove, and J. F. Dos Santos, "Numerical investigation of the tool contact condition during friction stir welding of aerospace aluminium alloy," Comput. Mater. Sci., vol. 71, pp. 101–108, 2013.

[53] Y. J. Chao, X. Qi, and W. Tang, "Heat Transfer in Friction Stir Welding—Experimental and Numerical Studies," J. Manuf. Sci. Eng., vol. 125, no. 1, p. 138, 2003.

[54] L. Dubourg et al., "Design and properties of FSW tools : a literature review 1-Introduction 2 . Fundamental principles of Friction Stir Welding."

[55] T. Watanabe, H. Takayama, and A. Yanagisawa, "Joining of aluminum alloy to steel by friction stir welding," J. Mater. Process. Technol., vol. 178, no. 1–3, pp. 342–349, 2006.

[56] M. M. El-rayes and E. A. El-danaf, "Journal of Materials Processing Technology The influence of multi-pass friction stir processing on the microstructural and mechanical

properties of Aluminum Alloy 6082," J. Mater. Process. Tech., vol. 212, no. 5, pp. 1157–1168, 2012.

[57] M. Guerra, C. Schmidt, J. C. McClure, L. E. Murr, and A. C. Nunes, "Flow patterns during friction stir welding," Mater. Charact., vol. 49, no. 2, pp. 95–101, 2002.

[58] J. A. Schneider and A. C. Nunes, "Characterization of plastic flow and resulting microtextures in a friction stir weld," Metall. Mater. Trans. B Process Metall. Mater. Process. Sci., vol. 35, no. 4, pp. 777–783, 2004.

[59] P. Heurtier, M. J. Jones, C. Desrayaud, J. H. Driver, F. Montheillet, and D. Allehaux, "Mechanical and thermal modelling of Friction Stir Welding," J. Mater. Process. Technol., vol. 171, no. 3, pp. 348–357, 2006.

[60] A.Scialpi, L. A. C. De Filippis, and P. Cavaliere, "Materials & Design Influence of shoulder geometry on microstructure and mechanical properties of friction stir welded 6082 aluminium alloy," vol. 28, pp. 1124–1129, 2007.

[61] K. Kumar and S. V. Kailas, "The role of friction stir welding tool on material flow and weld formation," Mater. Sci. Eng. A, vol. 485, no. 1–2, pp. 367–374, 2008.

[62] L. H. Shah, S. Walbridge, and A. Gerlich, "Tool eccentricity in friction stir welding: a comprehensive review," Sci. Technol. Weld. Join., vol. 0, no. 0, pp. 1–13, 2019.

[63] Y. N. Zhang, X. Cao, S. Larose, and P. Wanjara, "Review of tools for friction stir welding and processing," Can. Metall. Q., vol. 51, no. 3, pp. 250–261, 2012.

[64] D. G. Hattingh, C. Blignault, T. I. van Niekerk, and M. N. James, "Characterization of the influences of FSW tool geometry on welding forces and weld tensile strength using an instrumented tool," J. Mater. Process. Technol., vol. 203, no. 1–3, pp. 46–57, 2008.

[65] G. M. D. Cantin, S. A. David, W. M. Thomas, E. Lara-Curzio, and S. S. Babu, "Friction Skew-stir welding of lap joints in 5083–0 aluminium," Sci. Technol. Weld. Join., vol. 10, no. 3, pp. 268–280, 2005.

[66] M. Merklein and J. Herrmann, “Effect of a local laser heat treatment on the formability of multi-layered 6000 series aluminum alloys,” Phys. Procedia, vol. 83, pp. 560–567, 2016.

[67] He, X., Gu, F., & Ball, A. (2014). A review of numerical analysis of friction stir welding. Progress in Materials Science, 65, 1-66.

[68] Maciolek, A., Jöckel, A., Völkers, S., Hatzky, M., Suckow, T., Schell, L., ... & Niendorf, T. (2024). Influence of Short-Time Post-Weld heat treatment on the performance of friction stir welded AA7075 aluminum sheets. International Journal of Fatigue, 178, 107998.

[69] Gemme, F., Verreman, Y., Dubourg, L., & Wanjara, P. (2011). Effect of welding parameters on microstructure and mechanical properties of AA7075-T6 friction stir welded joints. Fatigue & Fracture of Engineering Materials & Structures, 34(11), 877-886.

[70] Sajadifar, S. V., Moeini, G., Scharifi, E., Lauhoff, C., Böhm, S., & Niendorf, T. (2019). On the effect of quenching on postweld heat treatment of friction-stir-welded aluminum 7075 alloy. Journal of Materials Engineering and Performance, 28(8), 5255-5265.

[71] Datta, R., & Bhargava, M. (2024). Investigation of microstructure and microtexture development and its correlation with mechanical and formability behavior of dissimilar friction stir welded AA6061 and AA5754 sheets. Materials Today Communications, 41, 110556.

[72] Sen, M., & Chattopadhyaya, S. (2020). Investigations into FSW joints of dissimilar aluminum alloys. Materials Today: Proceedings, 27, 2455-2462.

[73] Schmidt, H., & Hattel, J. (2004). A local model for the thermomechanical conditions in friction stir welding. Modelling and simulation in materials science and engineering, 13(1), 77.

[74] Singh, R., Rizvi, S. A., & Tewari, S. P. (2017). Effect of friction stir welding on the tensile properties of AA6063 under different conditions. IJE Transactions A: Basics, 30(4), 597-603.

[75] Zhang, Z., Li, W., Li, J., Chao, Y. J., & Vairis, A. (2015). Microstructure and anisotropic mechanical behavior of friction stir welded AA2024 alloy sheets. Materials Characterization, 107, 112-118.

[76] Su, Y., Li, W., Shen, J., Fu, B., Dos Santos, J. F., Klusemann, B., & Vairis, A. (2021). Comparing the local-global deformation mechanism in different friction stir welding sequences of Ti-4Al-0.005 B titanium alloy T-joints. Materials Science and Engineering: A, 823, 141698.

[77] Patel, V., Li, W., Vairis, A., & Badheka, V. (2019). Recent development in friction stir processing as a solid-state grain refinement technique: microstructural evolution and property enhancement. Critical Reviews in Solid State and Materials Sciences, 44(5), 378-426.

[78] Gibson, B. T., Lammlein, D. H., Prater, T. J., Longhurst, W. R., Cox, C. D., Ballun, M. C., ... & Strauss, A. M. (2014). Friction stir welding: Process, automation, and control. Journal of manufacturing processes, 16(1), 56-73.

[79] Patsalias, G., Sofias, K., & Vairis, A. (2025). Solid-State Welding of Thin Aluminum Sheets: A Case Study of Friction Stir Welding Alloys 1050 and 5754. Metals, 15(4), 463.

[80] Li, B., He, P., Wang, J., Pan, X., Wang, Y., Wang, Z., & Baniotopoulos, C. C. (2024). Mechanical characteristic and stress-strain modelling of friction stir welded 6061-T6 aluminium alloy butt joints. Thin-Walled Structures, 198, 111645.

[81] Li, B., Li, G., Wang, J., Chen, B., Wang, Y., Dai, Y., & Dong, G. (2024). Residual stress tests and predictive model of friction stir welded normal-strength aluminium alloy H-shaped sections. Engineering Structures, 319, 118789.

[82] Salloomi, K. N., & Al-Sumaidae, S. (2021). Coupled Eulerian–Lagrangian prediction of thermal and residual stress environments in dissimilar friction stir welding of aluminum alloys. Journal of Advanced Joining Processes, 3, 100052.

[83] Guo, Y., Ma, Y. E., Zhang, X., Qian, X., & Li, J. (2020). Study on residual stress distribution of 2024-T3 and 7075-T6 aluminum dissimilar friction stir welded joints. Engineering Failure Analysis, 118, 104911.

[84] Zapata, J., Toro, M., & López, D. (2016). Residual stresses in friction stir dissimilar welding of aluminum alloys. Journal of Materials Processing Technology, 229, 121-127.

[85] Aval, H. J. (2015). Microstructure and residual stress distributions in friction stir welding of dissimilar aluminium alloys. Materials & Design, 87, 405-413.

[86] Lombard, H., Hattingh, D. G., Steuwer, A., & James, M. N. (2009). Effect of process parameters on the residual stresses in AA5083-H321 friction stir welds. Materials Science and Engineering: A, 501(1-2), 119-124.

[87] Abdulstaar, M. A., Al-Fadhalah, K. J., & Wagner, L. (2017). Microstructural variation through weld thickness and mechanical properties of peened friction stir welded 6061 aluminum alloy joints. Materials Characterization, 126, 64-73.

[88] Mishra, R. S., & Ma, D. Z. (2005). Friction stir welding and processing. Materials science and engineering: R: reports, 50(1-2), 1-78.

[89] Stewart, M. B., Adamas, G. P., Nunes Jr, A. C., & Romine, P. (1998). Developments in Theoretical and Applied Mechanics. Florida Atlantic University, USA, 472-484.

[90] Arbegast, M. W. J. (2003). Hot Deformation of Aluminum Alloys III Edited by Z. Jin, A. Beaudoin, TA Bieler and B. Radhakrishnan TMS (The Minerals, Metals & Materials Society), 2003. In Hot Deformation of Aluminum Alloys III: 2003 TMS Annual Meeting, San Diego, California, March 2-6, 2003 (p. 313). TMS Publishing Company.

[91] Sato, Y.S., Kokawa, H. Distribution of tensile property and microstructure in friction stir weld of 6063 aluminum. Metall Mater Trans A 32, 3023–3031 (2001). https://doi.org/10.1007/s11661-001-0177-8

[92] Rhodes, C. G., Mahoney, M. W., Bingel, W. H., Spurling, R. A., & Bampton, C. C. (1997). Effects of friction stir welding on microstructure of 7075 aluminum. Scripta materialia, 36(1), 69-75.

[93] Xu, S. W., Deng, X., Reynolds, A. P., & Seidel, T. U. (2001). Finite element simulation of material flow in friction stir welding. Science and Technology of Welding and Joining, 6(3), 191-193.

[94] Mishra, R. S., & Ma, D. Z. (2005). Friction stir welding and processing. Materials science and engineering: R: reports, 50(1-2), 1-78.

[95] Kumar, P., & Sharma, S. (2022). Effect of high tool rotational speed and pin diameter on mechanical properties, microstructure and formability of friction stir tailor welded blanks. Advances in Materials and Processing Technologies, 1-29.

[96] Praneetha, K., Apoorva, M., Laxmi, T. P., Sekhar, S. R., & Sashank, S. S. (2022). Experimental investigation on aluminium alloy AA6082 and AA2014 using the friction stir welding. Materials Today: Proceedings.

[97] Kamalvand, E., Jabbari, A., Sheykholeslami, M. R., Mazdak, S., Beygi, R., & Mohammadi, S. (2021). Effect of friction stir welding parameters on the deep drawing of tailor-welded blanks (TWBs). CIRP Journal of Manufacturing Science and Technology, 33, 91-99.

[98] Parente, M., Safdarian, R., Santos, A. D., Loureiro, A., Vilaca, P., & Jorge, R. M. (2016). A study on the formability of aluminum tailor welded blanks produced by friction stir welding. The International Journal of Advanced Manufacturing Technology, 83(9), 2129-2141.

[99] Steuwer, A., Peel, M. J., & Withers, P. J. (2006). Dissimilar friction stir welds in AA5083–AA6082: the effect of process parameters on residual stress. Materials Science and Engineering: A, 441(1-2), 187-196.

[100] Yoshida, T., Katayama, T., Hashimoto, K., and Kuriyama, Y. (2003). Shape control techniques for high strength steel in sheet metal forming. Shinnittetsu Giho, 25-29.

[101] Mahoney, M. W., Rhodes, C. G., Flintoff, J. G., Bingel, W. H., & Spurling, R. A. (1998). Properties of friction-stir-welded 7075 T651 aluminum. Metallurgical and materials transactions A, 29(7), 1955-1964.

[102] Vilaça, P., & Thomas, W. (2011). Friction stir welding technology. In Structural Connections for Lightweight Metallic Structures (pp. 85-124). Springer, Berlin, Heidelberg.

[103] Peel, M., Steuwer, A., Preuss, M., & Withers, P. J. (2003). Microstructure, mechanical properties and residual stresses as a function of welding speed in aluminium AA5083 friction stir welds. Acta materialia, 51(16), 4791-4801.

[104] Steuwer, A., Peel, M. J., & Withers, P. J. (2006). Dissimilar friction stir welds in AA5083–AA6082: the effect of process parameters on residual stress. Materials Science and Engineering: A, 441(1-2), 187-196.

[105] Cavaliere, P., Squillace, A., & Panella, F. (2008). Effect of welding parameters on mechanical and microstructural properties of AA6082 joints produced by friction stir welding. Journal of materials processing technology, 200(1-3), 364-372.

[106] Miles, M. P., Nelson, T. W., & Melton, D. W. (2005). Formability of friction-stir-welded dissimilar-aluminum-alloy sheets. Metallurgical and Materials Transactions A, 36(12), 3335-3342.

[107] Feng, Z., Wang, X. L., David, S. A., & Sklad, P. S. (2007). Modelling of residual stresses and property distributions in friction stir welds of aluminium alloy 6061-T6. Science and Technology of Welding and Joining, 12(4), 348-356.

[108] Min-Su, H. A. N., Seung-Jun, L. E. E., Jae-Cheul, P. A. R. K., Seok-Cheol, K. O., Yong-Bin, W. O. O., & Seong-Jong, K. I. M. (2009). Optimum condition by mechanical characteristic evaluation in friction stir welding for 5083-O Al alloy. Transactions of Nonferrous Metals Society of China, 19, s17-s22.

[109] Simoncini, M., Cabibbo, M., & Forcellese, A. (2016). Development of double-side friction stir welding to improve post-welding formability of joints in AA6082 aluminium alloy. Proceedings of the Institution of Mechanical Engineers, Part B: Journal of Engineering Manufacture, 230(5), 807-817.

[110] Kumar, K. S. S., & Reddy, A. C. (2016). Die Less Single Point Incremental Forming Process of Aa6082 Sheet Metal to Draw Parabolic Cups Using ABAQUS. International Journal of Advanced Technology in Engineering and Science, 4(11), 127-134.

[111] Liu, J., Gao, H., El Fakir, O., Wang, L., & Lin, J. (2015). HFQ forming of AA6082 tailor welded blanks. In MATEC Web of Conferences (Vol. 21, p. 05006). EDP Sciences.

[112] Dwivedi, S. P. (2014). Effect of process parameters on tensile strength of friction stir welding A356/C355 aluminium alloys joint. Journal of mechanical science and technology, 28(1), 285-291.

[113] Shaikh, A., Bhatt, K. D., & Chaudhary, A. B. (2014). Effect of friction stir welding process parameters on polymer weld. International Journal for Technological Research in Engineering, 9, 741-743.

[114] Raju, L. S., Kumar, A., & Indreswaraiah, P. (2014). Effect of Welding Speed on Mechanical Properties of Friction Stir Welded Copper. Bonfring International Journal of Industrial Engineering and Management Science, 4(2), 68-71.

[115] Prasad, P. J. C., Hema, P., & Ravindranath, K. (2014). Optimization of Process Parameters for Friction Stir Welding of Aluminum Alloy Aa6061 Using Square Pin

Profile. International Journal of Mechanical Engineering and Robotics Research, 3(2), 455.

[116] Meshram, M. P., Kodli, B. K., & Dey, S. R. (2014). Friction stir welding of austenitic stainless steel by PCBN tool and its joint analyses. Procedia materials science, 6, 135-139.

[117] Ahmadi, H., Mostafa Arab, N. B., & Ghasemi, F. A. (2014). Optimization of process parameters for friction stir lap welding of carbon fibre reinforced thermoplastic composites by Taguchi method. Journal of Mechanical Science and Technology, 28(1), 279-284.

[118] Elatharasan, G., & Kumar, V. S. (2012). Modelling and optimization of friction stir welding parameters for dissimilar aluminium alloys using RSM. Procedia engineering, 38, 3477-3481.

[119] Ko, D. H., Kim, J. H., Ko, D. C., & Kim, B. M. (2014). Improvement of Weldment Properties by Hot Forming Quenching of Friction Stir Welded TWB Sheet. Advances in Mechanical Engineering, 6, 257510.

[120] Hui, W. A. N. G., Luo, Y. B., Friedman, P., Chen, M. H., & Lin, G. A. O. (2012). Warm forming behavior of high strength aluminum alloy AA7075. Transactions of Nonferrous Metals Society of China, 22(1), 1-7.

[121] A. Steuwer, M. J. Peel, and P. J. Withers, “Dissimilar friction stir welds in AA5083 – AA6082 : The effect of process parameters on residual stress,” vol. 441, pp. 187–196, 2006.

[122] T. Yoshida, K. Hashimoto, T. Katayama, and Y. Kuriyama, “Shape control techniques for high strength steel in sheet metal forming,” Nippon Steel Tech. Rep., no. 88, pp. 27–32, 2003.

[123] “Submitted for publication in ICRS-6 Proceedings,” no. 1, 2000.

[124] H. Strength, “Stir of High Strength Alloys by Friction Aluminum Welding,” vol. 40, 2000.

[125] L. Svensson, L. Karlsson, H. Larsson, B. Karlsson, M. Fazzini, and J. Karlsson, “Microstructure and mechanical properties of friction stir welded aluminium alloys with special reference to AA 5083 and AA 6082,” vol. 5, no. 5, pp. 285–296, 2000.

[126] T. Publications and F. U. Berlin, “No Title,” vol. 402, pp. 1671–1676, 2002.

[127] J. K. Paik and A. Duran, “Ultimate Strength of Aluminum Plates and Stiffened Panels for Marine Applications,” vol. 41, no. 3, pp. 108–121, 2004.

[128] M. W. Mahoney, C. G. Rhodes, J. G. Flintoff, R. A. Spurling, and W. H. Bingel, “Properties of Friction-Stir-Welded 7075 T651 Aluminum,” vol. 29, no. July, 1998.

[129] M. Peel, A. Steuwer, M. Preuss, and P. J. Withers, “Microstructure , mechanical properties and residual stresses as a function of welding speed in aluminium AA5083 friction stir welds,” vol. 51, pp. 4791–4801, 2003.

[130] P. Cavaliere, A. Squillace, and F. Panella, “Effect of welding parameters on mechanical and microstructural properties of AA6082 joints,” vol. 0, pp. 364–372, 2007.

[131] M. P. Miles, D. W. Melton, and T. W. Nelson, “Formability of Friction-Stir-Welded Dissimilar-Aluminum- Alloy Sheets,” vol. 36, no. December, 2005.

[132] Z. Feng, X.-L. Wang, S. A. David, and P. S. Sklad, “Modelling of residual stresses and property distributions in friction stir welds of aluminium alloy 6061-T6,” Sci. Technol. Weld. Join., vol. 12, no. 4, pp. 348–356, 2007.

[133] M. Han, S. Lee, J. Park, S. Ko, Y. Woo, and S. Kim, “Optimum condition by mechanical characteristic evaluation in friction stir welding for 5083-O Al alloy,” Trans. Nonferrous Met. Soc. China, vol. 19, pp. s17–s22, 2009.

[134] J. Liu, M. Tan, A. Jarfors, Y. Aue-u-lan, and S. Castagne, “Formability in AA5083 and AA6061 alloys for light weight applications,” Mater. Des., vol. 31, pp. S66–S70, 2010.

[135] P. F. Bariani, S. Bruschi, A. Ghiotti, and F. Michieletto, “CIRP Annals - Manufacturing Technology Hot stamping of AA5083 aluminium alloy sheets,” CIRP Ann. - Manuf. Technol., vol. 62, no. 1, pp. 251–254, 2013.

[136] J. Liu, M. Tan, and Y. Aue-u-lan, “Superplastic-like forming of non-superplastic AA5083 combined with mechanical pre-forming,” pp. 123–129, 2011.

[137] D. E. Cipoletti, A. F. Bower, Y. Qi, and P. E. Krajewski, “The influence of heterogeneity in grain boundary sliding resistance on the constitutive behavior of AA5083 during high-temperature deformation,” vol. 504, pp. 175–182, 2009.

[138] C. Zhang, L. Leotoing, D. Guines, and E. Ragneau, “Theoretical and numerical study of strain rate influence on AA5083 formability,” vol. 9, pp. 3849–3858, 2008.

[139] M. Simoncini, M. Cabibbo, and A. Forcellese, “Development of double-side friction stir welding to improve post-welding formability of joints in AA6082 aluminium alloy,” vol. 230, no. 5, pp. 807–817, 2016.

[140] K. S. S. Kumar and A. C. Reddy, “DIE LESS SINGLE POINT INCREMENTAL FORMING PROCESS OF AA6082 SHEET METAL TO DRAW PARABOLIC CUPS USING ABAQUS,” pp. 127–134.

[141] N. Li, M. S. Mohamed, J. Cai, J. Lin, D. Balint, and T. A. Dean, “Experimental and Numerical Studies on the Formability of Materials in Hot Stamping and Cold Die Quenching Processes,” vol. 1561, pp. 1555–1561, 2011.

[142] X. Luan, O. El, H. Gao, J. Liu, and L. Wang, “Formability of AA6082-T6 at Warm and Hot Stamping Conditions,” vol. 716, pp. 107–113, 2016.

[143] J. Liu, H. Gao, O. El Fakir, L. Wang, and J. Lin, “HFQ forming of AA6082 tailor welded blanks,” vol. 05006, 2015.

[144] M. S. Mohamed, A. D. Foster, J. Lin, D. S. Balint, and T. A. Dean, "International Journal of Machine Tools & Manufacture Investigation of deformation and failure features in hot stamping of AA6082 : Experimentation and modelling," Int. J. Mach. Tools Manuf., vol. 53, no. 1, pp. 27–38, 2012

[145] Choi, S.-H., Kim, K.-H., Oh, K. H., and Lee, D. N., 1997, "Tensile Deformation Behavior of Stainless Steel Clad Aluminum Bilayer Sheet," Materials Science and Engineering: A, 222(2), pp. 158–165. https://doi.org/10.1016/S0921- 5093(96)10514-1.

[146] Nyung Lee, D., and Keun Kim, Y., 1988, "Tensile Properties of Stainless SteelClad Aluminium Sandwich Sheet Metals," J Mater Sci, 23(4), pp. 1436–1442. https://doi.org/10.1007/BF01154614.

[147] Masoumi, M., and Emadoddin, E., 2013, "Interface Characterization and 143 Formability of Two and Three-Layer Composite Sheets Manufactured by Roll Bonding," Materials & Design (1980-2015), 44, pp. 392–396. https://doi.org/10.1016/j.matdes.2012.08.030.

[148] Yoshida, F., and Hino, R., 1997, "Forming Limit of Stainless Steel-Clad Aluminium Sheets under Plane Stress Condition," J Mater Process Technol, 63(1–3), pp. 66–71. https://doi.org/10.1016/S0924-0136(96)02601-5.

[149] Basril, M. A. M., Teng, H. M., Azuddin, M., and Choudhury, I. A., 2017, "The Effect of Heating Temperature and Methods towards the Formability of Deep Drawn Square Metal Cup," IOP Conf Ser Mater Sci Eng, 210, p. 012067. https://doi.org/10.1088/1757-899X/210/1/012067.

[150] Jayahari, L., Naik, B. B., and Singh, S. K., 2014, "Effect of Process Parameters and Metallographic Studies of ASS-304 Stainless Steel at Various 144 Temperatures under Warm Deep Drawing," Procedia Materials Science, 6, pp. 115–122. https://doi.org/10.1016/j.mspro.2014.07.013.

[151] Ghosh, M., Miroux, A., Werkhoven, R. J., Bolt, P. J., and Kestens, L. A. I., 2014, "Warm Deep-Drawing and Post Drawing Analysis of Two Al–Mg–Si Alloys," J Mater Process Technol, 214(4), pp. 756–766. https://doi.org/10.1016/j.jmatprotec.2013.10.020.

[152] Alinia, S., Khamedi, R., and Ahmadi, I., 2018, "The Investigation and Optimization of Process Parameters in Warm Deep Drawing of ASS304 Steel Using Box Behnken Design and Applying Temperature Gradient," Exp Tech, 42(6), pp. 645–657. https://doi.org/10.1007/s40799-018-0285-7.

[153] Goud, R. R., Prasad, K. E., and Singh, S. K., 2014, "Formability Limit Diagrams of Extra-Deep-Drawing Steel at Elevated Temperatures," Procedia Materials Science, 6, pp. 123–128. https://doi.org/10.1016/j.mspro.2014.07.014.

[154] Basak, S., Panda, S. K., and Lee, M.-G., 2020, "Formability and Fracture in Deep Drawing Sheet Metals: Extended Studies for Pre-Strained Anisotropic Thin Sheets," Int J Mech Sci, 170, p. 105346. https://doi.org/10.1016/j.ijmecsci.2019.105346.

[155] Singh, A., Basak, S., P.S., L. P., Roy, G. G., Jha, M. N., Mascarenhas, M., and Panda, S. K., 2018, "Prediction of Earing Defect and Deep Drawing Behavior of Commercially Pure Titanium Sheets Using CPB06 Anisotropy Yield Theory," J Manuf Process, 33, pp. 256–267. https://doi.org/10.1016/j.jmapro.2018.05.003.

[156] Lin, P., Sun, Y., Chi, C., and Wang, W., 2017, "Effect of Plastic Anisotropy of ZK60 Magnesium Alloy Sheet on Its Forming Characteristics during Deep 145 Drawing Process," The International Journal of Advanced Manufacturing Technology, 88(5–8), pp. 1629–1637. https://doi.org/10.1007/s00170-016- 8816-9.

[157] Atrian, A., and Fereshteh-Saniee, F., 2013, "Deep Drawing Process of Steel/Brass Laminated Sheets," Compos B Eng, 47, pp. 75–81. https://doi.org/10.1016/j.compositesb.2012.10.023.

[158] Atrian, A., and Panahi, H., 2018, “Experimental and Finite Element Investigation on Wrinkling Behaviour in Deep Drawing Process of Al3105/Polypropylene/Steel304 Sandwich Sheets,” Procedia Manuf, 15, pp. 984–991. https://doi.org/10.1016/j.promfg.2018.07.396.

[159] Pazand, K., Moarrefzadeh, A., and Morovvati, M. R., 2022, “Experimental and Numerical Evaluation of Formability in Three-Layer Metallic Sheets with Various Layer Arrangements,” Engineering Research Express, 4(3), p. 035034. https://doi.org/10.1088/2631-8695/ac89ce.

[160] Karajibani, E., Fazli, A., and Hashemi, R., 2015, “Numerical and Experimental Study of Formability in Deep Drawing of Two-Layer Metallic Sheets,” The International Journal of Advanced Manufacturing Technology, 80(1–4), pp. 113–121. https://doi.org/10.1007/s00170-015-6978-5.

[161] Afshin, E., and Kadkhodayan, M., 2015, “An Experimental Investigation into the Warm Deep-Drawing Process on Laminated Sheets under Various Grain Sizes,” Mater Des, 87, pp. 25–35. https://doi.org/10.1016/j.matdes.2015.07.061.

[162] Liu, J., Tan, M.-J., and Castagne, S., 2010, "Formability in AA5083 and AA6061 alloys for light weight applications," Materials & Design, 31, pp. S66-S70.

[163] Priyadarshini, A., Sancheti, C. I., and Dwarka, S. S., 2015, "Comparative study of forgeability of as extrude AA6082 and as cast AA6082 alloy," no. October, pp. 1-6.

[164] Lee, Y. B., Shin, D. H., Park, K. T., & Nam, W. J., 2004, "Effect of annealing temperature on microstructures and mechanical properties of a 5083 Al alloy deformed at cryogenic temperature," Scripta materialia, 51(4), 355-359.

[165] Changela, K., Krishnaswamy, H., & Digavalli, R. K., 2020, "Mechanical behavior and deformation kinetics of aluminum alloys processed through cryorolling and subsequent annealing," Metallurgical and Materials Transactions A, 51, 648-666.

[166] Kumar, S., Kumar, S., and Kumar, A., 2013, "Optimization of process parameters for friction stir welding of joining A6061 and A6082 alloys by Taguchi method," Proceedings of the Institution of Mechanical Engineers, Part C: Journal of Mechanical Engineering Science, 227(6), pp. 1150-1163.

[167] Singh, N., Belokar, R. M., & Walia, R. S., 2022, "Fabrication and mechanical characterization of Al7075-T6/SiC/Gr/S-glass fiber particulate reinforced hybrid metal matrix composite using vacuum sealed stir casting technique," Transactions of the Indian Institute of Metals, 75(7), 1741-1750.

[168] Kumar, A., Kumar, D. R., and Gautam, V., 2019, "Prediction of residual stresses in biaxial stretching of tailor welded blanks by finite element analysis," IOP Conference Series: Materials Science and Engineering, IOP Publishing, pp. 012039.

[169] Ling, J., and Lee, S., 2015, "Characterization of a portable x-ray device for residual stress measurements," Adv X-ray Anal., 59, pp. 153-161.

[170] Hibbit, Karlsson, and Sorensen, 2007, ABAQUS/Standard Analysis User's Manual, Hibbit, Karlsson, Sorensen Inc.

PLAGIARISM REPORT

DELHI TECHNOLOGICAL UNIVERSITY

(Formerly Delhi College of Engineering)
Shahbad Daulatpur, Main Bawana Road, Delhi-42

PLAGIARISM VERIFICATION

Title of the Thesis "**Experimental and Numerical Investigations on Formability of Tailor Welded Blanks Prepared by Friction Stir Welding Process**"

Total Pages: **152**

Name of the Scholar: **Mr. SUBHAJIT KONAR**

Supervisor: **Prof. VIJAY GAUTAM**

Department of Mechanical Engineering

This is to report that the above thesis was scanned for similarity detection. Process and outcome is given below:

Software used: **Turnitin**

Similarity Index: **10%**

Total Word Count: **33,449.**

Date: _____

Candidate's signature **Signature of Supervisor**

PUBLICATIONS BASED ON THE RESEARCH WORK

The followings are the publications in journals and conferences based on the present work.

International Journals: -

1. **Konar, S.,** & Gautam, V. (2025). Investigations on Formability Enhancement of Friction Stir Tailor-Welded Blanks. *Journal of Engineering Materials and Technology*, *147*(3), 031004. https://doi.org/10.1115/1.4067785 [**ASME: IF1.9, SCIE**]
2. **Konar, S.,** Gautam, V. (2025). Deformation Behaviour of a High Manganese and Measurements of Microstructural Features Using Orientation Imaging Microscopy. *Journal of Metrology Society of India*. https://doi.org/10.1007/s12647-025-00859-1. [**Springer: IF 1.3, SCIE**]
3. Sharma, P. K., Gautam, V., **Konar, S.** (2025). Experimental and Numerical Analysis of Springback of AA1050-Fly Ash Green Composite Produced by Stir Casting Technique. *Journal of Materials Engineering and Performance*, 1-8. [**Springer: IF2.0, SCIE**]

International Book Chapters: -

4. Gautam, V., Kumar, D. R., & **Konar, S.** (2020). Experimental and Numerical Characterization of Residual Stresses in Tailor Welded Blanks After Springback. In Advances in Simulation, Product Design and Development (pp. 79-92). Springer, Singapore.
5. **Konar, S.**, & Gautam, V. (2020, July). Numerical Investigations on Steady-State Dynamic and Transient Rolling of Automobile Tire. In *International*

Conference on Recent Advancements in Mechanical Engineering (pp. 785-795). Singapore: Springer Nature Singapore.

International Conferences: -

6. **Subhajit Konar** and Vijay Gautam "Studies on Anisotropic Behaviour of Aluminium Alloy Sheets." International conference on Recent Advances in Mechanical Engineering for Sustainable Development (ISME-2024) held at Delhi Technological University during July 11-13, 2024.
7. **Subhajit Konar** and Vijay Gautam "Experimental Studies on the Formability of Different Steel Sheets." International conference on Recent Advances in Mechanical Engineering for Sustainable Development (ISME-2024) held at Delhi Technological University during July 11-13, 2024.

PROOF OF PUBLICATIONS

ASME Journal of Engineering Materials and Technology
Online journal at:
https://asmedigitalcollection.asme.org/materialstechnology

Investigations on Formability Enhancement of Friction Stir Tailor-Welded Blanks

Subhajit Konar
Department of Mechanical Engineering,
Delhi Technological University,
Shahbad Daulatpur, Main Bawana Road,
Delhi 110042, India
e-mails: subhokonar94@gmail.com;
subhajitkonar_2k20phdme508@dtu.ac.in

Vijay Gautam[1]
Department of Mechanical Engineering,
Delhi Technological University,
Shahbad Daulatpur, Main Bawana Road,
Delhi 110042, India
e-mail: vijaygautam@dce.ac.in

Experimental and numerical investigations on the formability of longitudinally butt-welded tailor-welded blank of the same thickness prepared by friction stir welding are presented in this article. The friction stir-welding technique involves a solid-state stirring mechanism to butt weld the two blanks of aluminum alloy AA5083 and AA6082 both in the annealed state. To study the effect of welded region on formability, experiments are performed on tailor-welded blanks with and without the annealing operation. The tensile properties of the parent sheets, welded blanks, and welded region are determined by performing standard uniaxial tension tests. The elastic properties, true stress–true strain, and anisotropic data sets are used in the material model for the prediction of failure strains to develop forming limit plots. The predicted results from finite element analysis are validated with the experimental results obtained from the limiting dome height test. The annealing is observed to enhance the formability of the friction stir tailor-welded blank (FSTWB) by almost 13% in plane strain and equibiaxial stretch conditions.
[DOI: 10.1115/1.4067785]

Keywords: formability, friction stir tailor-welded blanks, annealed and nonannealed sheets, aluminum alloys, limiting dome height, forming limit diagram, mechanical behavior, microstructure property relationships, plastic behavior

1 Introduction

The weld region in a friction stir tailor-welded blank (FSTWB) prepared by joining two or more sheets with the same or different thicknesses of the same or different materials in a single plane prior to forming is the main reason for the reduction in its formability. However, due to numerous benefits, it is important to enhance the formability of tailor-welded blanks (TWBs) used in sheet metal components for automotive and aerospace industries. Also, it has become an essential mass production technology that reduces the weight of the finished products by eliminating a number of reinforcements and stiffeners [1]. Mass optimization for lighter components is achieved by the use of a low-density ultra-high strength aluminum alloy, which offers good formability and crashworthiness [2]. Based on the classification, fusion welding and solid-state welding are the two techniques commonly employed to prepare a TWB. Although the fusion welding technique is a high-speed process providing good joint strength and efficiency in the steel components, it is not preferred in welding aluminum alloys due to the formation of an oxide layer and other solidification defects [3]. The friction stir-welding (FSW) technique is a solid-state welding process that is a good alternative to the fusion welding in addressing the problems encountered in welding aluminum alloys. It incorporates the use of friction heat caused due to severe plastic deformation using a nonconsumable rotating tool moving along the weld line during the joining of the two different sheets by a mechanical interlocking mechanism [4]. Apart from low power consumption, FSW technique offers good weld strength and integrity with negligible distortion [5].

In the last decades, owing to academic and industrial applications, many researchers have studied the deformation behavior and formability of TWBs prepared by FSW technique [6–8]. Silva et al. [9] carried out experimental studies on the forming behavior of a TWB of aluminum alloy using a single-point incremental forming technique and confirmed that FSW-produced TWB can be successfully used in the manufacturing of components requiring deep depths. Experimental and numerical methods were used by Kim et al. [10] to study the formability of FSTWBs made of four different sheets with varying thicknesses, such as 6111-T4, 5083-H18, 5083-O, and DP590. Yld2000-2d, a nonquadratic orthogonal anisotropic yield function, was used without considering anisotropy. It was concluded that accurate numerical prediction of the forming limit is dependent on the properties of the welded region. Nguyen et al. [11] studied the springback behavior of TWBs made from twinning-induced plasticity (TWIP) and mild steels, noting significant differences on either side due to the large disparity in material strength. To mitigate springback defects during the U-draw bending process of such TWBs, the researchers applied varying blank holding force (BHF) profiles on both sides of the blank. They proposed a systematic method to determine optimal BHF-stroke profiles that reduced the springback. Hariharan et al. [12] studied the formability of tailor-welded blanks with a very high strength ratio, created by

[1]Corresponding author.

Contributed by the Materials Division of ASME for publication in the Journal of Engineering Materials and Technology. Manuscript received June 4, 2024; final manuscript received January 24, 2025; published online February 14, 2025. Assoc. Editor: Abigail Hunter.

Copyright © 2025 by ASME

MAPAN-Journal of Metrology Society of India (December 2025) 40(4):991–1005
https://doi.org/10.1007/s12647-025-00859-1

ORIGINAL PAPER

Deformation Behaviour of a High Manganese Austenitic Steel and Measurements of Microstructural Features Using Orientation Imaging Microscopy

S. Konar[1] and V. Gautam[2]*

[1]Department of Mechanical Engineering, Research Scholar, Delhi Technological University, ShahbadDaulatpur, Main Bawana Road, Delhi 110042, India

[2]Department of Mechanical Engineering, Delhi Technological University, Shahbad Daulatpur, Main Bawana Road, Delhi 110042, India

Received: 28 May 2025 / Accepted: 17 September 2025 / Published online: 30 September 2025

© Metrology Society of India 2025

Abstract: In order to explore the deformation behaviour, tensile specimens of a cast Hadfield steel were prepared and elongated to a strain of 10%, 15% and 20%. Assuming that the materials obeys power law of strain hardening, the strain hardening exponent and strength coefficients were evaluated from log true stress vs. log true strain data. The samples were also prepared for electron backscattered diffraction to study the evolution of microstructure and texture and compared with the microstructural characteristics of undeformed samples. It was observed that the dislocation density increased with the plastic deformation from 10 to 15% strain due to increased twinning density but it decreased in the specimens tested to 20% of plastic strain due to dislocation annihilations and grain refinement by mechanical twinning. The nature of residual stress measured by using a XRD-$\sin^2\psi$ method in the as-cast samples was observed to be tensile whereas, in the deformed specimens it was compressive and correlated with the microstructural characteristics of the samples. The measurement results of microhardness of the tested samples showed an increased hardness with higher strains due to formation of α-martensite phase within the matrix. It was observed that the results obtained for residual stress and microhardness are in sync with the microstructural findings.

Keywords: Hadfield steel; Tensile deformation; Dislocation density; Microstructure; XRD-$\sin^2\psi$ method

1. Introduction

Since its creation in the 1880s, Hadfield steel which is an austenitic steel high in carbon and manganese is the primary steel used to make railway turnouts by casting technique, but some substitutes over the past 40 years, steels with improved wear resistance have also been introduced [1, 2]. Hadfield steel contains carbon in the range of 1.0–1.4% and manganese in the range of 10–14% so that a ratio of ~ 1:10 is maintained. It has great toughness, ductility, work hardening ability, and excellent wear resistance [3]. Hadfield steels are still often utilized to make wear-resistant components for a variety of components, including hammers for impact, variety of jaws and cones for crushers, grinding mill liners, excavator bucket teeth, tractor crawler treads, continuous tracks for battle tanks, and railroad turnouts [4, 5]. These uses are ascribed to Hadfield steel's superior toughness and strain hardening properties, as well as its capacity to manufacture castings in a range of sizes at a comparatively low cost. In its as-cast state, Hadfield steel includes $(Fe, Mn)_3C$ carbides. Before usage, it is normal industrial practice to solution heat treat the material, allowing carbides to dissolve and form a fully austenitic structure. The cast sample is typically solution-annealed at approximately 1050 °C for a few hours before being quenched with water. Due to the absence of an inert environment, high solutionizing temperature produce considerable surface decarburization and manganese loss, culminating in the formation of α-martensite on the surface layer following quenching. It quickly hardens after plastic deformation [3, 6].

Hadfield steel's strain hardening mechanism has been investigated by several researchers since its introduction.

*Corresponding author, E-mail: vijaygautam@dce.ac.in

DELHI TECHNOLOGICAL UNIVERSITY
(Formerly Delhi College of Engineering)
Bawana Road, Delhi-110042

CERTIFICATE

OF PRESENTATION

Sl. No. ISME-2024/ Pre/163

Paper ID - ISME-2024_248

This is to certify that

Subhajit Konar, Delhi Technological University, Delhi

has participated in the 22ND ISME - International Conference on "Recent Advances in Mechanical Engineering for Sustainable Development (ISME-2024) " organized by the Department of Mechanical Engineering, Delhi Technological University, Delhi held on July 11-13, 2024. He/She has also presented the paper titled, ***Experimental Studies on the Formability of Different Steel Sheets****. We wish him/her a bright success in all his/her future endeavors.*

Prof. Amit Pal Chair | **Prof. Vijay Gautam** Chair | **Prof. Qasim Murtaza** Secretary | **Dr. Pravin Kumar** Convener

DELHI TECHNOLOGICAL UNIVERSITY
(Formerly Delhi College of Engineering)
Bawana Road, Delhi-110042

CERTIFICATE

OF PRESENTATION

Sl. No. ISME-2024/ Pre/164

Paper ID - ISME-2024_318

This is to certify that

Subhajit Konar, Delhi Technological University, Delhi

has participated in the 22ND ISME - International Conference on "Recent Advances in Mechanical Engineering for Sustainable Development (ISME-2024) " organized by the Department of Mechanical Engineering, Delhi Technological University, Delhi held on July 11-13, 2024. He/She has also presented the paper titled, ***Studies on Anisotropic Behaviour of Aluminium Alloy Sheets****. We wish him/her a bright success in all his/her future endeavors.*

Prof. Amit Pal Chair | **Prof. Vijay Gautam** Chair | **Prof. Qasim Murtaza** Secretary | **Dr. Pravin Kumar** Convener

BIO DATA

Mr. Subhajit Konar is currently working as Chief of Staff at Thinkmetal Private limited, Chennai. He has 6.5 years of experience in the field of Intellectual Property Rights. He has worked for iRunway and Elevate for projects like Prior art search, infringement analysis, Freedom to operate search, Landscape analysis and invalidity analysis. His area of research has been in sheet metal forming of Tailor Welded Blanks, Friction Stir Welding. He has authored two SCIE indexed and two Scopus indexed journals. He has presented four papers at national and international conferences. Currently, he is involved in development of 3D printer manufacturing and filament fabrication.